Optimization of Furnace Residence Time and Ingots Positioning during the Heat Treatment Process of Large Size Forged Ingots

by

Nima BOHLOOLI ARKHAZLOO

MANUSCRIPT-BASED THESIS PRESENTED TO ÉCOLE DE TECHNOLOGIE SUPÉRIEURE IN PARTIAL FULFILLMENT FOR THE DEGREE OF DOCTOR OF PHILOSOPHY
Ph.D.

MONTREAL, JANUARY 28TH 2020

ÉCOLE DE TECHNOLOGIE SUPÉRIEURE
UNIVERSITÉ DU QUÉBEC

BOARD OF EXAMINERS

THIS THESIS HAS BEEN EVALUATED

BY THE FOLLOWING BOARD OF EXAMINERS

Prof. Mohammad Jahazi, Thesis Supervisor
Department of Mechanical Engineering at École de technologie supérieure

Prof. Farzad Bazdidi-Tehrani, Thesis Co-supervisor
School of Mechanical Engineering at Iran university of science and technology

Prof. Vahé Nerguizian, President of the Board of Examiners
Department of Electrical engineering at École de technologie supérieure

Prof. Henri Champliaud, Member of the jury
Department of Mechanical Engineering at École de technologie supérieure

Prof. Louis Gosselin, External Evaluator
Department of Mechanical Engineering at Université Laval

THIS THESIS WAS PRENSENTED AND DEFENDED

IN THE PRESENCE OF A BOARD OF EXAMINERS AND PUBLIC

JANUARY 22 ND 2020

AT ÉCOLE DE TECHNOLOGIE SUPÉRIEUR

ACKNOWLEDGEMENT

I would like to convey my earnest gratitude to my supervisor, Prof. Mohammad Jahazi, whose support, guidance, expertise and patience added considerably to my research experience and without him none of this would have been possible to achieve. I am thankful to him for believing in my accomplishments and providing me with every opportunity to assimilate. I would also wish to thank Prof. Farzad Bazdidi-Tehrani (my co-supervisor) for his kind support, guidance and conveying numerical simulation expertise during my Ph.D. program. He has helped me at all times during my presence in Iran University of Science and Technology (IUST) and after that. I also extend my earnest gratitude to Dr. Mohammad Jadidi, a post-doctoral researcher at IUST, for the fruitful discussions I held with him. He enthusiastically helped me throughout my term with respect to CFD simulation and numerical approaches.

Particular thanks are given to our Industrial partner, Finkl Steel, especially the R & D, Metallurgy and Engineering Departments, for providing real-scale instrumentation and measurements and their collaboration in this project.

Gratitude is also expressed for all CM2P members for their cooperation during the entire journey of my Ph.D.

My utmost gratitude is given to my parents for their outstanding support, kindness, love and constant motivation throughout this journey.

Optimisation du temps de résidence dans le four ainsi que le positionnement de lingots forgés de grande taille lors du processus de traitement thermique

Nima BOHLOOLI ARKHAZLOO

RÉSUMÉ

Les pièces forgées de grande taille sont communément utilisées dans les industries de l'énergie et du transport (arbres de turbines, trains d'atterrissage, etc.). Ces pièces acquièrent leurs propriétés mécaniques supérieures (par exemple, la dureté) grâce à un processus de traitement thermique appelé trempe et revenu. Le processus de revenu (incluant le chauffage et le maintien en chauffe) a lieu dans des fours à gaz et a un impact direct sur les propriétés finales du produit en raison des modifications microstructurales majeures induites par l'effet de la température. Une fois que les paramètres de revenu sont contrôlés (temps et température) les propriétés des matériaux peuvent être généralement optimisées. Distribution non uniforme de la température autour des pièces qui résulte des interactions thermiques à l'intérieur du four ou du positionnement des brames, peut causer une variation dans les propriétés mécaniques d'une extrémité à l'autre de la pièce, une modification de la microstructure ou même initier des fissurations. Par contre, une optimisation du temps de séjour dans le four de traitement thermique peut réduire la consommation d'énergie et éviter les changements microstructuraux indésirables. Cependant, la production industrielle repose principalement sur des corrélations empiriques qui ne sont pas toujours fiables. La prédiction précise de la température en fonction du temps des pièces forgées de grande taille dans les fours de traitement thermique à gaz nécessite un examen quantitatif exhaustif de l'échauffement par la compréhension des interactions thermiques conjuguées complexes à l'intérieur du four. Les limites des études analytiques et la complexité et le coût des expérimentations ont rendu les simulations numériques une solution efficace pour analyser les problèmes de la dynamique des fluides (CFD) dans ce domaine d'étude. Cependant, parmi les études publiées sur les fours à gaz, les fours à petite échelle ou ceux avec un temps de fonctionnement plus court ont été principalement considérés (en utilisant différentes simplifications comme les calculs à l'état stationnaire) et ce principalement en raison de la complexité des phénomènes et des temps de calcul élevés. Par la suite, très peu d'études ont été consacrées à l'amélioration des modèles de chargement des pièces de grande taille dans les fours à gaz et à l'optimisation de leur temps de résidence. De plus, peu d'information est disponible dans la littérature sur les limites et particularités des différentes approches numériques permettant de calculer les interactions thermiques dans le flux réactif turbulent des fours de grande taille chauffés au gaz. À cet égard, l'objectif principal de ce projet est de fournir une analyse quantitative complète de la période transitoire du chauffage et une compréhension des interactions thermiques à l'intérieur du four afin d'optimiser, le temps de

séjour et l'uniformité de la température pendant le traitement thermique. Pour atteindre cet objectif, les étapes ci-après ont été suivies:

La première partie de cette étude, fournit une analyse transitoire complète des caractéristiques de chauffage des pièces forgées de grande taille dans un four à gaz, en utilisant des températures mesurées expérimentalement et des simulations CFD. Un modèle CFD 3D du four à gaz a été généré, incluant, la chambre de traitement thermique, et les brûleurs à gaz. Les interactions entre la chaleur et l'écoulement du fluide, incluant la turbulence, la radiation et la combustion, ont été simultanément considérées dans le modèle en utilisant respectivement les modèles DO et EDM. En outre, l'applicabilité du modèle de radiation S2S a été évaluée pour quantifier l'effet du produit de combustion dans le four et le facteur de forme dû à la radiation durant le transfert de chaleur. Des mesures de températures ont été réalisées à plusieurs endroits grâce à l'instrumentation d'un bloc forgé de grande taille et l'intérieur du four, pour l'analyse expérimentale du processus de chauffage et aussi pour la validation du modèle CFD. Un bon accord a été obtenu avec une erreur maximale d'environ 7% entre les prédictions numériques et les mesures expérimentales. Les résultats ont montré qu'en dépit de l'uniformité de la température du four sans chargement, chaque surface du bloc présentait des vitesses de chauffage différentes après le chargement (chargement simple) ; des différences de température allant jusqu'à 200 k. L'analyse des résultats a également révélée la fiabilité du modèle S2S et a mis en évidence l'importance du facteur de forme du rayonnement pour des besoins d'optimisation pour cette application. Les résultats ont été corrélés avec la géométrie du four, la formation de structures tourbillonnaires et les circulations du fluide autour de la pièce. Les données expérimentales et les prévisions du modèle CFD pourraient être directement utilisées pour l'optimisation du processus de traitement thermique forgées de grande taille.

La deuxième partie de cette étude vise à déterminer l'effet de la configuration du chargement (configuration des chargements multiples) sur la distribution de la température des pièces forgées lors du traitement thermique, afin d'obtenir une meilleure uniformité de température; qui par la suite favorise l'obtention de propriétés mécaniques homogènes. Cette partie vise également l'optimisation du temps de séjour des lingots forgés de grande taille dans un four de revenu, proposant une nouvelle méthodologie hybride combinant des simulations numériques CFD et une série de mesures expérimentales à base d'un dilatomètre à haute résolution. Des simulations transitoires CFD 3D validées par des mesures expérimentales de températures ont été utilisées pour évaluer l'impact des modèles de chargement et du calage (positionnement des cales) sur l'uniformité de la température et le temps de résidence des pièces forgées dans le four. Une analyse transitoire complète des caractéristiques de chauffage des pièces forgées (y compris une analyse des modes de transfert de chaleur) en utilisant quatre configurations de chargement différents a permis de quantifier l'impact des

calages et leurs dimensions sur l'uniformité de la répartition de la température ainsi que sur le temps de séjour des produits. Les résultats ont montré que la non-uniformité de température peut aller jusqu'à 331 K pour un modèle de chargement conventionnel (non optimisé). L'influence positive de l'utilisation des cales et des espaceurs (cales entre les brames) a été approuvée et quantifiée à l'aide de l'approche développée. Il a été possible de réduire les non-uniformités identifiées jusqu'à 32% en modifiant la configuration du chargement à l'intérieur du four de traitement thermique. Cette approche hybride a permis de déterminer le temps de séjour optimal pour les lingots, et aussi permettre son amélioration jusqu'à peu près de 15,5% par rapport à la configuration classique (non optimisée). Cette approche a été validée et pourrait s'appliquer directement à l'optimisation de différents cycles de traitement thermique de pièces forgées de grande taille.

Enfin, la troisième partie de l'étude aborde les détails de la simulation numérique du procédé de traitement thermique de pièces forgées de grande taille dans des fours à gaz à échelle réelle. Plus précisément, l'évaluation du modèle de combustion non-premix avec l'équilibre chimique pour prévision précise de la température des pièces forgées, ainsi que les performances de six modèles de turbulence différents de RANS pour les projections d'analyse thermique sont discutés. À cet égard, les interactions thermiques à différents endroits du bloc forgé et dans des régions critiques telles que la région du brûleur, la stagnation et la région de sillage ont été réalisées à l'aide d'un modèle 3D périodique du four puis validé par des mesures expérimentales. Les résultats ont montré que le modèle périodique avec combustion non-premix est fiable pour l'analyse thermique du processus de traitement thermique avec un écart maximal d'environ 3% par rapport aux mesures expérimentales. Il a également été révélé que le choix du modèle de turbulence avait un effet significatif sur la prévision de la combustion et du transfert de chaleur autour du bloc. La prédiction du rapport ε/k par différents modèles de turbulence a montré une relation significative avec la combustion turbulente (telle que la longueur de la flamme du brûleur) et les prévisions de température du bloc, autour de la région de stagnation. Les modèles $k-\varepsilon$ Standard et réalisable en raison d'une prévision irréaliste de l'énergie cinétique de turbulence (sous-prévision du rapport ε/k) ont entraîné une longueur de flamme plus courte et une sous-prévision de la température du bloc forgé autour de la région de stagnation. En suite, le modèle SST $k-\omega$ a montré des prévisions raisonnables dans cette région. Le modèle RSM s'est révélé être le modèle de turbulence le plus fiable par rapport aux mesures expérimentales. De plus, un modèle $k-\varepsilon$ réalisable, mis à part une sous-prédiction sur la région de stagnation et la longueur de la flamme, pourrait efficacement prédire la température globale des pièces forgées lourdes avec une précision comparable à celle des données expérimentales et des prévisions du RSM.

Mots-clés: Traitement thermique, simulation CFD, four à gaz, mesures de température, uniformité de la température, modélisation du rayonnement, configuration du chargement,

temps de résidence, mesures expérimentales, approche hybride, modélisation de la turbulence, modélisation de la combustion,

Optimization of furnace residence time and ingots positioning during the heat treatment process of large size forged ingots

Nima BOHLOOLI ARKHAZLOO

ABSTRACT

High-strength large size forgings which are widely used in the energy and transportation industries (e.g., turbine shaft, landing gears etc.) acquire significant mechanical properties (e.g., hardness) through a sequence of heat treatment processes, called Quench and Temper (Q&T). The heating process (tempering) that takes place inside gas-fired furnaces has a direct impact on the final properties of the product due to several major microstructural changes taking place at this step. Therefore, material properties are usually optimized by controlling the tempering process parameters such as time and temperature. A non-uniform temperature distribution around parts, as a result of thermal interactions inside the furnace or loading pattern, may result in the parts property variations from one end to another, changes in microstructure or even cracking. On the other hand, improvement of large products residence time inside the heat treatment furnace can minimize energy consumption and avoid undesirable microstructural changes. However, at the present time, the industrial production is mainly based on available empirical correlations which are costly and not always reliable. Accurate time-dependent temperature prediction of the large size forgings within gas-fired heat treatment furnaces requires a comprehensive quantitative examination of the heating process and an in-depth understanding of complex conjugate thermal interactions inside the furnace. Limitations in analytical studies and complexity and cost of experimentations have made numerical simulations such as computational fluid dynamics (CFD), effective methods in this field of study. However, among the rarely found studies on gas-fired furnaces, small-scale furnaces or those with shorter operation times were mainly considered (using different simplifications like steady-state calculations) because of complexity of the phenomena and large calculation times. Subsequently, there are very few studies on the improvement of the loading patterns of large-size steel parts inside the gas-fired furnaces and their relevant residence time optimization. Moreover, the limitation and strength of different numerical approaches to calculate thermal interactions in the turbulent reactive flow of the large size gas-fired batch type furnaces were addressed by few researchers in the literature. In this regard, the main objective of the present thesis is to provide a comprehensive quantitative analysis of transient heating and an understanding of thermal interactions inside the furnace so as to optimize the residence time and temperature uniformity of large size products during the heat treatment process. To attain this objective, the following milestones are pursued.

The first part of this study provides a comprehensive unsteady analysis of large size forgings heating characteristics in a gas-fired heat treatment furnace employing experimentally measured temperatures and CFD simulations. A three-dimensional CFD model of the gas-fired furnace, including heat treating chamber and high momentum natural gas burners, was generated. The interactions between heat and fluid flow consisting of turbulence, combustion and radiation were simultaneously considered using the k-ε, EDM and DO models,

respectively. The applicability of S2S radiation model to quantify the effect of participating medium and radiation view factor in the radiation heat transfer was also assessed. Temperature measurements at several locations of an instrumented large size forged block and within the heating chamber of the furnace were performed for experimental analysis of the heating process and validation of the CFD model. Good agreement with a maximum deviation of about 7% was obtained between the numerical predictions and the experimental measurements. The results showed that despite the temperature uniformity of the unloaded furnace, each surface of the product experienced different heating rates after loading (single loading) resulting in temperature differences of up to 200 K. Analysis of the results also revealed the reliability of the S2S model and highlighted the importance of radiation view factor for the optimization purposes in this application. Findings were correlated with the geometry of the furnace, formation of vortical structures and fluid flow circulations around the workpiece. The experimental data and CFD model predictions could directly be employed for optimization of the heat treatment process of large size steel components.

The second part of this study aims to determine the effect of loading pattern (in the multiple loading configurations) on the temperature distribution of large size forgings during the heat treatment process within a gas-fired furnace to attain more temperature uniformity and consequently homogenous mechanical properties. This part also focuses on the improvement of residence time of large size forged ingots within a tempering furnace proposing a novel hybrid methodology combining CFD numerical simulations and a series of experimental measurements with high-resolution dilatometer. Transient 3D CFD simulations validated by experimental temperature measurements were employed to assess the impact of loading patterns and skids on the temperature uniformity and residence time of heavy forgings within the furnace. Comprehensive transient analysis of forgings heating characteristics (including heat transfer modes analysis) at four different loading patterns allowed quantifying the impact of skids and their dimensions on the temperature distribution uniformity as well as products residence time. Results showed that temperature non-uniformities of up to 331 K persist for non-optimum conventional loading pattern. The positive influence of skids and spacers applications was approved and quantified using the developed approach. It was possible to reduce the identified non-uniformities of up to 32 % through changing the loading pattern inside the heat treatment furnace. This hybrid approach allowed to determine an optimum residence time of large size slabs improving by almost 15.5 % in comparison with the conventional non-optimized configuration. This approach was validated and it could be directly applied to the optimization of different heat treatment cycles of large size forgings.

The third part of the study addresses the details of the numerical simulation of heat treatment process of large size forgings within real scale gas-fired furnaces. Specifically, assessment of chemical equilibrium non-premix combustion model for accurate temperature prediction of heavy forgings, as well as performance of six different RANS based turbulence models for predictions of turbulent phenomenon were discussed in this context. In this regard, thermal interactions at different locations of the forged block as well as critical regions such as burner area, stagnation and wake region were performed using a one-third periodic 3D model of the furnace and validated by experimental measurements. Results showed that the one-third periodic model with chemical equilibrium non-premix combustion is reliable for the thermal

analysis of the heat treatment process with a maximum deviation of about 3% with respect to the experimental measurements. It was also revealed that the choice of the turbulence model has a significant effect on the prediction of combustion and heat transfer around the block. Prediction of ε/k ratio by different turbulence models showed a significant relation to the turbulent combustion (such as burner flame length) and block temperature predictions, around the stagnation region. Standard and realizable $k-\varepsilon$ models, due to an unrealistic over prediction of turbulence kinetic energy (under-prediction of ε/k ratio), resulted in shorter flame length and under-prediction on the temperature of the forged block around the stagnation region; While, SST $k-\omega$ model showed reasonable predictions in this region. RSM model was found as the most reliable turbulence model compared to the experimental measurements. Meanwhile, realizable $k-\varepsilon$ model apart from some under-prediction on the stagnation region and flame length could effectively predict the overall temperature of the heavy forgings with reasonable accuracy with respect to the experimental data and RSM predictions.

Keywords: Heat treatment, CFD simulation, Gas-fired furnace, Temperature measurements, Temperature uniformity, Radiation modeling, Loading pattern, Residence time, Experimental measurements, Hybrid approach, Turbulence modeling, Combustion modeling

TABLE OF CONTENTS

LIST OF TABLES

Page

LIST OF FIGURES

Page

LIST OF ABBREVIATIONS

2D	Two dimensional
3D	Three dimensional
CFD	Computational Fluid Dynamics
DO	Discrete ordinates model
DSK	Double Skid
DSKC	Double skid + Central spacer skid
DTRM	Discrete Transfer Radiation Model
HRC	Rockwell C hardness
EDM	Discrete ordinates model
EDC	Eddy dissipation concept
Q&T	Quench and temper
RANS	Reynolds-averaged Navier–Stokes equations
RNG	Re-normalization group
RSM	Reynolds stress model
RFL	Rich Flammability Limit
RTE	Radiative transfer equation
RTE	Radiative transport equation
S2S	Surface to surface
SK	Single Skid
SKC	Single Skid + Central spacer skid
SST	Shear stress transport
TC	Thermocouple
TKE	*Turbulence kinetic energy*
WSGGM	Weighted-sum-of-gray-gases model

LIST OF SYMBOLS

Latin symbols

a	Absorption coefficient
A	Surface (^{m2})
d	Characteristic dimension (m)
D_t	Turbulence diffusivity
$C_{1\varepsilon}$,$C_{2\varepsilon}$,$C_{3\varepsilon}$	Constants in $k-\varepsilon$ equations
C_g, C_d	Constants in mixture fraction variance transport equation
E	Energy (J)
F_{ij}	View factor between surface k and surface j
$\overline{f}$	Mean Mixture fraction
$\overline{f}'^2$	Mixture fraction variance
G_k	Turbulence kinetic energy production due to velocity gradient
G_b	Turbulence kinetic energy production due to buoyancies
G_ω	Eddy dissipation rate production due to velocity gradient
g	Gravity (m/s^2)
J_i^z	Diffusive flux of chemical species
h	Enthalpy (J/kg)
h_0	Convection heat transfer coefficient ($W/m^2.K$)
H	Block height
I	Radiation intensity
K	Conductivity ($W/m.K$)
k	Turbulence kinetic energy (m^2/s^2)
k_{eff}	Effective thermal conductivity
L	Furnace length in longitudinal direction
l_s	Turbulence length scale
m^g	Mass flux ($kg/m^2.s$)
n	Refractive index

XXX

OH	Hydroxide
p	Pressure (Pa)
q_i	The generic source term
q_r	Reaction heat term
q_s	The generic source term
$\vec{r}$	Position vector
R_z	Production rate of z_{th} component
R_r	Net production of a specie in a reaction
$R_{z,r}$	Production rate of z_{th} component
Re	Reynolds number (ud/μ)
s	Path length
$\vec{s}$	Direction vector
$\vec{s}'$	Scattering direction vector
S_z	Source term of z_{th} component production
Sc	Schmidt number
t	Time (s)
T	Temperature (K)
t_T	Total heat treatment time
u_i	Reynolds-averaged velocity in tensor notation
u_i'	Resolved fluctuating velocity components
$\bar{U}$	Time averaged velocity
V_s	Velocity scale
$X, \mathrm{Y}, \mathrm{Z}$	Direction of coordinate axes
Y_i	Mass fraction of $\mathrm{i_{th}}$ specie in the reaction

Greek symbols

ε	Turbulence dissipation rate (m^2 / s^3)
ε_k	Surface emissivity
ν	Kinematic Viscosity (m^2 / s)
μ_t	Turbulence eddy viscosity ($kg.m / s$)
Γ_k	Turbulence kinetic energy diffusion coefficient
Γ_k	Eddy dissipation rate diffusion coefficient
ρ	Density (kg / m^3)
ρ_k	Surface reflectivity
$\sigma_k, \sigma_\varepsilon$	Prenatal number for the kinetic energy and dissipation rate respectively
σ_t	Constant in mixture fraction variance equation
σ, σ_s	Stefan-Boltzmann constant and scattering coefficient
$\rho\overline{u_i' u_j'}$	Reynolds stress ($kg / \mathrm{m}.s^2$)
Ω'	Solid angle
ω	Specific dissipation rate
ϕ	Phase function
λ	Wavelength
τ_{ij}	Viscous stress tensor

Superscripts

'	Fluctuations with respect to a Reynolds averaging
-	Time averaging function
$\rightarrow$	Vector

Subscripts

b	Black body

h	Hot
i, j, k	Tonsorial indices
O	Out
ox	Oxygen
R	Combustion reaction
Sec	Secondary
s	Source
T	Total
t	Turbulence
z	z_{th} species
λ	Spectral parameter

Abbreviation

3D	Three dimensional
CFD	Computational Fluid Dynamics
DO	Discrete ordinates model
DSK	Double Skid
DSKC	Double skid + Central spacer skid
EDM	Discrete ordinates model
HRC	Rockwell C hardness
RANS	Reynolds-averaged Navier–Stokes equations
RNG	Re-normalization group
RSM	Reynolds stress model
RFL	Rich Flammability Limit
RTE	Radiative transfer equation
RTE	Radiative transport equation
SST	Shear stress transport
SK	Single Skid
SKC	Single Skid + Central spacer skid
TKE	Turbulence kinetic energy

INTRODUCTION

A significant number of high-strength steel parts such as medium-carbon low-alloy steel used for different critical applications in energy and transportation, such as turbine shafts and landing gears, acquire their required properties through a sequence of heat treatment processes often called Quench and Temper (Q&T) (Bhadeshia & Honeycombe, 2017). This is to attain some important properties such as hardness, toughness, corrosion resistance and so on. Optimum process, which is an operation including the controlled heating and cooling of metals and alloys in the solid state to obtain specific mechanical characteristics, is a critical point and one of the most important parts of metallurgical engineering procedures. The Tempering (a heating process after the initial casting and open die forgings) is one of the most vital steps of the heat treatment having a direct influence on final delivered mechanical properties of the products (Totten, 2006).

Generally, gas-fired furnaces are used in the steel plants to carry out the tempering process. Heat transfer to the products primarily depends on temperature distribution inside the furnace and it significantly affects the quality of the final part. Besides, the time of tempering directly affects the acquired mechanical properties after the process. Hence, temperature and time are usually used to optimize the final material properties of the products. The problem becomes more acute and critical when it comes to the heat treatment of large size products for energy and transportation industries (Bohlooli Arkhazloo et al., 2019).

A non-uniform temperature distribution may result in the property variation from one end to another of the part, changes in microstructure, or even cracking. Different locations of blocks inside the furnace, considering their mutual heat transfer and also between the blocks and the heat sources may experience non-uniform heat transfer and consequently a non-uniform heat treatment. Improvement of the loading patterns within the furnace can significantly increase the temperature uniformity of the product during the process. Besides, it can also reduce the residence time of products by increasing the heating rates of the work piece as a result of changing in the heat transfer pattern.

On the other hand, reduction of residence time of large products inside the heat treatment furnace can minimize energy consumption and avoid undesirable microstructural changes. Required time for only one step of different stages of heat treating process can be more than 62 hours in the case of large size products (Gur & Pan, 2008). Therefore, optimization of forgings ingots residence time inside gas-fired heat treating furnaces is of great importance in the steel making industry. This improvement not only provides a better treatment, but also leads to a cost effective production. The importance of residence time is more notable where a significant number of large size ingots should be treated every day. In other words, even a small reduction in the residence time of one product can lead to a considerable energy savings. Thus, predicting and controlling the products' transient temperature is an essential task in the heat treatment process both from the performance and the cost points of view.

The current practice in industry for the heating cycle schedule is based on empirical correlations and is mostly limited to monitoring of the furnace temperature as a function of the furnace load (Zhang, Wen, Bai, Chen, & Long, 2009). Empirical correlations, however, cannot be used to accurately predict temperature distribution in the products and very often large deviations with the loading pattern or furnace configurations, are observed (Gur & Pan, 2008; Hao, Gu, Chen, Zhang, & Zuo, 2008; Wang et al., 2008).

Therefore, accurate time-dependent temperature prediction of the large size parts inside the gas-fired heat treatment furnaces necessitates a quantitative examination of the transient heating and comprehending of thermal interactions within the furnace. This analysis can deliver information about the temperature evolution of products and improvement of temperature uniformity, residence time and loading pattern of large-size steel parts in gas-fired heat treating furnaces. However, understanding the complexities of the thermal interactions along with the turbulent flow field as well as combustion and radiation within the gas-fired heat treatment furnace is very challenging. These phenomena imposing strong non-linear thermal boundary conditions make the analytical studies, which are generally limited to linear problems, very complex and insufficient for accurate predictions (Gao, Reid, Jahedi, & Li, 2000). On the other hand, experimentation of large-size products in the large scale

furnaces and reliable data acquisition is very challenging and expensive. Recently, computational fluid dynamics (CFD) offering simultaneous analysis of turbulent fluid flow, combustion and conjugate heat transfer has been employed to study large size industrial furnaces (Chattopadhyay, Isac, & Guthrie, 2010). Different furnaces such as electrically heated or gas quenching ones have been studied using CFD. However, very few studies focus on the simulation of large-size heat treatment inside gas-fired batch-type furnaces due to their complexity, as a result of reactive flow combined with turbulent transport process and conjugate heat transfer including absorbing and emitting hot combustion products and long processing. Hence, the number of published papers in the case of heat treatment furnaces is few and most of the limited numerical studies have been devoted to one aspect of the process (i.e., furnace chamber and its details such as burners or product heating characteristics, solely) rather than simultaneous analysis of furnace thermal interactions (such as turbulent combustion and radiation heat transfer) and its details including the product.

Considering the importance of accurate transient temperature prediction of large-size products inside the gas-fired heat treatment furnaces and the lack of relevant information, the first objective of the present thesis was on the experimental analysis and CFD simulations of large-size products' heat treatment inside gas-fired furnaces. Comprehensive analysis of the conjugate heat transfer in the heat treatment process as well as identification of a correlation between non-uniformity sources including furnace geometrical parameters (size, location of burners and skids), loading pattern and vortical structures inside the furnace was other secondary objectives of this study.

There are few studies on the improvement of large-size steel parts loading patterns inside the gas-fired furnaces and their relevant residence time optimization. Therefore, investigation of the loading patterns effect on temperature uniformity of large size forged ingots as well as reduction of residence time inside the large size gas-fired furnaces, were other objectives of the present thesis.

Due to the lack of enough systematic evaluation of the strengths and limitations of different CFD approaches for the prediction of thermal interactions within the furnace, including turbulence and combustion, the fourth objective of the present study was set to address this limitation in the literature. In other words, finding an accurate combination of CFD models that could deliver reliable prediction of burner domain (flow field) and product temperature (scalar) with reasonable computational cost was the fourth objective of the present study. A detailed analysis of turbulent combustion phenomena in the furnace was another secondary objective of this part.

The present thesis is organized, as follows:

1. The thesis starts with an overview on the heat treatment process of large-size forgings inside gas-fired furnaces in chapter 1. Different thermal interactions involved in the heat treatment and their relative numerical approaches to be predicted by the CFD simulation are discussed. Finally, the state-of-the-art on the analysis of heat treatment of large size products inside gas-fired furnaces, their loading pattern and residence time as well as numerical approaches to predict the process are identified.

2. Chapter 2 presents the details of the numerical approaches employed for simulating the thermal interactions inside the gas-fired furnace. After a mathematical description of each model, strengths and limitations of different approaches are discussed.

3. The elaboration of the industrial and laboratory scale experimental measurements are presented in chapter 3. Details of instrumentations and measurements in a real scale gas-fired heat treatment furnace (loaded large size forged ingots), as well as laboratory scale experimentations are presented. Also, details of a calibration test process to evaluate the measurement accuracy and employed thermo-physical properties are discussed in this chapter.

4. Chapter 4 focuses on the experimental and numerical analyses of large size forgings transient heating inside the gas-fired heat treatment furnace in the single loading

configuration. Heat transfer histories of different locations of the parts inside the furnace as well as temperature uniformity analysis of the forgings based on the analysis of conjugate heat transfer are presented. Details of the cause of temperature non-uniformities including furnace geometrical design, loading pattern and fluid flow circulation and their correlation with heat transfer modes (radiation, convection) are discussed.

5. Chapter 5 discusses the effect of loading pattern on the temperature homogeneity of the large-size products during the heat treatment process. The chapter also proposes a new hybrid methodology (including CFD simulation and experimental measurements) to optimize the residence time of large size forgings inside the heat treatment furnace during different stages of tempering.

6. Chapter 6 presents details of CFD simulation of a gas-fired furnace comparing different numerical approaches to predict the thermal interactions inside the gas-fired heat treatment furnace. Details of turbulence and combustion modeling and their relative strengths and limitations in this particular application are discussed. Finally, after comprehensive analysis of numerical techniques, a computationally effective methodology to predict the heat treatment process of large-size forgings inside gas-fired heat treatment furnaces is proposed.

A summary covering all the concluding remarks concerning chapters 4 to 6 is presented in the Conclusions section to link the outcomes of the thesis and present original contributions of the study toward the thesis initial objectives.

CHAPTER 1

LITERATURE REVIEW

1.1 Steel Heat Treatment

Heat treatment is a process that encompasses the controlled heating and cooling of metals and alloys in the solid state to achieve certain mechanical characteristics such as hardness, strength, flexibility, machinability and reduction of residual and internal stresses. The heat treatment process takes place based on the steel microstructural transformation as a function of temperature and chemical composition of an alloy (Bhadeshia & Honeycombe, 2017) (See Fig. 1.1).

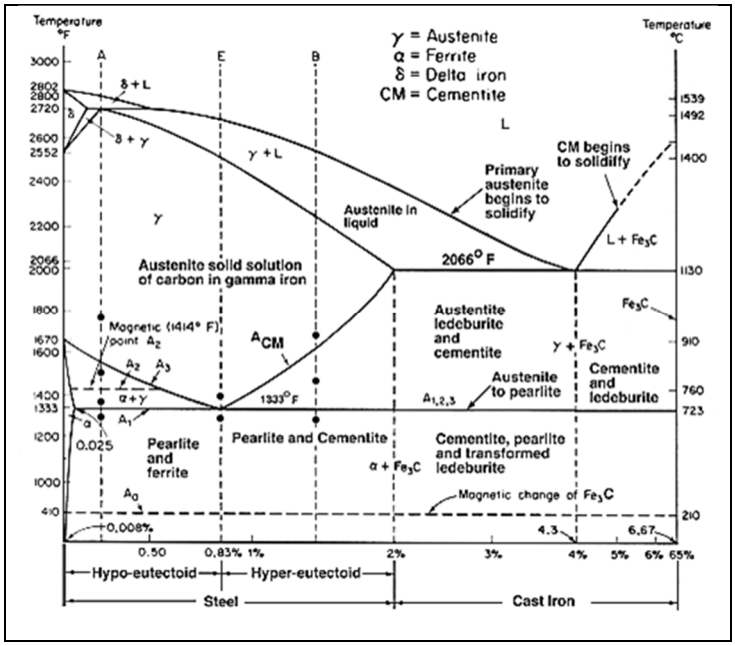

Figure 1.1 Iron-Carbon phase diagram (Pollack, 1988).

1.2 Tempering Process

Tempering is a thermal treatment process that is often carried out in gas-fired heat treatment furnaces (for large-size product) after the quench. The aim is to modify the microstructure of

the quenched part to acquire desired mechanical properties such as hardness, toughness, ductility and dimensional stability (Speich & Leslie, 1972). The main two parameters that control the tempering process are temperature and time at temperature. Depending on chemical composition of a specific steel, its primary microstructure, and heating rate, different microstructural changes takes place during certain temperature intervals and time. Inaccurate selection of time and temperature of tempering can affect final mechanical properties and can even produce cracks in the part (Canale, Yao, Gu, & Totten, 2008). There are several methods to determine proper time and temperature of the tempering process. Methods like Liščić and Filetin' correlation (Liščić & Filetin, 1987) using linear regression analysis for a specific temperature range of tempering have been used to calculate the tempering temperature-time condition. Other methods like Holloman-Jaffe equation (Totten, 2006) were developed to predict the hardness of tempered steel parts. In all these equations, having an accurate prediction of parts' temperature during the heating up to the target temperature (non-isothermal tempering) and soaking at the temperature (isothermal tempering) is important.

1.3 Heat Treatment Furnaces

Heat treatment furnace that provides the heat treatment medium inside, is one of the most vital equipment of heat treatment procedure which should be comprehensively studied to achieve optimum heat treatment of metals. There are several types of heat treatment furnaces that can be categorized based on their shape and movement of products within them (such as box furnaces, pit furnaces or tip-up furnaces) or the energy used in them (like electrical heated furnace or gas-fired heat treatment furnaces). Among different types of furnaces Gas-fired heat treatment furnaces are extensively used for large-size high-strength steel products such as medium-carbon low-alloy steels for different critical applications in the energy and transportation industries. Natural gas usage in these furnaces provides the increased heat treatment rate and reliable burning (Totten, 2006). Final material properties are usually optimized by tempering parameters modification (such as temperature, time, etc.) in these heat treatment furnaces (Yan, Han, Li, Luo, & Gu, 2017). To analyze these furnaces, burners

which provide the heat input as a result of combustion of the natural gas by oxygen should be studied comprehensively (Purushothaman, 2008).

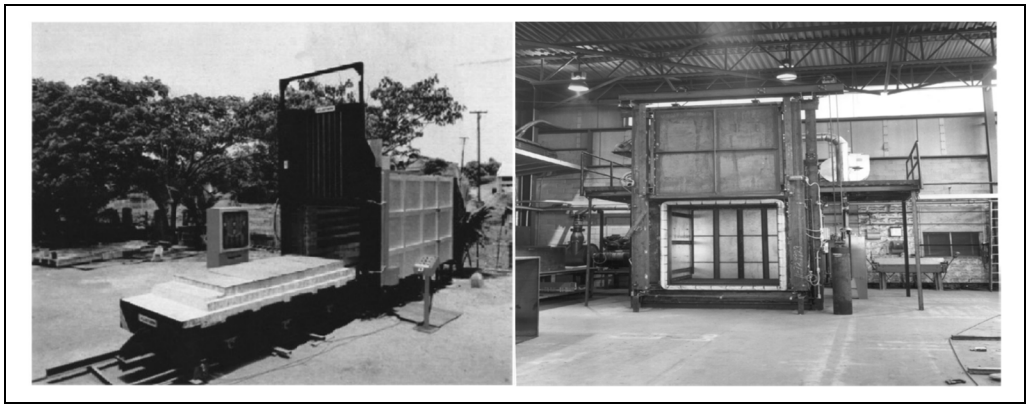

Figure 1.2 (Right): Car-bottom gas-fired heat treatment furnace and (Left): electrically heated box type heat treatment furnace.

1.4 Tempering of Large Size Parts

Large-size products, due to the significant temperature variation between their surface and center, contain different microstructures which in turn response differently to the tempering process (Talebi, Ghasemi-Nanesa, Jahazi, & Melkonyan, 2017). Besides, non-uniform temperature distribution in such parts within gas-fired furnaces may result in non-uniform properties in different locations of the final product or even cracking. Therefore, temperature distribution uniformity is of great importance for the quality of the final products (Gao et al., 2000; Gur & Pan, 2008). Further, due to their large sizes a lot of energy is used in these furnaces (Kang & Rong, 2006; B. Mayr, Prieler, Demuth, Moderer, & Hochenauer, 2017). Therefore, predicting, controlling and subsequently optimizing the temperature distribution of such parts is a necessary task to increase the product quality and reduce the production cost (Hao et al., 2008). However, an exact prediction of the furnace temperature distribution and, consequently, the temperature experienced by the product is difficult and the heating cycle schedules are mainly based on the available empirical correlations (Kang & Rong, 2006). These correlations are usually valid for specific ranges of temperature and defined as a function of the furnace load and simple loading patterns of the parts inside the furnace

(Canale et al., 2008; Korad, Ponboon, Chumchery, & Pearce, 2013). Hence, large deviations in the case of large-size products multiple loading patterns are observed (Cheng, Brakman, Korevaar, & Mittemeijer, 1988; Gao et al., 2000; Primig & Leitner, 2011). On the other hand, most of the metallurgical studies assume a constant heating rate in different locations of the part, which is far from the reality and proves the need for accurate determination and prediction of temperature evolution inside the gas-fired heat treatment furnaces and subsequent analyses based on these temperature profiles.

An accurate temperature prediction of parts necessitates a quantitative analysis of thermal interactions and their subsequent roles on the transient heating of large size parts inside gas-fired heat treatment furnaces as detailed in the following sections.

1.5 Thermal Interactions inside a Gas-Fired Furnace

Heat is a form of energy that exchanges between several mediums due to temperature differences. This transfer of energy which always takes place from the higher temperature field to the lower one, according to the first law of thermodynamics, is the basis of the heat transfer (Incropera, Lavine, Bergman, & DeWitt, 2007). Gas-fired heat treatment furnaces transfer heat to the different location of parts through the three modes of heat transfer: radiation, convection and conduction. As it can be seen in the schematic view of interactions inside a heat treating furnace (Fig. 1.3) the three modes of heat transfer are playing their role in a conjugate situation. Therefore, any analytical, experimental or numerical study should consider the conjugate heat transfer to analyze the heat transfer rates. It should be noted that these heat transfer modes take place in combination with the two main fluid flow related interactions (combustion and turbulence) which will be discussed in the following sections.

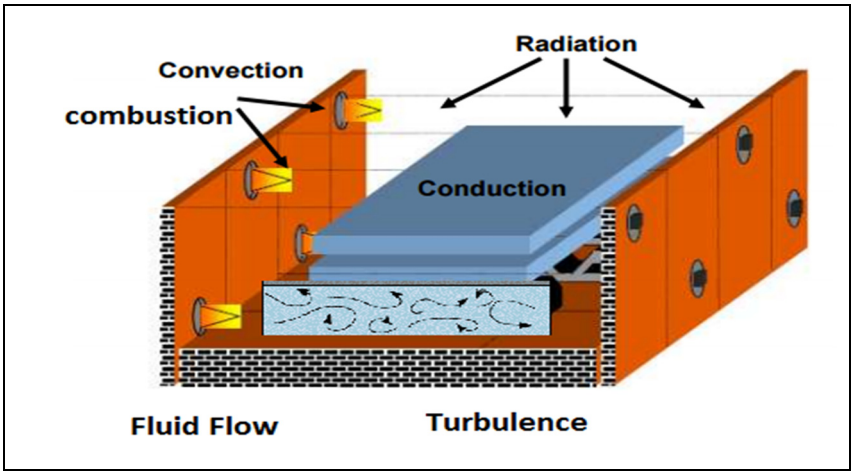

Figure 1.3 Thermal interactions and conjugate heat transfer within a gas-fired heat treatment furnace.

1.5.1 Conduction

The conduction heat transfer is the most significant mode in a solid medium. The heat transfer rate through a planar layer according to the Fourier's law is:

$$\dot{Q}_x = -kA\frac{dT}{dx} \tag{1.1}$$

In this equation, k, as thermal conductivity, is the material property that represents the ability to conduct the heat in a material whether solid or fluid flow. Thermal conductivity of many materials changes with temperature. This is also true for other thermo-physical properties of material like specific heat. For instance, Fig. 1.4 shows the variation of a carbon steel thermal conductivities and specific heats over a wide range of temperatures used by Tang et al. (Tang et al., 2017) in their study. JMatPro software (Danon, Cho, De Jong, & Roekaerts, 2011) was reported to be a reliable tool for the calculation of temperature dependent thermal conductivities of different alloys (B. Mayr, Prieler, Demuth, Moderer, et al., 2017; Prieler, Mayr, Demuth, Holleis, & Hochenauer, 2016; Tang et al., 2017).

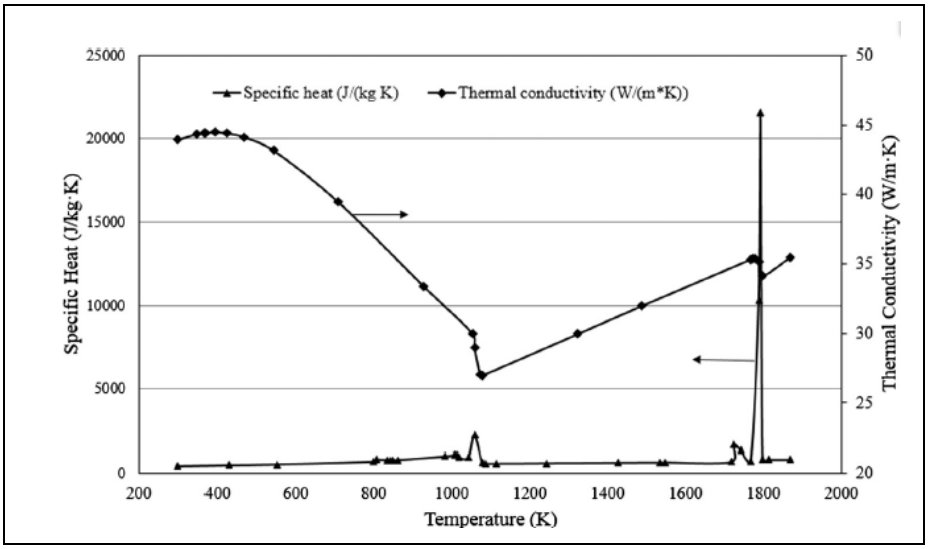

Figure. 1.4 Temperature dependant thermal conductivity of a steel slab (Tang et al., 2017).

1.5.2 Convection

The Newton's rule of cooling describes the rate of convection heat transfer (the heat transfer that is actuated by the flow motion usually takes place with the mass transfer), $\dot{Q}_{conv}$, based on the temperature gradient, the differences between the hot surface (T_h) and the ambient fluid temperature (T_a) and the heat transfer area, A_s are as below:

$$\dot{Q}_{conv} = h_o A_s \left(T_h - T_a \right) \tag{1.2}$$

In this equation h_o is the convection heat transfer coefficient. Several investigations in the heat treatment field show that the convection heat transfer plays an important role in the heat transfer in this process (Bhadeshia & Honeycombe, 2017; Totten, 2006). Although in some furnaces such as electrically heated vacuum furnaces (Gao et al., 2000) the convection heat transfer can be neglected, in majority of the furnaces the convection can be considered as a significant phenomenon in the process. This heat transfer mode is dominant, especially at low temperatures where the furnace undergoes the heating to reach to the soaking temperature. The convection heat transfer is highly correlated with turbulence in turbulent fluid flow.

1.5.3 Radiation

Radiation heat transfer is the energy emitted by the matter (photons) in the form of electromagnetic waves due to changes in the electronic configuration of atoms as a result of temperature in vacuum (without the presence of matter) or transparent mediums (solid and fluid). The Stefan-Boltzmann law for a black surface, calculates the total radiated energy per unit surface area per unit time (E_b) as a function of the fourth power of object's (black body) temperature as follows (Howell, Menguc, & Siegel, 2015):

$$E_b = \sigma T^4 \tag{1.3}$$

Where the temperature is in Kelvin and $\sigma = 5.67\times10^{-8}\, Js^{-1}m^{-2}K^{-4}$ is the Stefan-Boltzmann constant. For the gray body which does not absorb or emit the full amount of radiation and normally radiates a small amount of that, the total energy, considering the emissivity, becomes (Incropera et al., 2007):

$$\dot{Q} = A\varepsilon\sigma\left(T_a^4 - T_b^4\right) \tag{1.4}$$

The radiative transfer equation (RTE) in a medium that participates in the radiation heat transfer (a medium with absorption, emission, and scattering effect) can be formulated as follows (Danon et al., 2011):

$$\frac{dI(\vec{r},\vec{s})}{ds} + (a+\sigma_s)\,\mathrm{I}(\vec{r},\vec{s}) = an^2\frac{\sigma T^4}{\pi} + \frac{\sigma_s}{4\pi}\int_0^{4\pi}\mathrm{I}(\vec{r},\vec{s})\phi(\vec{s},\vec{s}')d\Omega' \tag{1.5}$$

Where *I* is the radiation intensity and ($a+\sigma_s$) represents the optical thickness of the medium. The definition of all the variables and related units are provided in the nomenclature section.

1.5.4 Combustion

Hydrocarbon fuel sources such as methane or natural gas can react with oxygen to provide combustion and subsequently thermal energy or heat.

$$CH_4 + 2O_2 \rightarrow CO_2 + 2H_2O \tag{1.6}$$

The oxygen availability and operating temperature can change the combustion efficiency and also the combustion products. Incomplete combustion and CO production will take place in combustion with insufficient oxygen content. Besides, the excess air, which means excess oxygen, can affect the ratio of available heat. Combustion in any gas-fired heat treatment furnaces plays the most important role in the system because:

- Combustion facilitator devices such as burners can be considered as the inlet boundary condition for the main system such as a furnace.
- Combustion has a direct interaction with the radiation, convection and turbulence which have their own impacts on the final goal.

Therefore, the combustion prediction in any combustion included application such as gas-fired heat treatment furnaces should be thoroughly investigated.

1.5.5 Turbulence

Almost all fluid flows which we encounter in the world are turbulent. Turbulent flows can be usually observed in numerous natural and industrial cases like impingement flows or burner combustions (Fig. 1.5). The boundary layers and the wakes around and after bluff bodies such as cars, airplanes, buildings and large-size steel parts in the heat treatment furnaces are turbulent. In the turbulent flow field of study, the parameters such as velocity are decomposed in two parts of a time-averaged, $\overline{U}_i$, which is independent of time (when the average flow is steady), and a fluctuating part, $\acute{u}_i$, which means that $u_i = \overline{U}_i + \acute{u}_i$. There is no exact definition of turbulent flow, but it has a number of characteristic features such as irregularity, continuity, diffusivity, large Reynolds numbers, a three-dimensional nature (Cant, 2001; Tennekes, Lumley, & Lumley, 1972). These characteristics can be found in several gas-fired heat treatment furnaces which are designed to have a self-induced turbulence. The high momentum of combustion products, with a large Re number, are in continuum interactions and provide 3D circulation inside the furnace.

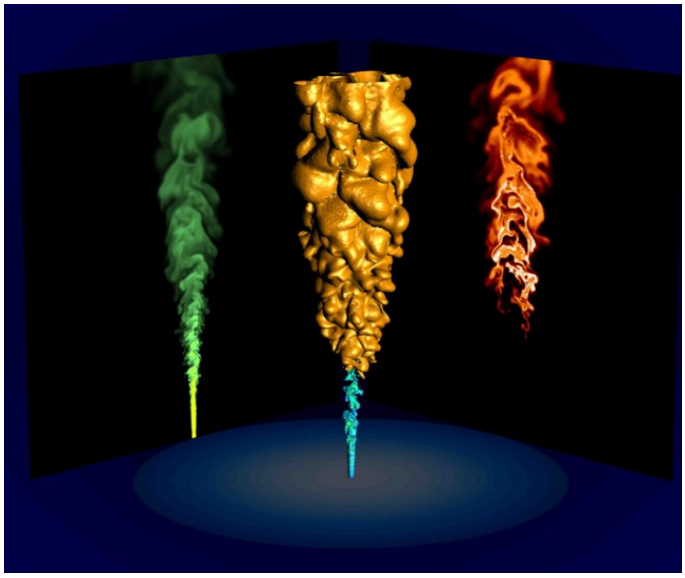

Figure 1.5 Turbulent combustion visualized by numerical simulation (Vicquelin, 2010).

1.6 Thermal Interactions Analyses inside Heat Treatment Furnaces

1.6.1 Analytical and Semi-Analytical Studies

Thermal interactions inside the gas-fired heat treatment furnaces importing strong non-linear thermal boundary conditions to the loads make the thermal analysis of heat treatment process very difficult. In the literature Chapman et al. (Chapman, Ramadhyani, & Viskanta, 1990) in a semi-analytical study, assessed various material properties on the efficiency of heat treating process in a direct fired batch reheating furnace. Gao et al. (Gao et al., 2000) using heat conduction rule in solids, developed an analytical, practical virtual sphere method to estimate the equilibrium time and heating/cooling rate in heat treatment furnaces. Their results proved that the convection heat transfer rate could significantly differ from the empirically calculated h values for specific furnaces. Singh et al. (Singh, Talukdar, & Coelho, 2015) in their semi-analytical studies developed a heat-flow model to estimate temperature evolution of products in different heat treatment processes such as heating in electrically furnaces, air and water quenching. However, analytical analyses are generally limited to linear problems

and they become very complicated in gas-fired furnaces where strong non-linear transient condition and interactions are present.

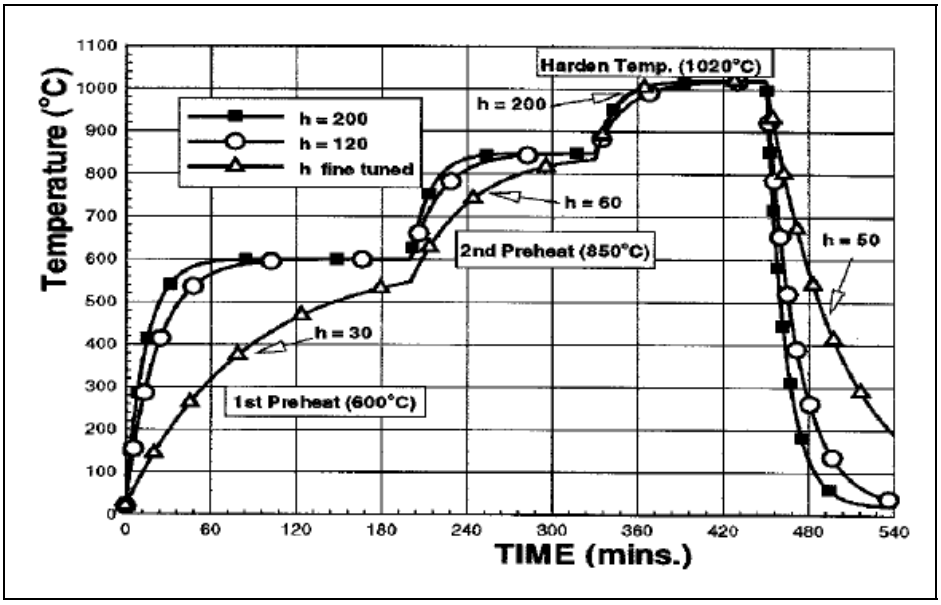

Figure 1.6 Prediction of heating and cooling rates with different convection heat transfer coefficients (Gao et al., 2000).

Although the advantage of these types of studies is in their simplicity and applicability in different case studies, the fact that the today's industry needs reliable and optimal data for optimization of product quality and product price, illustrates the need for studies with more details and accuracy. The need for specification of real convection heat transfer coefficient, accurate combustion prediction and suitable radiation simulation to provide a better optimization of time residency and positioning plan, specify the value of high order numerical simulations in this field of study.

1.6.2 CFD Studies

In this context, major advances have been made in development of high performance computational facilities allowing for the simulation of large size furnaces. Studies such as those of Jaklic et al. (Jaklič, Glogovac, Kolenko, Zupančič, & Težak, 2002) and Tagliafico et

al. (Tagliafico & Senarega, 2004) using finite-difference and finite element based methods added more details to the analysis of load-furnace heating characteristics. Recently, computational fluid dynamics (CFD) offering simultaneous analysis of turbulent fluid flow, combustion and conjugate heat transfer has been used to simulate thermal flow field in various metallurgical processes (Szajnar, Bartocha, Stawarz, Wróbel, & Sebzda, 2010; S. F. Zhang et al., 2009; Zhou, Yang, Reuter, & Boin, 2007) (See Fig. 1.7). Yang et al. (Yang et al., 2006) using the ANSYS Fluent software (ANSYS, 2016) performed CFD evaluation of various metallurgical applications including: melting of aluminum scrap in a rotary furnace, molten hot metal flow in a coke-bed blast furnace, electric arc furnace and gas-fired heat treating furnaces. They used $k-\varepsilon$ turbulence model alongside with the EDM combustion model. Several radiation models including, P-1, DTRM and Monte Carlo model (MCM) have been evaluated in different industrial furnaces. The capability of these approaches to predict the thermal interactions inside the furnace has been confirmed by the authors. They also presented several data, including temperature evolution, melting curves and gas consumption profiles proving the CFD applicability in predicting flow, temperature, mass fraction and reaction distribution. Wang et al. (J. Wang et al., 2008) predicted the temperature field of a gas quenching furnace using CFD simulation and Cosentino et al. (Cosentino, Warnken, Gebelin, & Reed, 2013) investigated the non-uniform quenching effect on the product properties.

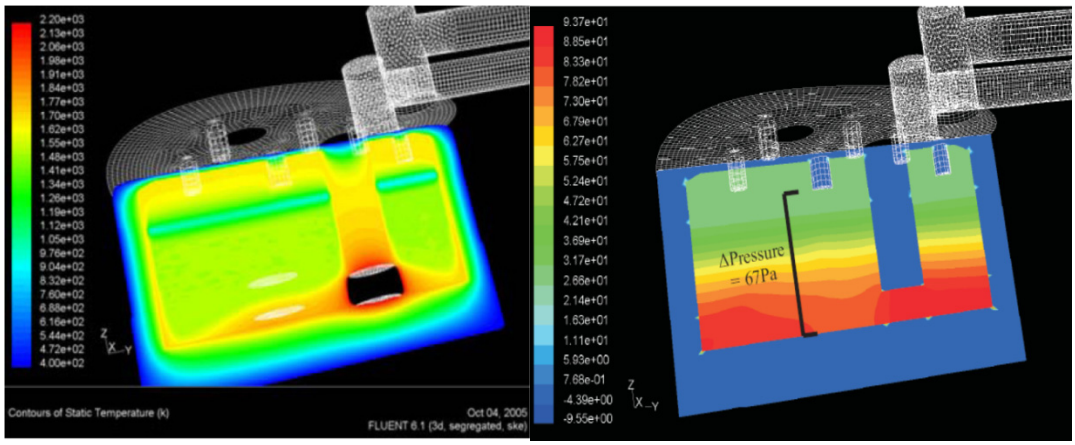

Figure 1.7 Right) pressure and left) temperature distribution prediction by CFD in the submerged arc furnace (Yang et al., 2006).

1.6.3 CFD Analysis of Heat Treatment Furnaces without Combustion

One of the most basic investigations of heat treatment process using CFD is the study of Elkatatny et al. (Elkatatny, Morsi, Blicblau, Das, & Doyle, 2003) who presented a CFD simulation of high-pressure gas quenching of H13 die in a vacuum heat treatment furnace (See Fig. 1.8). They suggested that a steady state simulation can be effectively used instead of complete transient simulation in order to reduce the computational cost. It has been reported that the CFD results were in good agreement with the experimental data and the steady state solution was capable of accurate prediction of quenching treatment.

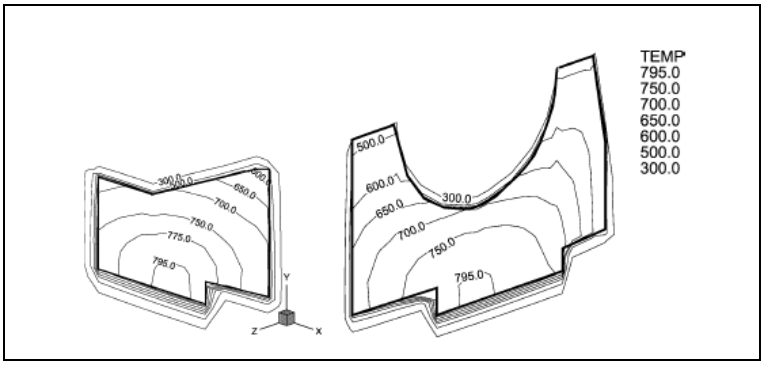

Figure 1.8 Temperature distribution prediction of H13 die using CFD simulation (Elkatatny et al., 2003).

Gongfa et al. (Gongfa et al., 2014) investigated the air quenching of heavy rail-head U71Mn in both internal and external fields product using CFD. They could establish the flow distribution, streamlines and temperature contours in internal and external fields. Using the cooling rate calculation, provided by CFD simulation, they reported phase transformation on the basis temperature gradient. Bergman (Bergman, 2012) provided a 2D simulation of a heat treatment furnace, including the gas fluid flow and heat transfer into the product (turbine structure). The significant impact of Reynolds number and buoyancy on the heat transfer rate was reported. Besides, in the case of turbulence modeling, according to the authors, $k-\omega$ model was proved to be a more reliable model in comparison to the standard $k-\varepsilon$ and the realizable $k-\varepsilon$ models to predict the heat flux for highly turbulent fluid flow. Wang et al. (J.

Wang, Chen, & Shan, 2006) employed CFD, validated by experimental data, in a gas nitriding furnace. Using the k-ε turbulence modeling in various fan motor velocities, fan locations and pressures, they reported fairly acceptable results in comparison to the experimental data.

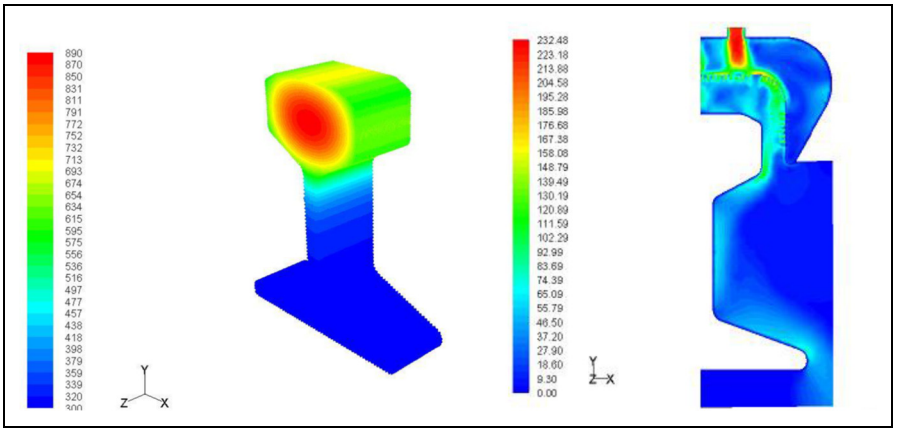

Figure 1.9 Right) temperature contour of air quenched rail head and left) flow field of quenching medium (Gongfa et al., 2014).

1.6.3.1 Loading Pattern and Residence Time Analyses

There is little data on the assessment of loading pattern concerning the uniformity of heat treatment process and simultaneous analysis of furnace-load interactions to improve the loading patterns inside the heat treatment furnaces. Among the rarely found data, Lior (Lior, 2004) presenting a comprehensive analysis of the gas quenching furnace fluid flow and the heat transfer discussed convective cooling over rectangular and circular bluff bodies with various flow characteristics and flow directions on the basis of thermo-chromic liquid crystal (R. Wiberg, 2001) and PIV measurement techniques (R. Wiberg & Lior, 2003). Besides, various positioning plans of the species with several configurations were discussed in this study. It should be noted that the configuration of bluff buddies positioning has been discussed widely in the fluid flow examinations; however, in the case of heat treating application, this study can be considered as one of the first efforts to evaluate the configuration impact on the uniformity of heat treatment (Lior, 2004). Wiberg in his experimental study (R. Wiberg & Lior, 2003) showed that separated flow over a bluff

cylinder in axial flow can lead to variations in the Nusselt number, or in other words convection heat transfer, up to 125%.

Mcchion's study (Macchion, 2005; Macchion, Lior, & Rizzi, 2004) is another investigation of charge influence on the gas quenching (heat treating) procedure. It has been concluded that the thermal flow field and temperature uniformity of the product are affected by chamber geometry, loads positioning configuration, their shapes and the gas mixture composition in the chamber. They stated that thermal field is significantly affected by the piece position. Products that had been placed in the central area of the furnace (with relatively equal distance to the furnace walls) experienced more uniform heat treatment. Besides, the large eddy simulation capability to simulate the gas quenching chamber has been evaluated in Macchion et al.'s numerical study (Macchion, Zahrai, & Bouwman, 2006).

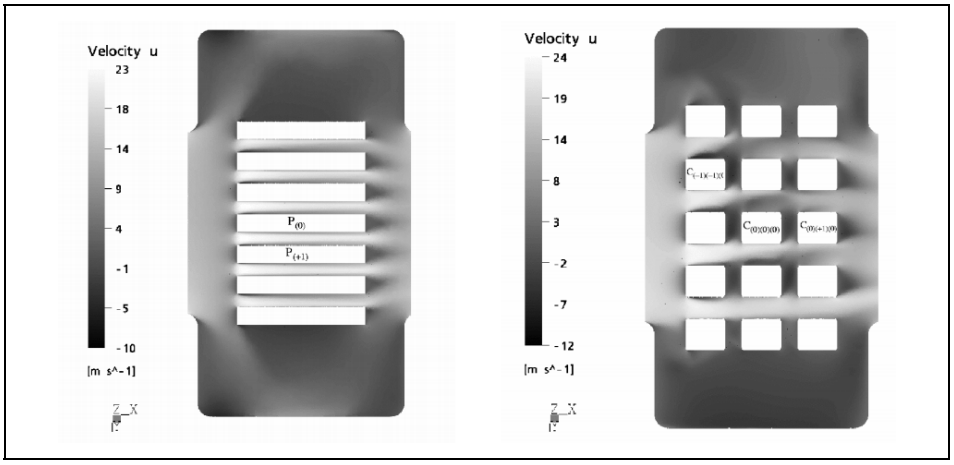

Figure 1.10 Streamwise velocity contours of a gas quenching chamber loaded by plates and rectangular ingots (Macchion et al., 2004).

Wang and Shang (Wang & Shang, 2010) investigated the flow and heat exchange in the high-pressure gas quenching chamber using the ANSYS Fluent software and evaluated their data on the basis of hot wire anemometer (for the velocity measurement in the gas quenching nozzles) and thermocouples measurements. They reported the flow circulation regime, including the streamlines of fluid circulation and temperature evolution on their case study. According to the author presence of a big eddy at the corner of the furnace where the cooling

rate was slower than other position was confirmed showing the importance of vortical structure in the present field of study. They also reported various cooling rates (with the approximately 7.9% relative error) in different zones of the chamber according to the location of products within the furnace.

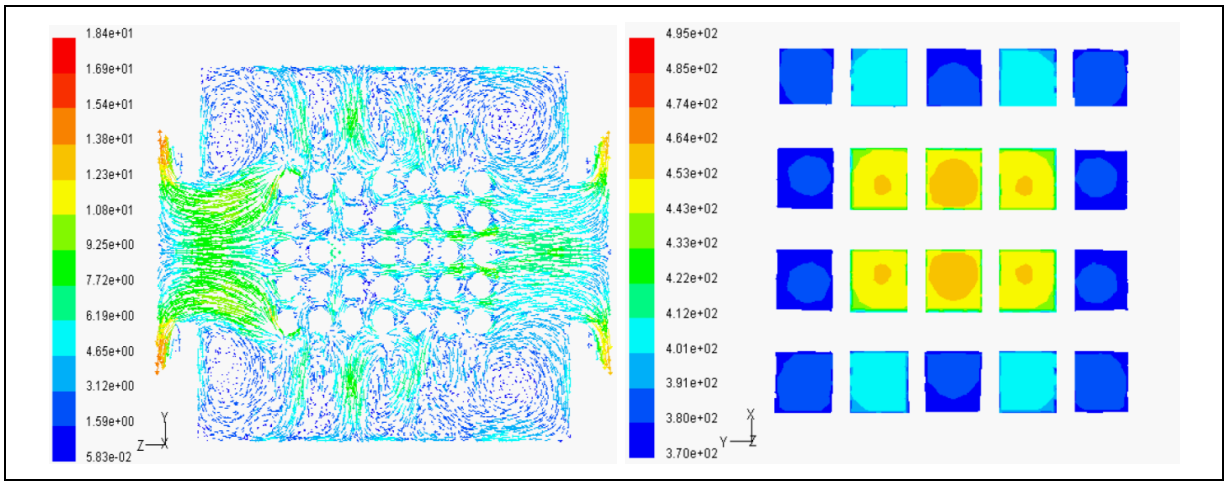

Figure 1.11 Left) velocity distribution and right) temperature in the gas quenching chamber (Z. J. Wang & Shang, 2010).

X. Hao et al (Hao et al., 2008) in their case study, which was a vacuum electrically heated furnace, using some simplification and optimization could propose a new heat treating time-table. Based on several heating rates for different locations of the product they used North American Die Casting Association (NADCA) suggestion to optimize the residence time of the block inside an electrically heated furnace. This suggestion states that heating stage can be started as soon as the temperature difference between surface and the center is less than 30°C (Hao et al., 2008).

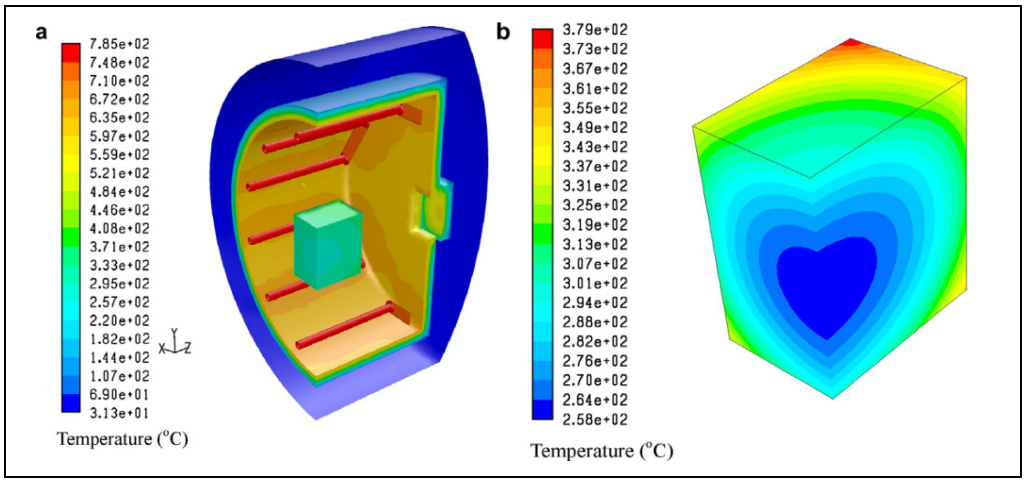

Figure 1.12 Contours of temperature evolution in the a) electricaly heated furnace and b) heat treated block (Hao et al., 2008).

In Fig. 1.13, T1, T2 and T3 represent the corner, surface and the core of the workpiece and TF is the furnace temperature. Heating curves and their mutual temperature differences between the locations show a considerable extra residence time in products initial schedule. As it can be seen in each heating stage t_b which is the optimized residence time is shorter than the t which had been used in their initial process. Their new proposed heat treating procedure, considering the new heating rates and some simplifications, decreased the residence time of the workpiece up to five hours. Although they just considered the temperature as the main criterion (without considering the material microstructural changes and mechanical properties based on various heating rates), their study proved the possible contributions for the residence time improvement in the steel making industry.

Kang and Rong (Kang & Rong, 2006) studied the effect of small products loading patterns on their heat treatment process within an electrically heated furnaces. Fig. 1.14 depicts the comparison of loading pattern influence on temperature evolution of samples in their numerical study. In this picture old and new are two different positioning plans and points 3 and 4 are two different locations of parts. As it can be seen there is a visible difference between the two methods of product positioning temperature evolution. This difference is more notable at low temperatures where the convection heat transfer is dominant. This study

and other similar analytical and numerical works demonstrate the importance of loading pattern optimization.

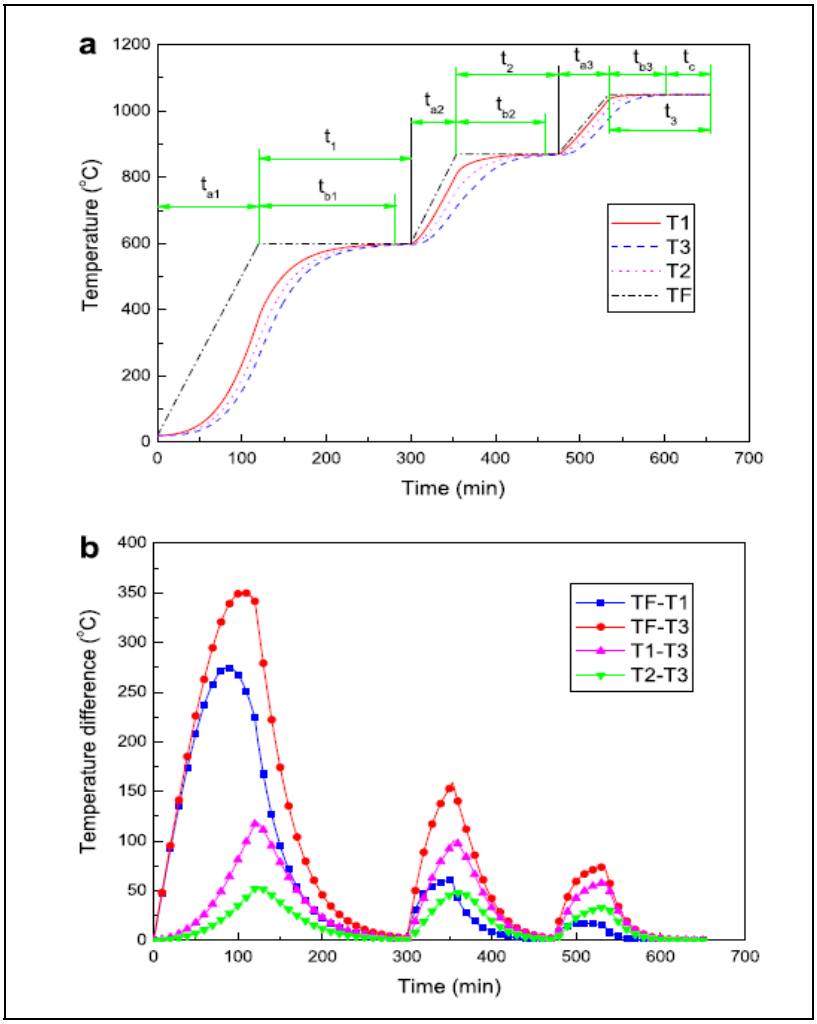

Figure 1.13 Optimization of furnace resicence time based on a) heating curves and b) temperature difference curves inside electretically heated furnace (Hao et al., 2008).

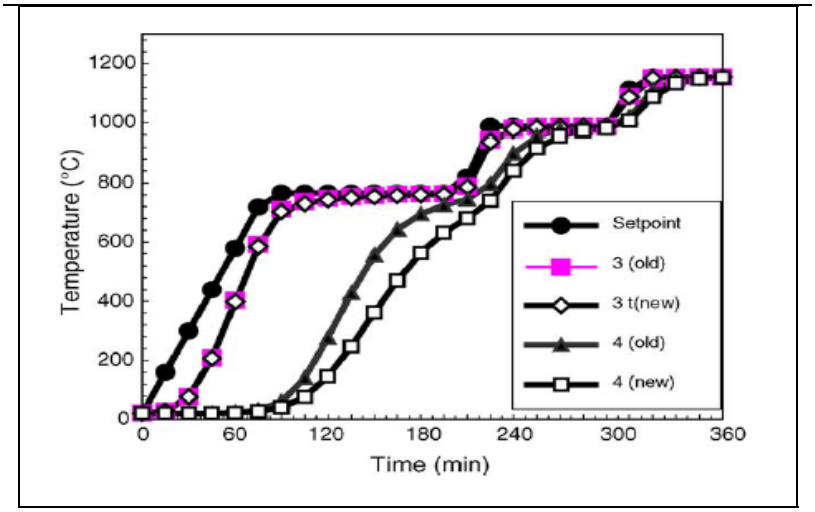

Figure 1.14 Comparison of two different products loading patteren effects on the heat treatment process inside an electercally heated furnace (Kang & Rong, 2006).

1.6.4 Gas-Fired Furnaces

Among the different types of industrial furnaces, gas-fired ones are commonly applied to applications with large size products (Totten, 2006). Natural gas combustion can be found in various furnaces including box and continuous ones such as pusher type and walking beam reheating furnaces (Totten, 2006). Simulation of these furnaces is more complex due to the existence of reactive flow combined with turbulent transport process and conjugate heat transfer including absorbing and emitting hot combustion products. Little data is available in the literature, probably due to above difficulties and the large volume of industrial furnaces and large size products, which requires significant computational and experimental resources. However, these challenges lately attracted researchers' attention to this field of study. Different gas-fired furnaces such as crucible or continues furnaces have been studied by several researchers (Govardhan, Rao, & Narasaiah, 2011; B. Wu et al., 2008; C. Zhang, Ishii, Hino, & Sugiyama, 2000).

Continuous reheating furnaces such as pusher type and walking beam furnaces, as gas-fired furnaces, have also been the subject of several investigations. For example, Harish and Dutta

(Harish & Dutta, 2005) concentrated on the radiation simulation of slab reheat furnace. Zhang et al. (Ishii, Zhang, & Hino, 2002) focused on the combustion modeling, provided insight into the temperature distribution and thermal interactions inside gas-fired furnaces. Recently, Liu et al. (Y. J. Liu, Li, Misra, Wang, & Wang, 2016) using CFD proposed a basic model for increasing the temperature uniformity in reheating furnaces. Mayr et al. (B Mayr, Prieler, Demuth, Potesser, & Hochenauer, 2017) proposed a one-step steady state CFD approach and Tang et al. (Tang et al., 2017) with a combination of 3D CFD and 2D finite difference methods (validated by experimental measurements) proposed time saving approaches for optimization purposes (See Fig. 1.15). However continuous gas-fired furnaces, due to their shorter processing time (regularly 2 hours (Tang et al., 2017)) in comparison with the large size heat treating furnaces (24-48 hours in the case of large size products (Gur & Pan, 2008)), require lower computational time for transient simulation. Besides, the relatively simple geometry of these furnaces, which allow for simplification such as steady state calculation in length or periodic transient simulation (B. Mayr, Prieler, Demuth, Moderer, et al., 2017) made these furnaces an interesting case study for several investigators. Employing models such as steady flame-let combustion model (SFM) (B. Mayr, Prieler, Demuth, Moderer, et al., 2017) and numerical techniques such as 2D interpolation (Tang et al., 2017) different methods have been proposed to reduce the computational cost. Recently Garcia et al. (García, Colorado, Obando, Arrieta, & Amell, 2019) investigated the effect of burner locations on the performance of walking-beam type reheating furnace using 3D steady state CFD calculation. According to the authors, burner types and positions have significant impact on the performance of the furnace and product quality.

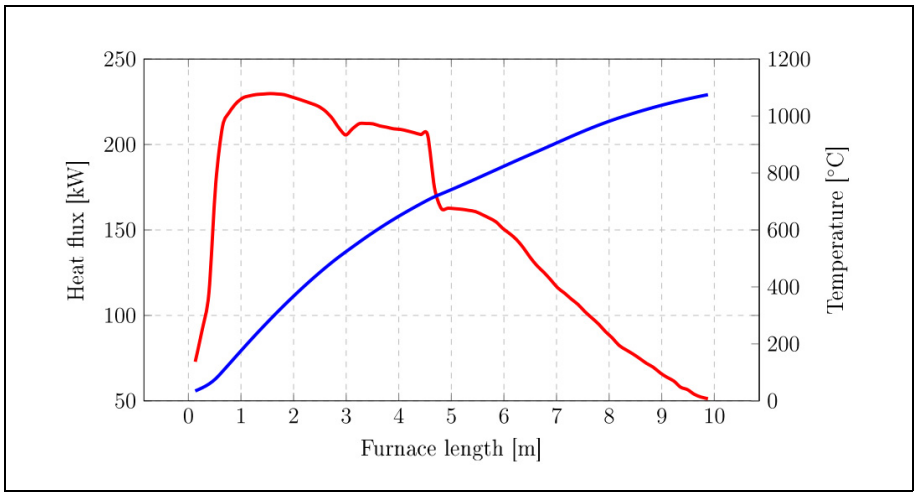

Figure 1.15 Volume average temperature of a billet and its averaged heat flux over the length of furnace (B. Mayr, Prieler, Demuth, Moderer, et al., 2017).

Gas-fired heat treatment furnaces on the other hand are usually subjected to longer operation times especially, in the case of large size products. This longer operation times need more attention in the instrumentation for the experimental measurements and also more computational cost for the complete transient simulation of the process. Besides, the entire furnace experiences completely transient phenomena in contrast to continuous furnaces with different zones with semi-steady-state situation. Hence, the number of published papers in the case of batch-type heat treatment furnaces is few and most of the limited numerical studies have been devoted to one aspect of the process (i.e., furnace chamber or only its details such as burners or product heating characteristics). For instance, Danon et al. (Danon et al., 2011) evaluated burner positioning effects on the performance of multi-burner combustion furnace and Galletti et al. (Galletti, Coraggio, & Tognotti, 2013) mainly focused on different combustion models for the burner simulation inside a semi-industrial furnace. Tu et al. (Tu et al., 2015) recently investigated the furnace room shape on the gas burner combustion. They used the standard $k-\varepsilon$ model for turbulence simulation and evaluated the applicability of EDC and EDM combustion models for various chamber configurations using experimental data to validate their simulations. Therefore, studies on simultaneous analysis of all the components of the furnace have been limited small-scale furnaces with simple geometrical details. Besides, on the experimental studies, measurements have been used

mostly as a validation tool rather than for analysis. For example, Yang et al. (Yang, De Jong, & Reuter, 2007) concentrating on the numerical simulation validated by experimental measurement, studied the performance of small-scale gas-fired mobile heat treatment furnaces. They studied several fuel supply systems and the influence of excess air on the performance of a heat treating mobile furnace. Transient temperature evolutions of products and furnace were discussed in their study (Fig. 1.6).

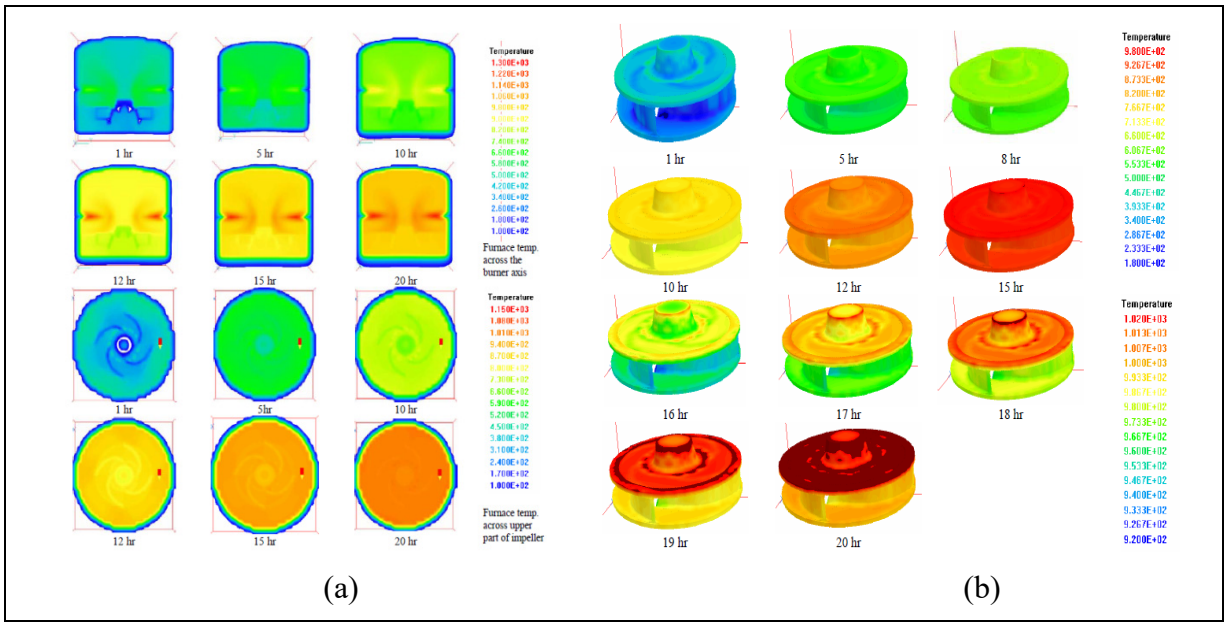

Figure 1.16 Temperature evolution of: a) the heat treating furnace and, b) the dredging impeller (Yang et al., 2007).

The CFD evaluation of oscillating combustion using the commercial code, ANSYS (ANSYS, 2016), in a crucible furnace is presented in Govardhan et al.'s (Govardhan et al., 2011) investigation. They employed standard $k-\varepsilon$ model, P-1 model and EDM for turbulence, radiation and combustion simulations, respectively. To validate the CFD results, temperature measurements in three probing points (T_1, T_2, and T_3) using type K thermocouples were made. Temperature predictions validation indicated that the CFD results were in good agreement with the experimentally measured temperatures. However, some inconsistencies specifically in case of oscillating combustion with the highly turbulent medium, was reported. According to the authors, the over-prediction of turbulence and radiation models,

inaccurate inlet boundary conditions and not sufficiently enough grid resolution were considered as inaccuracy sources.

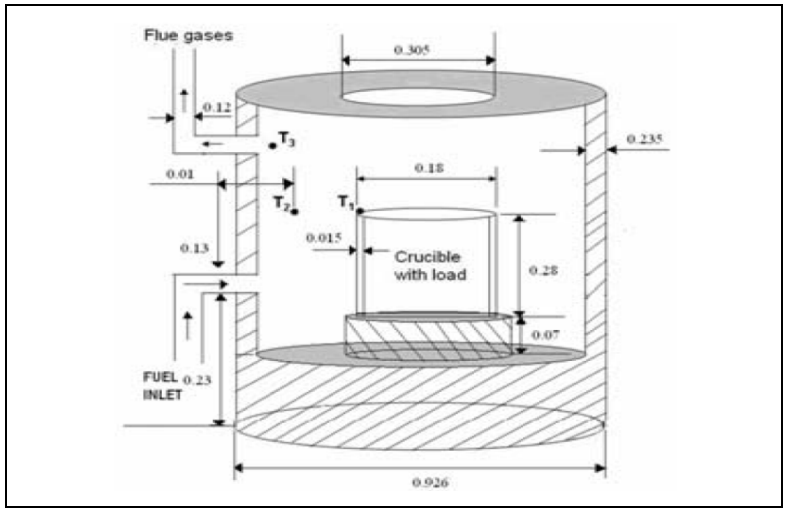

Figure 1.17 Schematic sketch of circular furnace employed by Govardhan et al. (Govardhan et al., 2011).

Table 1.1 Temperature validation reported by J. Govardhan et al. (Govardhan et al., 2011)

Time (min)	**T_1 (K)**		**T_2 (K)**		**T_3 (K)**	
	Exp	CFD	Exp	CFD	Exp	CFD
10	575	594	621	871	735	871
20	778	843	791	1040	1043	1080
30	921	912	977	1150	1051	1150
40	974	938	1053	1170	1123	1222

In another work, Mayr et al. (Bernhard Mayr, Prieler, Demuth, Potesser, & Hochenauer, 2015) employing experimental validation evaluated the applicability of steady state CFD simulation for combustion modeling of flat burners, using steady laminar flame let model (SFM), in a lab-scale heat treatment furnace; and reported on the performance of the furnace as a function of fuel/oxidizer ratio.

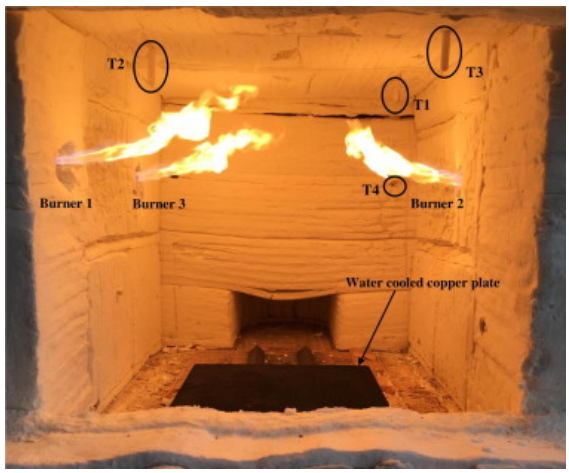

Figure 1.18 The lab-scale gas-fired furnace studied by Mayr et al. (Mayr et al., 2015).

Mayr et al. (B Mayr, Prieler, Demuth, Potesser, et al., 2017) recently presented a steady state computational analysis of semi-industrial gas-fired furnace validated by experimental measurements.

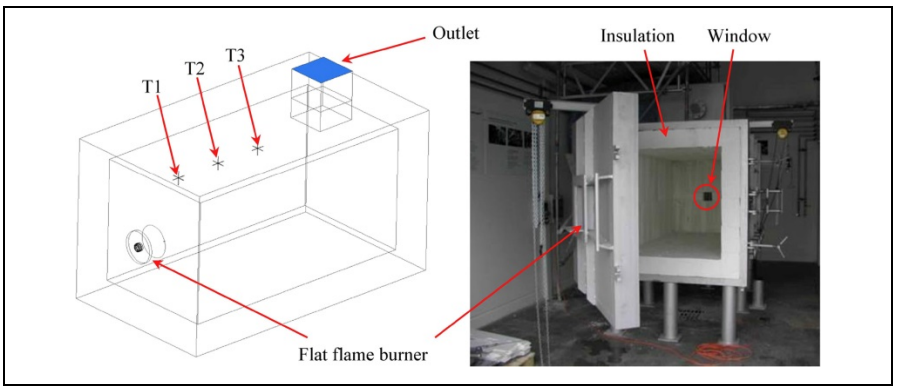

Figure 1.19 Semi industrial gas-fired furnace and its relative measurement points used in Mayr et al. numerical study (Mayr, Prieler, Demuth, Potesser, & Hochenauer, 2017).

The main goal was the determination of reliable combustion models with lower computational demand for future optimization purposes. Detail analysis of the combustion phenomena in different fuel/gas ratios and the subsequent heat transfer to the surface of the quarrel is presented in their paper. Temperature measurement at some points in the furnace

and at the surface of the quarrel was used to validate the numerical simulations. Authors proposed an efficient model, from the computational cost point of view, for further optimization. According to the authors, the predicted temperature of the furnace wall showed a considerable deviation from the measurements but also showed a good level of accuracy. The high over prediction of model in one of the fuel/gas ratio case studies (Fig. 1. 20 (c)) was accounted for the instabilities occurred during the experimental measurements.

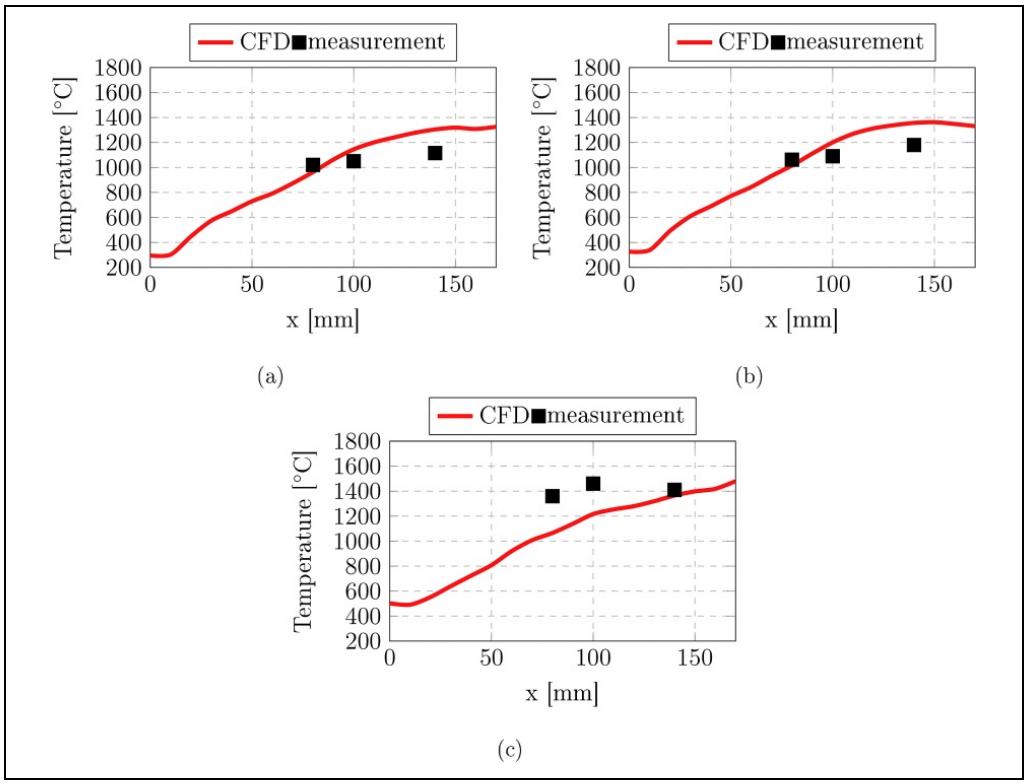

Figure 1.20 Comparison between CFD results and experimental measurements in a semi-industrial size gas-fired furnace (Mayr, Prieler, Demuth, Potesser, et al., 2017).

1.7 Challenges and Objectives

The literature review provided a large number of studies on different approaches used for developing accurate heat treatment processes using experimental and/or numerical investigations. However, among works concerning the simulation of gas-fired furnaces, only small-scale furnaces or those with a shorter operation time have been mainly considered.

Data on simultaneous analyses of thermal interactions inside industrial heat treatment furnaces along with large size products heating characteristics are very rare. The majority of the studies covered one part of the process, i.e. heating chamber and its details such as burners, or products heating characteristic solely. Moreover, experimental measurements due to technical challenges have been generally devoted to validating numerical results rather than being used as tools to heat transfer analysis. Detail experimental analysis, especially for the large size products, that encompasses high temperature gradient in their different locations is in demand considering the state of literature. Thus, the first objective of the present study is to comprehensively analyze the heat transfer in the heat treatment process of large size ingots in full scale gas-fired furnaces using both experimental measurements and CFD simulations. This part of the present thesis is aimed to address several missing links to the scientific as well as industrial communities. Temperature uniformity of the large size parts as a crucial parameter to evaluate the process efficiency was chosen to analyze the transient history of large size forged ingots within an industrial gas-fired furnace. Experimental measurement results and unsteady CFD predictions were used to analyze the temperature evolution of a large size forged ingot in a single loading configuration during the heat treatment process based on heat transfer modes in the furnace, fluid flow circulation, and vortical structures.

Optimization of furnace residence time inside heat treatment furnaces can significantly affect the production cost and fuel usage in the steel industry. On the other hand, this optimization along with loading pattern improvement of steel parts in heat treatment furnaces can guarantee the uniformity of heat treatment and consequently final products' quality. Residence time and loading pattern improvement were rarely addressed in the literature. Among the few reported works, electrical furnaces and small products' loading patterns were only discussed. Therefore the second objective of the study is to carry out a thermal analysis on furnace residence time and loading pattern of large size forgings inside gas-fired heat treatment furnaces. Specifically, quantification of temperature non-uniformity in a non-optimized loading pattern and possible improvement using skids and spacers were the secondary objectives of this part. A novel hybrid experimental-numerical approach is

proposed to improve the residence time of large size steel parts inside gas-fired heat treatment furnace.

Different numerical and experimental studies on the heat treatment process inside industrial and laboratory scale furnaces were discussed in the presented literature review. However, these studies were performed with different research purposes, like product temperature prediction, combustion simulation, non-uniformity identification and loading pattern or residence time optimization. This makes it difficult to evaluate the strength and limitations of numerical approaches in CFD simulations for the prediction of thermal interactions like turbulent convection or combustion within the gas-fired furnace. However, little data is available on the systematic investigation of CFD results sensitivity to the numerical approaches used in the modeling of gas-fired batch heat treatment furnaces. Therefore, the third main objective of the present study is to assess the sensitivity of CFD predictions to employed numerical techniques in order to have reliable and cost effective simulations of the heat treatment process inside large size heat treatment furnaces. To this end, several turbulence models as well as combustion modeling approaches were examined both for the flow field and scalar predictions (temperature) near the burner and steel parts.

CHAPTER 2

NUMERICAL DETAILS FOR THERMAL ANALYSIS OF HEAT TREATMENT PROCESS IN GAS-FIRED FURNACE

2.1 Introduction

In the present chapter, the principal elements of the numerical approaches that will be considered in the thesis will be presented. Specifically, the numerical models for radiation, combustion, and turbulence modeling that will be assessed in the present study will be introduced. An overall comparison of models for each phenomenon will be presented from both computational cost and accuracy points of view.

2.2 Computational Fluid Dynamics (CFD)

Computational fluid dynamics (CFD) is a branch of mechanical engineering widely used in various fluid dynamics and heat transfer phenomena. It has attracted many scientific disciplines when dealing with the complicated applications where the conventional experimental techniques are difficult to execute or expensive. Although CFD fundamentally requires reliable experimental data to validate its predictions with, it can provide valuable insight into the nature of fluid dynamics and the phenomena that the available experimental facilities cannot capture. Typically a CFD code or software such as ANSYS FLUENT (ANSYS, 2016) contains four main components (Ashgriz & Mostaghimi, 2002):

- Partial differential equations which are discretized to supply a numerical set of equations that identify and describe the fluid flow, heat transfer, combustion or any other flow related interactions.
- Grid generators that divide the flow domain into small grids or control volumes where the equations are solved.
- Initial and boundary conditions describing the flow pattern that should be defined by the user to obtain the reliable data. This part of CFD code is extremely dependent on experimental data.

- Procedures that control the accuracy, and convergence of the solution.

Due to the wide range of CFD approaches and formulations, in the following sections the most important numerical details that take part in the present project will be discussed. The topics are selected based on the project demands and the literature review presented in the previous chapter.

2.3 Navier-Stokes Equations

The most important set of equations to predict, describe and simulate the fluid flow, the Navier-Stokes equations provide mathematical foundations of fluid flow, heat transfer, mass transfer and any other fluid related phenomena. Basically, for an accurate and exact prediction and description of all flows, the mass and momentum equations called as, continuity and momentum equations should be solved. For the flows that deal with the heat transfer or compressibility an additional equation, energy equation, should be considered. If the target flow encompasses mixing of the species, the species conservation equation should also be solved. Moreover, in the case of reacting flow model, the conservation equation for the mixture reaction should be added. Finally in the case of turbulent flow, other additional transport equations must be solved to consider the impact of turbulence on the fluid flow field (Constantin & Foias, 1988; Patankar, 2018).

- Conservation of mass:

In general, for both compressible and incompressible fluid flows, the conservation of mass equation called also continuity equation is given by (Patankar, 2018):

$$\frac{\partial \rho}{\partial t} + \nabla.(\rho \mathrm{v}) = S_m \tag{2.1}$$

The definition of all the variables and related units are provided in the nomenclature page.

- Conservation of Momentum

Momentum equation, states that the algebraic summation of all the active forces on a control volume should be equal to zero. The differential form of momentum equation is (Patankar, 2018):

$$\frac{\partial(\rho v)}{\partial t}+\nabla.(\rho \mathrm{v} v)=-\nabla \mathrm{p}+\nabla.(\tau)+\rho g+F \tag{2.2}$$

The stress tensor, τ, is defined as:

$$\tau=\mu\left[\left(\nabla v+\nabla v^{T}\right)-\frac{2}{3}\nabla.vI\right] \tag{2.3}$$

- Energy Equation

The general differential energy equation or energy conservation equation is:

$$\frac{\partial}{\partial t}(\rho E)+\nabla.(\mathrm{v}(\rho E+p))=\nabla.\left(k_{eff}\nabla \mathrm{T}-\sum_{j}h_{j}J_{j}+\left(\tau_{eff}.v\right)\right)+S_{h} \tag{2.4}$$

In this equation k_{eff} is the effective conductivity (summation of molecular and turbulent conductivities), J_j is the diffusion flux of species j, and τ_{eff} is the effective stress tensor. Turbulent thermal conductivity which can be determined using turbulence model should be considered in case of turbulent flow. The first term of the right-hand side of Eq. 2.4 represents the conduction energy transformation in the fluid while the second and third ones indicate the energy transfer caused by species diffusion and viscous dissipation, respectively (Tennekes et al., 1972). Finally, the term S_h represents the chemical reaction heat and any other volumetric heat sources such as radiation sources. In the above equation, the relationship between the energy, *E*, and the sensible enthalpy, *h*, is (Incropera et al., 2007):

$$E=h-\frac{p}{\rho}+\frac{v^{2}}{2} \tag{2.5}$$

Where for an ideal fluid on the basis of mass fraction of species j, Y_j:

$$h=\sum_{j}Y_{j}h_{j} \tag{2.6}$$

- Solid Regions Energy Equation

The energy transport in the solid medium is described by the following equation (Incropera et al., 2007):

$$\frac{\partial}{\partial t}(\rho h)+\nabla.(v\rho h)=\nabla.(k\nabla T)+S_h \tag{2.7}$$

The above equation terms are energy storage's change with time, the energy convection transfer due to motion in rotation or movement of solid, (the term v, is calculated from the specific movement in the solid zone), conduction heat fluxes (first term in the right hand side of the equation) and the volumetric heat sources in the solid medium, respectively.

2.4 Species Transport

To solve and model the mixing reactions such as combustion in the burners and the transport of combustion products inside the furnace the conservation equation of species that includes convection, diffusion and reaction source, should be considered for each component (Bennett, 1962; Incropera et al., 2007). In the case of heat treatment, the species transport with reaction is the objective approach. The species transport formulation for the local mass fraction species of, Y_i, for the i_{th} species is (B. Magnussen, 1981):

$$\frac{\partial}{\partial t}(\rho Y_i)+\nabla.(\rho\bar{v}Y_i)=-\nabla.\overline{J}_i+R_i+S_i \tag{2.8}$$

In which R_i is the net rate of the production of i_{th} component by chemical reaction and S_i encompasses the other types of sources. The term $\overline{J}_i$ is the diffusion flux of species i, which depends on the gradient of concentration and temperature. For the turbulent regime the mass diffusion can be computed as follows:

$$\overline{J}_i=-\left[\rho D_{i,m}+\frac{\mu_t}{Sc_t}\right]\nabla Y_i-D_{T,i}\frac{\nabla T}{T} \tag{2.9}$$

where Sc_t, μ_t, and D_t are the turbulence Schmidt number, turbulence viscosity and the turbulent diffusivity, respectively. To achieve the exact simulation of mass transfer or species transport equation, all the terms and their modeling approaches should be considered and evaluated alongside with the geometry. However, the most important term and the key parameter to start the mass transfer solution is the reaction modeling. To determine the reaction rates in equation (2.8) the three well-known approaches are:

- Laminar Finite-rate model

- Eddy-dissipation model
- Eddy-dissipation-concept (EDC)

In the first model, the effect of turbulent fluctuations is neglected in the laminar finite-rate approach and the reaction rates are specified by Arrhenius kinetic expression. While, in the eddy-dissipation approach, the reaction rates are assumed to be dominated by turbulence and the computationally expensive Arrhenius chemical kinetic calculations are ignored. The third model includes the detailed Arrhenius chemical kinetics in turbulent flames which means high computational cost. Since, the eddy-dissipation model has been used in similar studies; therefore, this technique will be presented in detail in the next section. Non-premix combustion model with equilibrium model will also be illustrated as the model with lower computational cost which will be employed in the present study.

2.4.1 The Eddy-Dissipation Model

As it is mentioned the most important term and the key parameter to start the mass transfer solution is the reaction modeling. In the eddy-dissipation model, based on the Magunssen and Hjertager study (B. Magnussen, 1981), the net rate of production of i_{th} species in the reaction r, $R_{i,r}$ can be calculated as below:

$$R_{i,r} = v'_{i,r} M_{w,i} P \rho \frac{\varepsilon}{k} \min_R \left[\frac{Y_R}{v'_{R,r} M_{w,R}} \right] \tag{2.10}$$

$$R_{i,r} = v'_{i,r} M_{w,i} P Q \rho \frac{\varepsilon}{k} \left[\frac{\sum_p Y_p}{\sum_j^N v''_{j,r} M_{w,j}} \right] \tag{2.11}$$

where Y_P is the mass fraction of any product species, Y_R is the mass fraction of the particular reactant, and P and Q are empirical constants equal to 4.0 and 0.5, respectively. As it can be seen in these equations the reaction rate is calculated on the basis of eddy mixing scale, ε/k, and the eddy-break up of Spalding (Spalding, 1971).

2.4.2 Non-premixed Combustion

The basic assumption of this combustion modeling is that the thermochemistry of combustion can be reduced to a local mass mixture fraction of burnt and unburnt fuel stream elements (Poinsot & Veynante, 2005). Using this method, the combustion is simplified to a mixing problem. In other words, this modeling approach includes transport equation solution for one or two mixture fraction scalars. The mixture fraction, f, to which the instantaneous thermochemical state of the fluid is dependent on, can be determined as a function of mass fraction for element i, M_i as follow (Ishii et al., 2002):

$$f = \frac{M_i - M_{i,ox}}{M_{i,fuel} - M_{i,ox}} \tag{2.12}$$

The term f can be used to calculate the instantaneous values of density, temperature and enthalpy of any mixture components:

$$\phi_i = \phi_i(f) \tag{2.13}$$

In case of second stream presence, the sum of all three mixture fractions in the system is always equal to 1:

$$f_{fuel} + f_{\sec} + f_{ox} = 1 \tag{2.14}$$

If the diffusion coefficients for all reactant species are equal, the species equations can be simplified to one equation written for the mixture fraction. This assumption is acceptable, especially for turbulent flow. The transport equation for density averaged application goes as follows (Poinsot & Veynante, 2005):

$$\frac{\partial}{\partial t}(\rho\overline{f}) + \nabla.(\rho\overset{\mathrm{r}}{v}\overline{f}) = \nabla.\left[\frac{\mu_l + \mu_t}{\sigma_t}\nabla\overline{f}\right] + S_s \tag{2.15}$$

Where μ_l, μ_t and S_s are the laminar viscosity, the turbulent viscosity and the source terms, respectively. Besides, the mixture fraction variance ($\overline{f'^2} = f - \overline{f}$) equation should be solved to predict the exact non-premixed combustion (Poinsot & Veynante, 2005):

$$\frac{\partial}{\partial t}(\rho\overline{f'^2}) + \nabla.(\rho\overset{\mathrm{r}}{v}\overline{f'^2}) = \nabla.\left[\frac{\mu_l + \mu_t}{\sigma_t}\nabla\overline{f'^2}\right] + C_g\mu_l.(\nabla\overline{f})^2 - C_d\rho\frac{\varepsilon}{k}\overline{f'^2} + S \tag{2.16}$$

In many industrial applications, the combustion does not occur under chemical equilibrium. According to the reports in the literature (Bowman, 1991; Sivathanu & Faeth, 1990) for lean combustion, as the present work's case study where the 5% excess air was inputted to the burners, thermodynamic equilibrium could be used to describe the process. Therefore, equilibrium chemistry with Rich Flammability Limit (RFL) (ANSYS, 2016) should be used to accommodate chemical non-equilibrium for the combustion simulation. A β shape probability density function (PDF) of turbulence-chemistry interactions is used in the software to relate instantaneous values to the averaged mixture fractions (ANSYS, 2016). It should be pointed out that the non-premix combustion with equilibrium model requires these conditions to be fulfilled:

- Turbulent flow field
- A diffusion chemical system that encompasses the discrete fuel and oxidizer entrances.
- The equal diffusion coefficient for all species (in other words Lewis number in the flow field, must be unity), which is a good assumption in turbulent combustion
- The same type of fuel composition in multi-inlet applications.

In the present study, the applicability of non-premix combustion along with the EDM model will be evaluated.

2.5 Radiation

In the heat treatment process, where the radiant heat flux due to the high temperature of the heat treatment furnace, is one of the most important mode of heat transfer; the radiation modeling has a great impact on the final simulation result. The equation of radiation considering absorption, emission and scattering is as follows (Howell et al., 2015):

$$\frac{dI(\vec{r},\vec{s})}{ds}+(a+\sigma_s)I(\vec{r},\vec{s})=an^2\frac{\sigma T^4}{\pi}+\frac{\sigma_s}{4\pi}\int_0^{4\pi} I(\vec{r},\vec{s})\phi(\vec{s},\vec{s}')d\Omega' \tag{2.17}$$

Where $\vec{r}$, $\vec{s}$, $\vec{s}'$ and s are position vector, direction vector, scattering direction vector and path length respectively. Besides, a, n, σ_s and σ denote the absorption coefficient, refractive index, scattering coefficient and Stefan-Boltzmann constant, respectively. The terms *I, T* and

ϕ refer to radiation intensity, local temperature and phase function. The term $(a+\sigma_s)$ represents the optical thickness capacity of the medium, which is calculated on the basis of the medium gas mixture and the operating conditions.

2.5.1 P-1 Radiation Model

This model belongs to the general P-N model which is based on the expansion of the radiation intensity, I , into an orthogonal series of spherical harmonics (Howell et al., 2015). For the P-1 radiation equation the radiation flux can be expressed as follows (Howell et al., 2015):

$$-\nabla.q_r = aG - 4an^2\sigma T^4 \tag{2.18}$$

Where q_r and G are the radiation flux and incident radiation; and the expression $-\nabla.q_r$ is the heat source term. Although the above equation can be modified in the case of non-gray radiation applications, the non-gray model assumes a constant absorption coefficient for wavelength and constant spectral emissivity at walls. The P-1 model solves equation (2.17) as a diffusion equation which means that this model needs a lower amount of CPU usage. Besides, it considers also scattering and provides results with a good prediction for the combustion applications. The P-1 model specifically provides reliable results for the cases where the optical thickness $((a+\sigma)\times L)$ is larger than unity. Optical thickness parameter encompasses the simultaneous effect of absorption, scattering and size of the domain. The other advantage of this model is its compatibility with complex geometry and curve line coordinates (Sazhin, Sazhina, Faltsi-Saravelou, & Wild, 1996). Although this low computational cost can be considered as an advantage for the P-1 model, inaccuracies are unavoidable due to the fact that this model assumes all the surfaces as a diffusive one, or in other words it assumes the isotropic reflection of incident radiation at the surfaces (Howell et al., 2015).

2.5.2 Discrete Ordinates Radiation Model (DO)

The DO radiation model (Chui & Raithby, 1993) modifies equation (2.17) to a transport equation of radiation intensity by solving the equation for finite numbers of discrete solid angles. This solution method is similar to the fluid flow equation's solution. In the DO coupled energy and intensity equations are solved simultaneously in each control volume. This model considers the radiation equation in the direction $\vec{s}$ as a field equation and for the spectral intensity $I_\lambda(\vec{r},\vec{s})$ using a gray-band model:

$$\nabla.(I_\lambda(\vec{r},\vec{s})\vec{s}) + (a_\lambda + \sigma_s)I(\vec{r},\vec{s}) = a_\lambda n^2 I_{b\lambda} + \frac{\sigma_s}{4\pi}\int_0^{4\pi} I_\lambda(\vec{r},\vec{s}')\phi(\vec{s},\vec{s}')d\Omega' \tag{2.19}$$

Where λ, a_λ and $I_{b\lambda}$ is the wavelength, spectral absorption and black body intensity, respectively. This model divides the radiation spectrum to *m* wavelengths band and integrates the above equation over each interval. This integration results in transport equations for the quantity $I_\lambda \Delta_\lambda$. Therefore, total intensity in each direction and position will be:

$$I(\vec{r},\vec{s}) = \sum_k I_{\lambda k}(\vec{r},\vec{s})\Delta\lambda_k \tag{2.20}$$

2.5.3 Surface to Surface (S2S) Model

In this model, the radiation heat transfer between two surfaces is a direct function of the radiation view factor, also called the shape factor. This model which requires lower computational costs in comparison with the DO model, ignores absorption, emission or scattering effect of radiation by the medium. Therefore, the radiation energy balance is calculated, as follows (Howell et al., 2015):

$$q_{out,k} = \varepsilon_k \sigma T_k^4 + \rho_k \sum_{j=1}^{N} F_{kj} q_{out,j} \tag{2.21}$$

In this equation, F_{kj} is the radiation view factor between surface *k* and surface *j* which is calculated based on the size, separation distance and orientation of the surfaces.

2.6 Turbulence

Studies on turbulence can be divided into analytical solutions, experimental investigations and numerical simulations. As a result of the highly nonlinear nature of turbulence, including, analytical solutions are limited to very fundamental and simple applications such as flow over a flat plate, etc. (Davidson, 2011). On the other hand, experimental investigations have a significant role not only on the released information about various applications, but also on the data production for numerical simulations. Although, high-tech measurement techniques and facilities support the experimental investigations, the cost of measurement in experimental trials and also the limitation of measurement in these applications such as steel heat treatment highlight the role of numerical simulation in turbulence determination. Development of the computational equipment over the last 20 years has led to wide employment of CFD for the simulation of turbulence problems from simple applications to highly turbulent flow fields such as combustor simulations, turbine blade film cooling and heat treatment industries (Bazdidi-Tehrani, Bohlooli, & Jadidi, 2015). There are different approaches to solve the turbulent nature of fluid flows. The most well-known and common methodology in turbulence area is the Reynolds Averaged Navier-Stokes (RANS) models which are highly compatible with different phenomena, complex geometries and different grid resolutions. Based on the literature review and the research scope these models have been selected for the present study and discussed briefly in the next sections.

2.6.1 Reynolds Averaged Navier-Stokes (RANS)

In the RANS based models the variables are usually decomposed into mean (time-averaged) and fluctuating parts. The mean values can be achieved by Reynolds averaging (including the time averaging, volume averaging and ensemble averaging) that has been introduced by Reynolds in 1895. Time averaging which is the most common Reynolds averaging method can be used when the turbulent flow has a steady or stationary nature which means that the

flow parameters do not vary in time average. The time averaging can be defined as (Bazdidi-Tehrani, Hatami, & Abouata, 2017):

$$F(\bar{r}) = \lim_{T\to\infty}\left[\frac{1}{T}\int_{t}^{t+T} f(\bar{r},t)dt\right] \tag{2.22}$$

Using this formula, the parameters can be written as follows:

$$\begin{aligned} u &= U + u' \\ p &= P + p' \\ T &= T + T' \end{aligned} \tag{2.23}$$

Where u, p, and T are the instantaneous velocity, pressure and temperature, respectively. The terms U, P, and T (also can be written as U, P and T) represent the time-averaged parts while the terms u', p', and T' are the fluctuating parts of velocity, temperature and pressure, respectively. In should be noted that according to the continuity equation:

$$\begin{aligned} \frac{\partial U_i}{\partial x_i} &= 0 \\ \frac{\partial u_i}{\partial x_i} &= 0 \end{aligned} \tag{2.24}$$

By imposing this decomposition to the Navier-Stokes equations, we have (Davidson, 2011):

$$\frac{\partial \rho}{\partial t} + \frac{\partial}{\partial x_i}(\rho U_i) = 0 \tag{2.25}$$

$$\frac{D(\rho U_i)}{Dt} = -\frac{\partial P}{\partial x_i} + \frac{\partial}{\partial x_j}\left(2\mu S_{ij} - \overline{u_i' u_j'}\right) \tag{2.26}$$

$$\frac{DT}{Dt} = \frac{\partial}{\partial x_i}\left(\alpha \frac{\partial T}{\partial x_i} - \overline{u_i' T'}\right) \tag{2.27}$$

Where:

$$S_{ij} = \frac{1}{2}\left(\frac{\partial U_i}{\partial x_j} + \frac{\partial U_j}{\partial x_i}\right) \tag{2.28}$$

The Eq. (1.8) also can be written as follows:

$$U_i \frac{\partial U_i}{\partial x_j} = -\frac{1}{\rho}\frac{\partial P}{\partial x_i} + \frac{1}{\rho}\frac{\partial}{\partial x_j}\left(\tau_{ij} - \rho\overline{u_i' u_j'}\right) + F_i \tag{2.29}$$

As it can be seen the difference between the fundamental Eq. (2.2) and the time-averaged Eq. (2.29) is the term $\rho\overline{u_i'u_j'}$ which is called Reynolds stress because it has the dimensions of stress (Davidson, 2011). This term describes the effect of turbulent diffusion of momentum which is stronger than the molecular viscosity in a fully turbulent flow. To close the set of equations the Reynolds stress term should be modelled. One of the basic approaches is Boussinesq hypothesis, called as constant eddy viscosity, which provides a relation between the $\rho\overline{u_i'u_j'}$ and the average velocity gradient, as follows (Schiestel, 1983):

$$-\rho\overline{u_i'u_j'} = \mu_t\left(\frac{\partial U_i}{\partial x_j}+\frac{\partial U_j}{\partial x_i}\right)-\frac{2}{3}\left(\rho k+\mu_t\frac{\partial U_i}{\partial x_i}\right)\delta_{ij} \tag{2.30}$$

Where *k* or turbulence kinetic energy is given by:

$$k=\frac{1}{2}\left(\overline{u'^2}+\overline{v'^2}+\overline{w'^2}\right) \tag{2.31}$$

There are several turbulence models for the description of $\overline{u_i'u_j'}$, that have various degrees of complexity on the basis of extra partial differential (or transport) equations that must be solved in addition to the three conservation equations. These models can be found from the simplest algebraic or zero-equation model to the full Reynolds stress model (FRSM) and nonlinear eddy viscosity models (Bazdidi-Tehrani, Mohammadi-Ahmar, Kiamansouri, & Jadidi, 2015).

2.6.2 Two-Equation Turbulence models

Generally, the two-equation turbulence models employ the definition of the turbulence viscosity as a function of velocity scale (V_s) and length scale (l_s) (Davidson, 2011).

$$\mu_t=\rho C_\mu V_s l_s \tag{2.32}$$

Where, the velocity scale is usually equal to $k^{1/2}$ (or root mean square of turbulence kinetic energy). On the other hand, the specification of length scale is different in various models which in turn, provide several choices. For instance, the well-known $k-\varepsilon$ (Launder & Spalding, 1972) turbulence model assumes that the length scale is proportional to the $k^{3/2}/\varepsilon$,

where ε is the turbulence dissipation rate. While, the k-ω model (Wilcox, 1998) uses the $k^{1/2}/\omega$.

2.6.2.1 $k-\varepsilon$ Turbulence Model

The turbulence kinetic energy (k) and the turbulence dissipation rate (ε) equations are the two additional transport equations that the standard $k-\varepsilon$ model employs to close the Reynolds averaged Navire-stokes equations (Davidson, 2011).

$$\frac{\partial}{\partial t}(\rho k)+\frac{\partial}{\partial x_i}(\rho k u_i)=\frac{\partial}{\partial x_j}\left[\left(\mu+\frac{\mu_t}{\sigma_k}\right)\frac{\partial k}{\partial x_j}\right]+G_k+G_b-\rho\varepsilon-Y_M+S_k \tag{2.33}$$

$$\frac{\partial}{\partial t}(\rho\varepsilon)+\frac{\partial}{\partial x_i}(\rho\varepsilon u_i)=\frac{\partial}{\partial x_j}\left[\left(\mu+\frac{\mu_t}{\sigma_\varepsilon}\right)\frac{\partial \varepsilon}{\partial x_j}\right]+C_{1\varepsilon}\frac{\varepsilon}{k}(G_k+C_{3\varepsilon}G_b)-C_{2\varepsilon}\rho\frac{\varepsilon^2}{k}+S_\varepsilon \tag{2.34}$$

Where G_k and G_b are the turbulence kinetic energy generations due to the velocity gradients and buoyancies. Y_M and S represent the compressibility effect and the other source terms, respectively. The ANSYS FLUENT (ANSYS, 2016) Commercial code uses the following values for the constants in the above equations:

Table 2.1 The values of the $k-\varepsilon$ model constants (ANSYS, 2016).

C_μ	$C_{1\varepsilon}$	$C_{2\varepsilon}$	σ_k	σ_ε
0.09	1.44	1.92	1	1.3

These values have been determined on the basis of various numerical simulations. However, for special cases there are some corrections to these values such as those reported by Crasto et al. (Crasto, 2007) for the atmospheric boundary layer applications. It should be noted that the other branch of $k-\varepsilon$ models such as realizable and RNG $k-\varepsilon$, were introduced on the basis of the standard model and were employed in various applications such as heat treatment furnaces (Bernhard Mayr et al., 2015). The major difference for realizable model after modification of the standard model constants for more complex flow field, is the calculation

of eddy viscosity and dissipation rate (Shih, Zhu, & Lumley, 1993). Re-normalization group $k-\varepsilon$ model, also called RNG model, using analytical re-normalization technique with scale expansions for the Reynolds stress provides modified constants of standard $k-\varepsilon$ model. Besides, $C_{1\varepsilon}$ in this model is replaced by $C^{*}_{1\varepsilon}$ which is calculated from an auxiliary function (Yakhot, Orszag, Thangam, Gatski, & Speziale, 1992).

2.6.2.2 $k-\omega$ Turbulence Model

The $k\text{-}\omega$ (Wilcox, 1998) is a two-equation turbulence model that uses the correlation between the length scale and the turbulence viscosity in terms of turbulence kinetic energy (TKE) and specific dissipation rate (ω). This model was reported to present reliable results in far wakes, mixing layers and more importantly wall-bounded flows and free shear flows which correspond to the conditions observed in heat treatment furnaces. The standard $k\text{-}\omega$ is determined by the following two transport equations (Wilcox, 1998):

$$\frac{\partial}{\partial t}(\rho k)+\frac{\partial}{\partial x_i}(\rho k u_i)=\frac{\partial}{\partial x_i}\left[\Gamma_k\frac{\partial k}{\partial x_i}\right]+G_k-Y_M+S_k \tag{2.35}$$

$$\frac{\partial}{\partial t}(\rho\omega)+\frac{\partial}{\partial x_i}(\rho\omega u_i)=\frac{\partial}{\partial x_i}\left[\Gamma_\omega\frac{\partial \omega}{\partial x_i}\right]+G_\omega-Y_\omega+S_\omega \tag{2.36}$$

Where G_k, G_ω, Y, and S are the TKE production due to velocity gradient, ω production due to velocity gradient , dissipation term and other source terms. Also, the terms Γ_k and Γ_ω are the diffusion coefficients, which can be calculated as follows:

$$\Gamma_k=\mu+\frac{\mu_t}{\sigma_k} \tag{2.37}$$

$$\Gamma_\omega=\mu+\frac{\mu_t}{\sigma_\omega} \tag{2.38}$$

Where μ, μ_t, σ_k, and σ_ω are the molecular viscosity, turbulence viscosity, TKE Prandtl number and Prandtl number for ω, respectively.

$$\mu_t=\alpha^{*}\frac{\rho k}{\omega} \tag{2.39}$$

Where α^* has the same role and meaning as C_μ in Eq. (2.32). In the $k\text{-}\omega$ model, α^* is calculated dynamically to provide a better compatibility with low Reynolds regions. Another $k\text{-}\omega$ model that is modified to account for the transport of the principal turbulent shear stress, is Shear-stress transport (SST) $k-\omega$ model (Menter, 1994). This model has a blending function to use the capabilities of near wall region of standard $k-\omega$ model with the free-stream independence of the $k-\varepsilon$ model in the far field. The definition of turbulent viscosity as well as modeling constant is modified in SST $k-\omega$ model with respect to standard $k-\omega$ model (Menter, 1994).

2.6.2.3 Reynolds Stress Model (RSM)

The Reynlods stress model (Cant, 2001; Launder, Reece, & Rodi, 1975) is one of the most elaborate turbulence models and is the most physically sound RANS based model. In two equation models, the turbulent viscosity is calculated using empirical or theoretical correlations between turbulence kinetic energy and eddy dissipation rate for specific flow conditions. The RSM model, on the other hand, solves all Reynolds stresses and turbulence dissipation instead of using eddy-viscosity concept. Thereby, RSM solves seven turbulence transport equations for three dimensional flows, considering the turbulence anisotropy (in contrast to two equation models which assume isotropic turbulence field). This model is more accurate for prediction of complex flows involving swirl, rotation and rapid changes that correspond to the gas-fired heat treatment furnaces which use high momentum burners and have a self-induced turbulence in the treatment chamber (Cant, 2001).

2.6.3 Comparison between Turbulence Modeling Approaches

Fig. 2.1 presents an overall illustration of comparison between above mentioned turbulence modeling approaches from the computational cost point of view.

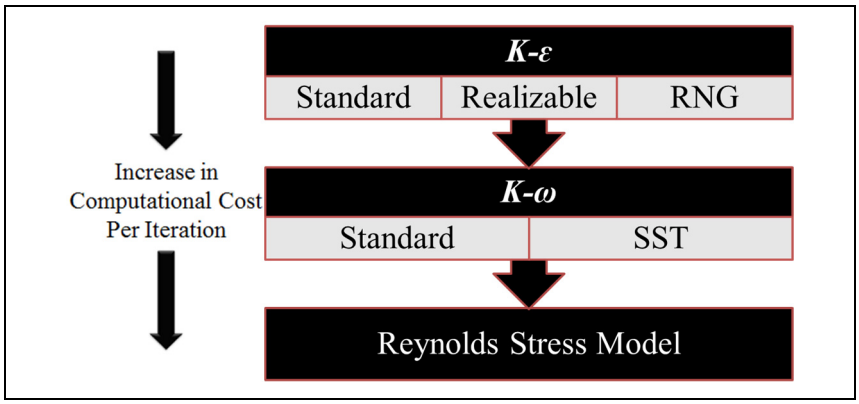

Figure 2.1 Comparison of computational cost per iteration for different available RANS models (ANSYS, 2016).

As it can be seen in Fig. 2.1, the computational cost per iteration increases from $k-\varepsilon$ group to Reynolds stress model. On the other hand, as briefly mentioned, each model has specific features and capabilities that should be considered for proper selection of the models and application to the thesis objectives and results interpretations. Below is a summary of each model capabilities and specifications (ANSYS, 2016; Davidson, 2011):

Standard $k-\varepsilon$: In this model, coefficients are calculated based on experiments on simple fully turbulent flows. This model has been widely used for thermal analysis of gas-fired furnaces (Denison, Borodai, Fox, & Bockelie, 2009; Y. J. Liu et al., 2016; C. Zhang et al., 2000). However, this model has limitations in complex flow including strong streamline curvature, separation or severe pressure gradient.

RNG $k-\varepsilon$: This model is a modified form of standard $k-\varepsilon$ model used for complex flows. It shows better results for flows involving, boundary layer separation, bluff bodies, moderate swirl and strong curvature making it a good candidate for the thermal analysis of gas-fired heat treatment furnace. However, the applicability of the model considering the flow field should be evaluated in the simulation of gas-fired heat treatment furnaces.

Realizable $k-\varepsilon$: This model theoretically performs similar to RNG $k-\varepsilon$ in a wide range of applications. This model is generally easier to converge in comparison to RNG and has

been reported to provide accurate results in continoues gas-fired furnace simulations (B Mayr, Prieler, Demuth, Moderer, & Hochenauer, 2017; Rezazadeh, Hosseinzadeh, & Wu, 2019; Tang et al., 2017). Therefore, this model along with other two equation $k-\varepsilon$ models will be assessed in the present context.

Standard $k-\omega$: Standard $k-\omega$ model has better performance for boundary-layer and free shear flows that can be found in several industrial flows like gas-fired furnaces (Denison et al., 2009). Regarding the fact that the main objective of the present research is to accurately predict the large size block temperature, this model is considered as one of the RANS based models.

SST $k-\omega$: This model that combines shear layer capabilities of the standard $k-\omega$ and away from wall of standard $k-\varepsilon$ has provided several reliable results in industrial applications including flow over a bluff body and impingement jets. However, its applicability based on the Re number and flow field in the gas-fired furnaces should be evaluated.

RSM: In this model, Reynolds stresses are solved using seven equations without an isotropic assumption of eddy viscosity. It makes this model as the most sound RANS model. However, extra CPU time and stability (due to closing several coupling equations) issues are the main concerns of RSM. It has been reported that RSM gives reliable results in complex 3D flows with strong streamline curvatures, swirl combustors and rotating flows such as gas-fired continuous furnaces (B Mayr, Prieler, Demuth, Potesser, et al., 2017; Prieler et al., 2016). Therefore, the RSM along with other numerical models will be evaluated in the thermal analysis of large size forgings heat treatment within gas-fired furnaces.

CHAPTER 3

EXPERIMENTAL MATERIALS AND METHODS

3.1 Introduction

The present chapter contains the details of the conducted industrial and laboratory scale measurements of the thesis. It will start with the details of furnace and temperature measurements in an industrial scale setup. Then, a calibration process of measurements as well as estimated thermo-physical properties will be presented. The laboratory physical simulation of the heat treatment process and its subsequent evaluation will be provided in the last section of the present chapter.

3.2 Furnace Description

The present investigation was conducted on an industrial gas-fired heat treatment furnace located at Finkl steel, St-Joseph-de-Sorel, Quebec (Finkl Steel Inc). The furnace medium drawings, including the dimensions are provided in Fig. 3.1.

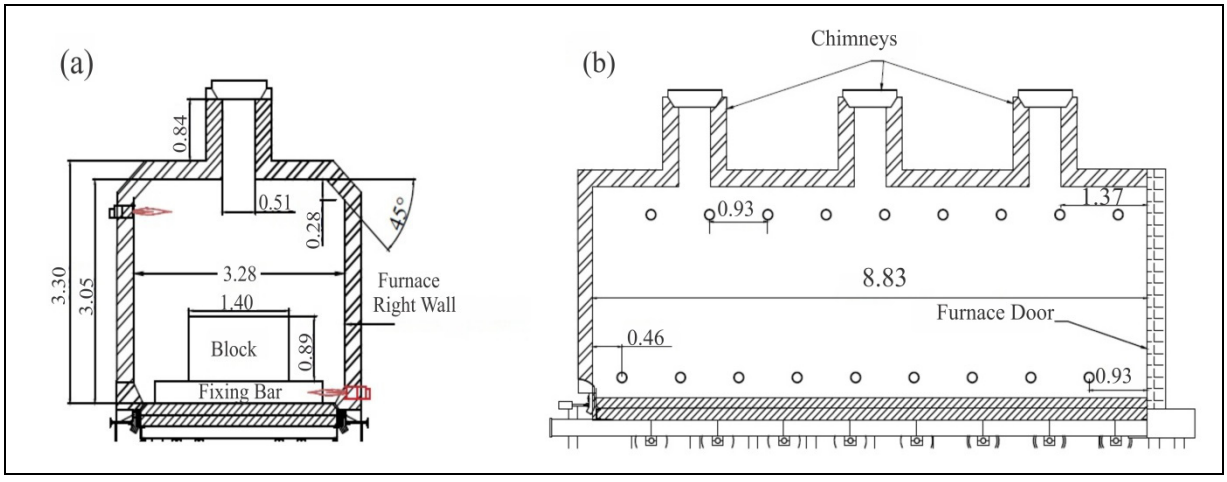

Figure 3.1 Dimensions and geometry of the car bottom gas-fired furnace in the (a) front view and (b) side view sketches (Bohlooli Arkhazloo et al., 2019).

Internal dimensions of the furnace in X, Y, and Z directions were 3.05 (m), 3.28 (m), and 8.83 (m), respectively. The furnace has 18 high-velocity Tempest cup burners (Fives North American Combustion, Inc.) located on the two sides of the furnace, along the Z direction with nine burners on the upper section of the furnace left wall, (upper burners) and the nine other in the lower section of the right wall (lower burners). This asymmetric arrangement improves temperature uniformity by self-induced recirculation and turbulence. Nine skids are positioned between the burners for placing the forged blocks.

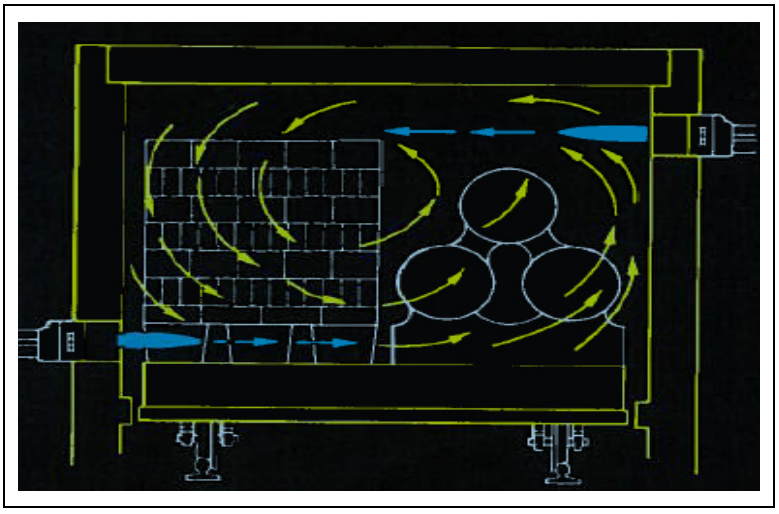

Figure 3.2 Self-induced turbulence within the gas-fired furnace (Pyradia Inc.).

The furnace temperature during the experimental measurements was controlled using a Honeywell UDC 2500 PID controlling system. PID controller divided the furnace length into three similar zones and by controlling the gas flow rate in each zone balanced the geometrical effects (door or back-wall) on the temperature variations in these zones. It allowed considering the one-third Periodic modeling of the furnace which is discussed in chapter 6. Fig. 3.3 shows the three zones of the furnace and periodic lines considered in the methodology of chapter 6.

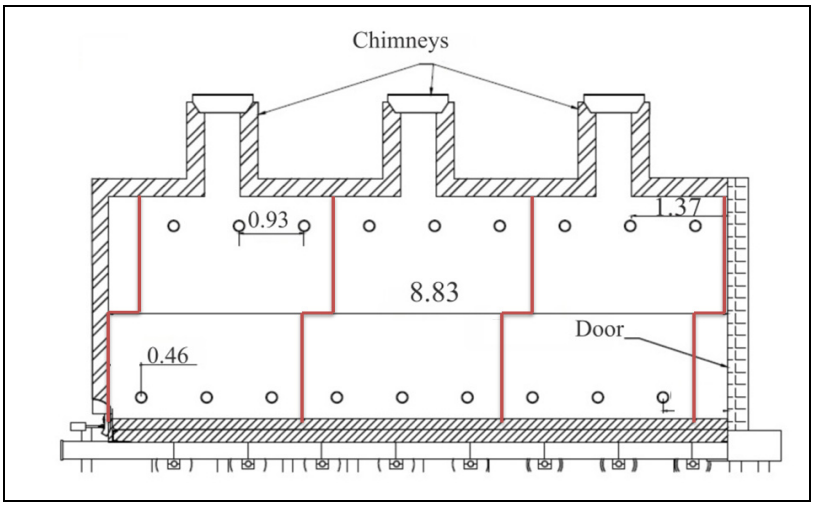

Figure 3.3 Schematic view of three zones of the furnace.

3.3 Temperature Measurements

Temperature measurements were divided into two steps of loaded and unloaded furnace to evaluate the loading effect on the temperature distribution inside the furnace and within the workpiece.

Firstly, sixteen standard sheathed K type thermocouples (TC) were installed at various positions of the empty furnace and a heating cycle consisting of different temperatures of the heat treatment process was applied (See Fig. 3.4). A ceramic material was used to encapsulate the thermocouples in the furnace medium. The results were interpreted not only to confirm the temperature uniformity of the furnace and its capability for the research study, but also to provide a cornerstone for the heat transfer analysis of the loaded furnace.

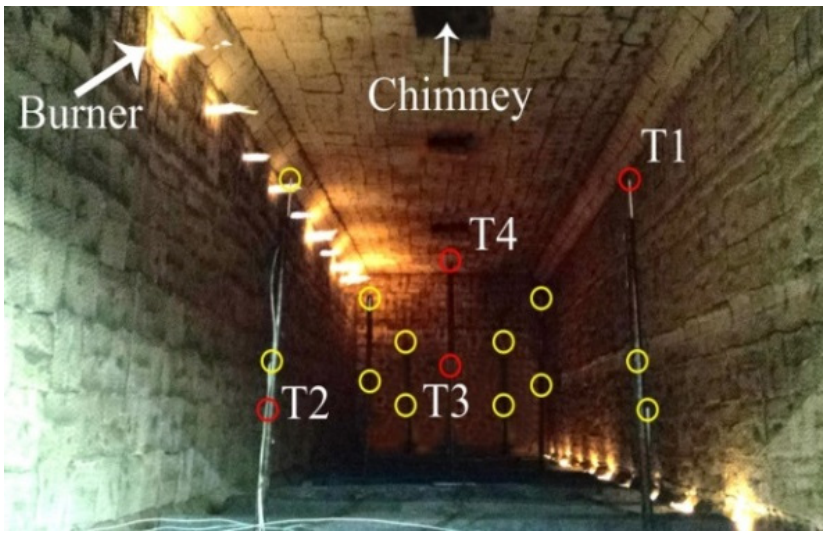

Figure 3.4 Experimental setup for temperature measurements of unloaded furnace in different locations of the furnace during the uniformity test.

The uniformity test results of the unloaded furnace are reported in Fig. 3.5. All of 16 TCs showed nearly the same temperature (conforming to the set temperatures) during the process. Therefore, only 4 of TCs (marked with red circles) are presented here. Also, the time history of the standard deviation of all the 16 thermocouple measurements is depicted in this Figure. The maximum standard deviation value during the heating history was 5.28°C and time averaged value of the deviation was 2.49°C. It is clear that the furnace medium has an acceptable uniformity at different operating temperatures. Maximum deviations were observed in the ramp stages, where the furnace increases its temperature to reach to the next target temperature.

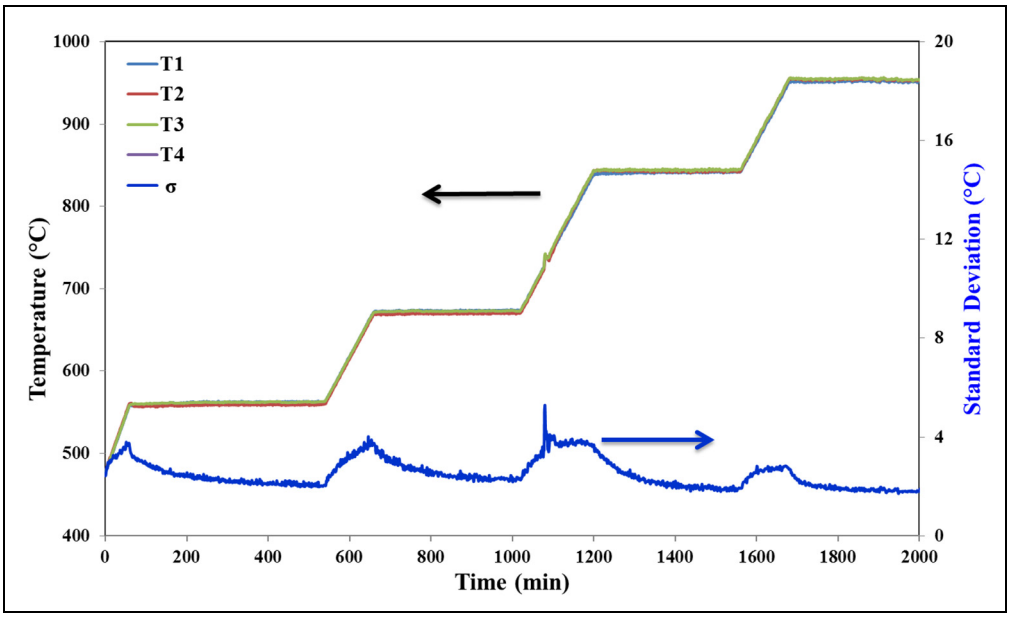

Figure 3.5 Temperature profile of furnace uniformity test and associated standard deviation.

In the loaded furnace, step of the temperature measurements, transient temperature evolution of a 1.4 × 0.89 ×2.72 (m^3) forged ingot was recorded by placing 11 K-type thermocouples at different locations of the block. TCs were installed at different surfaces of the forged block to evaluate and analyze the heating pattern around the workpiece. To ensure a solid attachment of all TCs, small holes (with the depth of 1(cm)) were drilled and thermocouples were solidly embedded at the bottom of the holes. The empty space of the hole was filled with iron powder of the same steel and the top of the hole was sealed with iron cement and a fixing screw (See Fig. 3.6). The standard accuracy of the K-type thermocouples with a stainless steel sheath according to ISA Standard is equal to ± 6.63 K (ISA Standard, 1982), for the furnace operating temperature ranges.

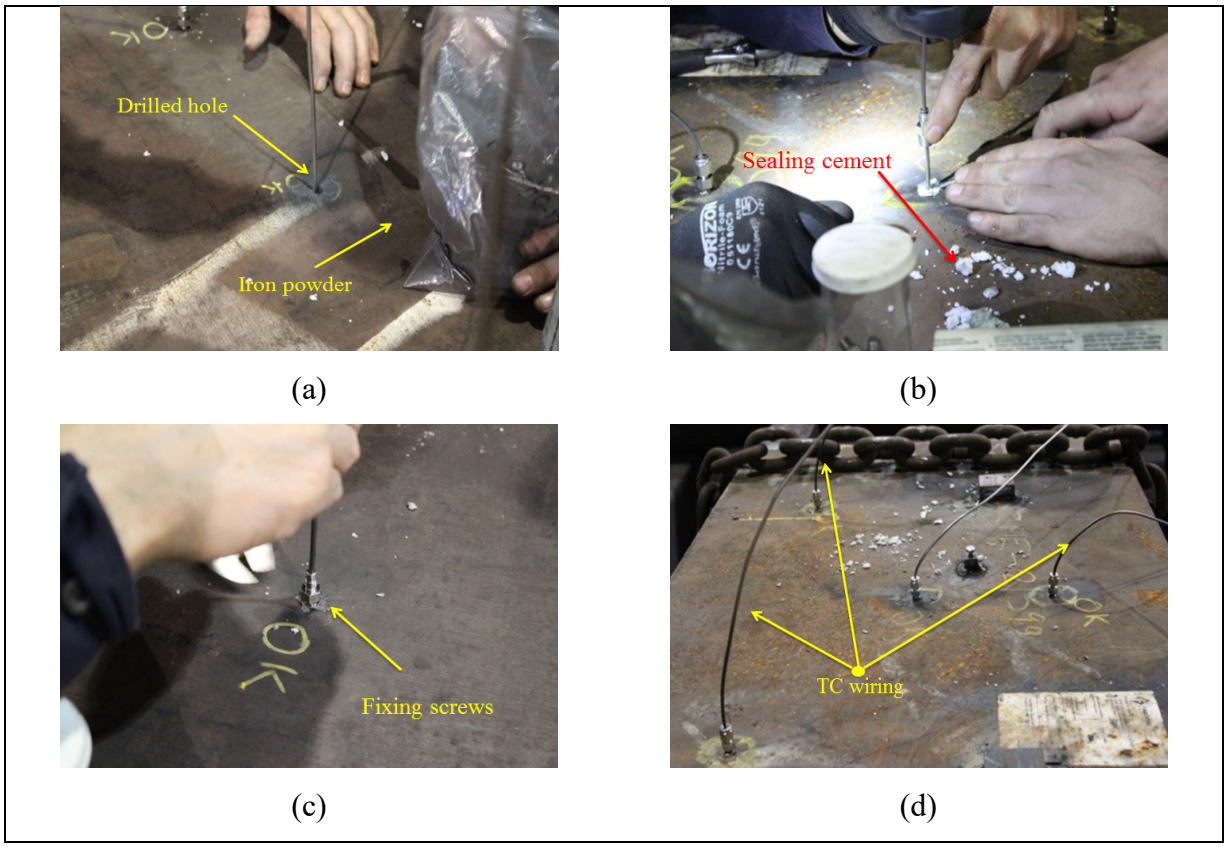

Figure 3.6 Procedure of thermocouples embedding on the forged block: a) filling the drilled hole with iron powder, b) sealing, c) screw fixing and d) wire locating

Six other TCs on the left and the right walls of the furnace and two TCs in the furnace medium were positioned to track the average furnace temperature. Moreover, to evaluate the heat loss through the furnace exhausts three thermocouples were installed at the center line of the chimneys (see section 3.5). The results were used both to confirm the CFD simulation results and heat balance analysis of the gas-fired furnace (see section 3.5).

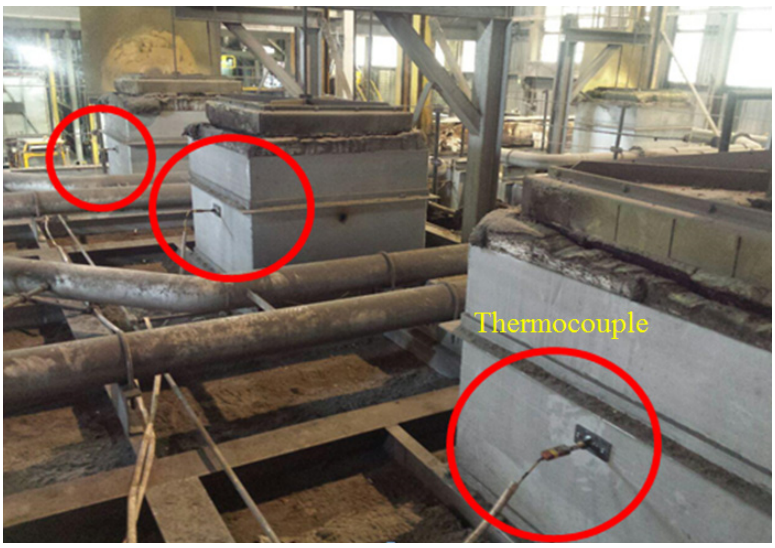

Figure 3.7 Installed thermocouples in the furnace chimneys for exhasut heat analysis.

A schematic view of the thermocouple positions on the large size forge block different surfaces is presented in Fig. 3.8. These positions were selected after preliminary simulation of the process and identification of the critical regions around the block. The center point of each surface of the block was instrumented by thermocouples. Besides, TC-1 was installed to record the stagnation area's temperature (the region where the combustion products were blocked by the forged ingot's surface). TC-2 recorded the skid affected area; while TC-9 and TC-4 were installed to quantify and analyze the non-uniformities on the same surfaces of the block considering their orientations with respect to the burners and block edges.

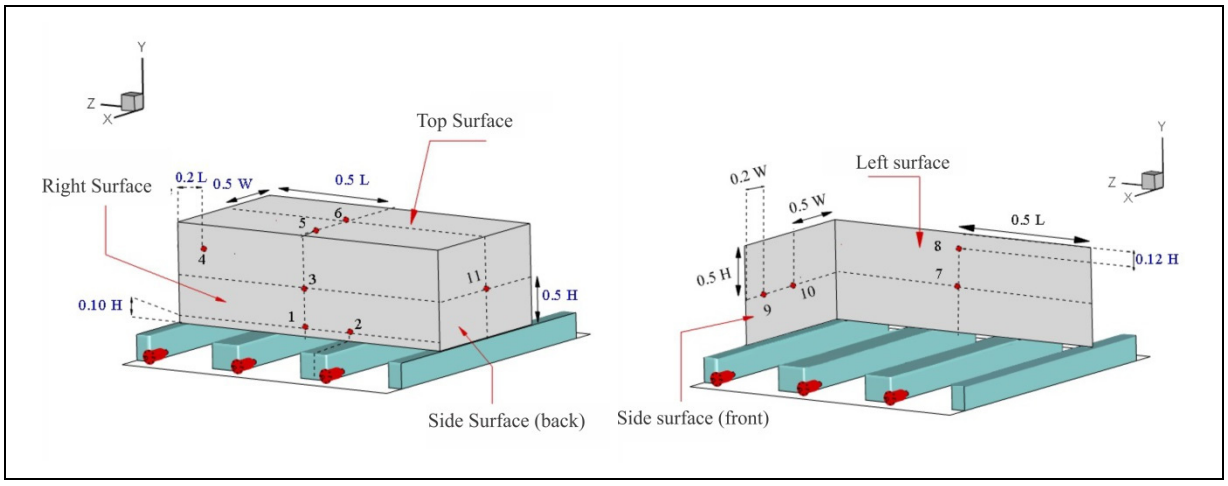

Figure 3.8 Schematic views of 11 thermocouples locations on the instrumented forged ingot.

Due to the large size of the furnace and workpiece, extensive care was taken to insure accurate installation of thermocouples and exact positioning and alignment of the block on the car-bottom furnace. However, a 1–2 (cm) error was estimated in the determination of probes positioning (see Fig. 3.8 and Fig. 3.9). Two other forged blocks with 1.4 × 0.79× 2.72 (m^3) dimensions were located in the front and back of the block to simulate the actual industrial practice. Fig. 3.9 shows two pictures of the forged ingots before and after 24 hours of the heat treatment process.

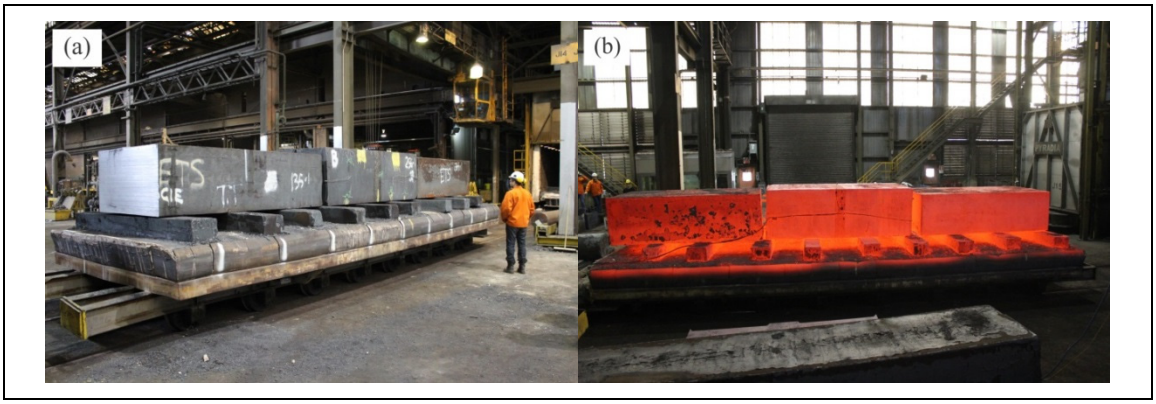

Figure 3.9 Forged ingots including test block: (a) before and (b) after the heat treatment and opining of the furnace door.

3.4 Flow Measurements

In the present study, gas flow metering were conducted using three pressure transducers along with a mini-max Honeywell electronic gas volume correctors installed on the furnace. Also, three pressure transducers were installed in three different zones of the furnace to measure the air usage for the burners' combustion. During the heat treatment process, the furnace was working under 5% excess air.

Figure 3.10 Installed flow metering devices on the gas-fired furnace burners to measure gas consumption.

3.5 Calibration Test

A set of calibration test was conducted on a small size block before the real scale measurements of the present study. The aim was to calibrate the measurement devices as well as measurement procedure. Besides, evaluation of thermo-physical properties predicted by the JMatPro software (Saunders, Guo, Li, Miodownik, & Schillé, 2003) and furnace performance (through calculation of wall and chimney's heat losses) were other objectives of this set of experimental measurements.

Due to the difficulties in temperature measurement of the large size block's center with the elaborated measurement techniques (vulnerability to cracks), a small size forged ingot was selected for this setup. The studied test block was a 0.51×0.77×1.03 (m^3) forged ingot with the same chemical composition of the project's steel. The chemical composition of the high-

strength medium carbon steel of the present study was (Wt. %) C: 0.35 – V: 0.15 – Mn: 0.99 – Si: 0.41- Ni: 0.5 – Cr: 1.86 – Mo: 0.53 – Cu: 0.16.

Seventeen TCs were used to record the temperature evolution of the test block. This number included thirteen TCs installed on different surfaces of the block (as depicted in Fig. 3.11) as well as three TCs that were located to track the quarter and center of the workpiece. Two other large size blocks with 1.4 × 0.79× 2.72 (m^3) dimensions were loaded on the furnace to simulate the actual industrial practice (See Fig. 3.12). During the calibration test, gas flow metering as well as exhaust temperature measurements were conducted.

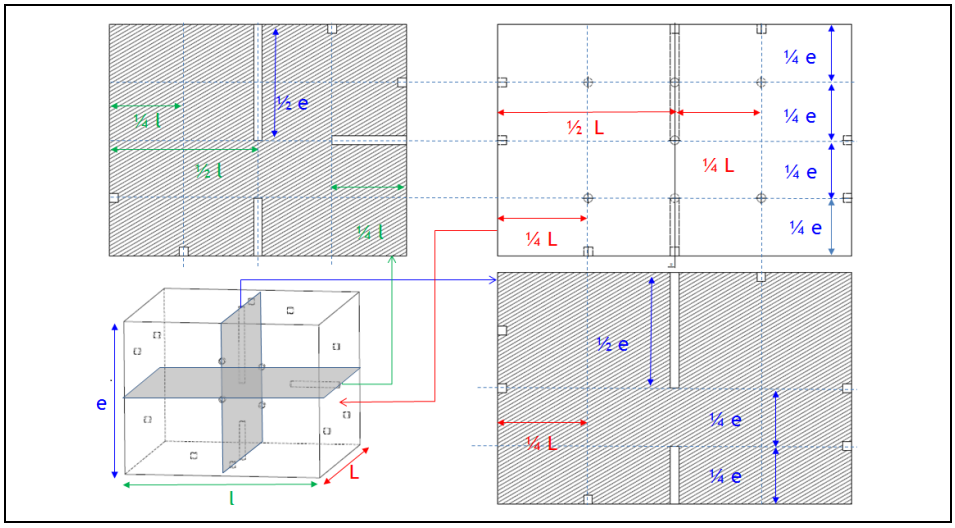

Figure 3.11 Schematic sketches of 17 thermocouples locations on the instrumented test block.

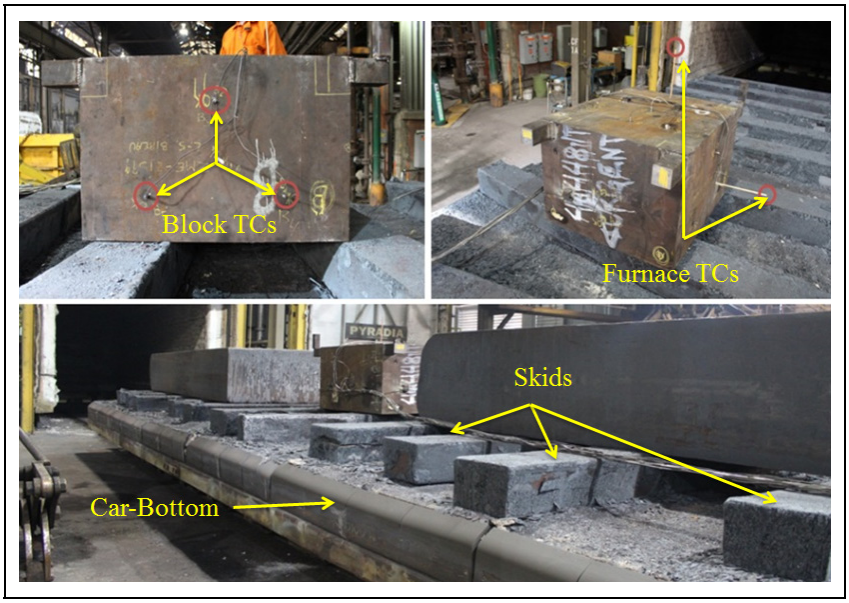

Figure 3.12 Instrumented test block loaded on the car-bottom furnace.

3.5.1 Block Measurements and Conductivity Calibration

To calibrate the measurement procedure and also validate the thermo-physical properties estimated by JMatPro software a 3D thermal transient FEM model of the test block was generated in ANSYS software. The experimentally measured temperatures at the surface of the test block were imposed as the boundary conditions to the model including 129406 tetrahedron elements. Thermo-physical properties estimated by the JMatPro software (depicted in Fig. 3.13) were used in the material properties specification of the model. Results of the numerically predicted transient temperature history of the test block's center and corresponding experimentally measured temperature in the calibration test are presented in Fig. 3.14.

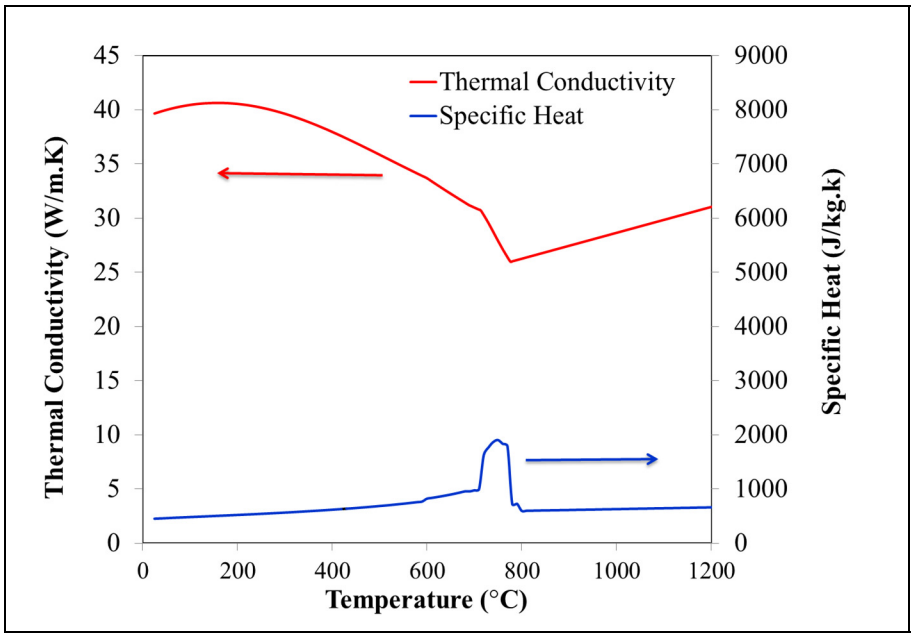

Figure 3.13 Temperature dependant thermo-physical properties of the ingot estimated by JMatPro.

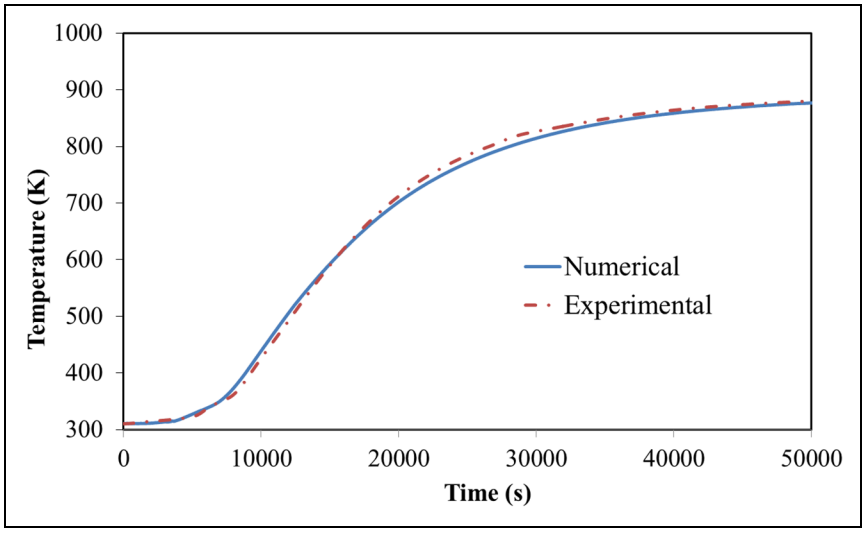

Figure 3.14 Comparison between numerically predicted and measured temperature evolution of test block's center point.

Results showed a good agreement between the FEM predictions and experimental measurements with a maximum deviation of 2.3%. The difference between the experimental

and numerical results is reasonable considering the dimensions of the block and limited number of TCs on the surface. Therefore, further investigations could be carried out using developed measurement procedure and estimated thermo-physical properties.

3.5.2 Furnace Refractories Heat loss Calibration

In the present study the refractories heat loss was calculated based on two different methods. The first approach was to calculate the heat loss using approach proposed by Hadala et al. (Hadała et al., 2017). To do so temperature-dependent thermal conductivities of furnace refractories (along with the JMatPro software's estimations for the forged block) should be defined to analyze the transient heat transfer in the heat treatment furnaces. Thermal conductivity of furnace refractories, on the basis of the technical documentations of the material used in the furnace, was available as it can be seen in Table 3.1.

Table 3.1 Thermal conductivity of the gas-fired furnace refractories (Morgan thermal ceramics, 2015).

Average Temperature	$260^{o}C$	$538^{o}C$	$816^{o}C$	$1093^{o}C$
(W/m.K)	0.08	0.16	0.28	0.43

This calculation resulted in an average value of 594 (w/m^2) heat losses for the furnace refractories. The second approach was to evaluate the refractories heat loss through zero dimension heat balance analysis of the furnace. The heat balance in a typical natural gas-fired furnace can be expressed as depicted in Fig. 3.15.

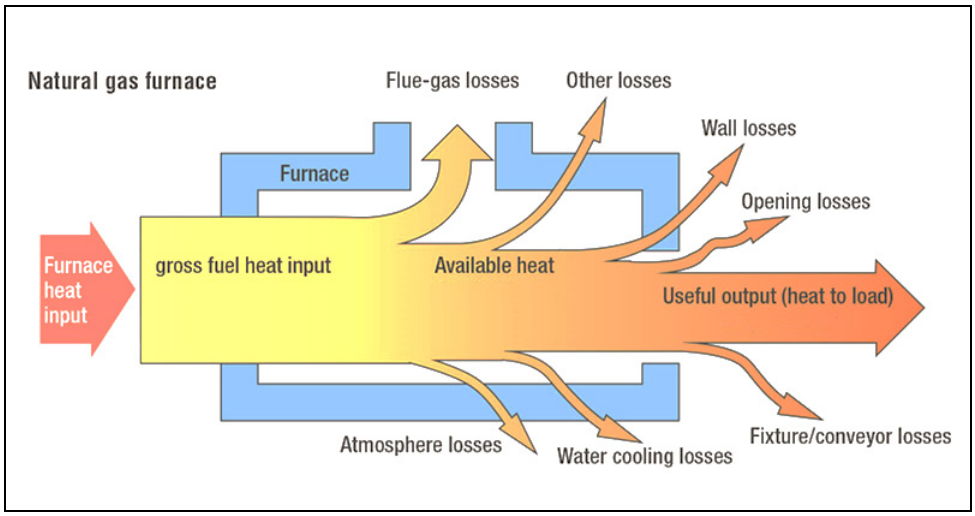

Figure 3.15 General energy balance in industrial furnaces (Mallela et al., 2019).

In the present study the effect of minor heat losses like opening losses or fixture losses and all other losses was added to the refractory losses to achieve a heat balance. Therefore, using the average temperature of the test block (predicted by the FEM model) and extrapolation of its results to the other two large size forged ingot (located on the furnace during the calibration test), the useful output of the gas combustion to the load was estimated. On the other hand, the available heat (see Fig. 3.15) in the furnace was calculated using computer based charts of the furnace manufacturer (Five Group Inc.). In these charts the amiable heat is calculated based on the furnace exhaust temperature and excess air used in the combustion. To do so, experimentally measured temperatures of the furnace chimneys were used considering the 5% excess air of the combustion. The difference between the calculated useful heat to the load (by FEM) and available heat (by thermal balance analysis) resulted in an averaged value of 622.5 (w/m^2) heat losses through furnace refractories. Considering the size of the furnace and accuracy of the measurement devices as well as employed correlations the calculated difference of 4.5% was reasonable. It should be noted that the calculated heat loss using furnace heat balance analysis also contains other types of furnace losses which is not considered in the approach of Hadala et al. (Hadała et al., 2017). Therefore, this analysis further confirmed that the experimental measurement procedure as

well as estimated thermo-physical properties are valid and further investigations can be carried out using the developed approach.

3.6 Laboratory Measurements

As a part of the present study, a numerical-experimental hybrid approach was developed to improve the furnace residence time of the large size block inside the gas-fired heat treatment furnace (see chapter 5). In this hybrid approach a series of laboratory experimental measurements was conducted using high resolution dilatometer machine (as the physical simulator of the furnace medium), and hardness measurements. Several non-isothermal and isothermal tempering cycles were physically simulated using the high resolution TA DIL 805A/D dilatometer machine. The heating rates using CFD results were adjusted to simulate that of actual heating cycle of forgings during heat treatment inside the furnace. To do so cylindrical samples 10 (mm) in length and 4 (mm) in diameter were cut from near the surface and central zones of the slab with the same chemical composition of the industrial scale forged block, which had underwent open-die forging at around 1260ºC. Rockwell C hardness measurements were conducted according to ASTM E18-19 on the polished surfaces of the heat treated samples to determine the impact of the heat treatment conditions on mechanical properties. A minimum of 25 measurements were used for all the tests with a load of 1 kg and a dwell time of 10 s.

3.7 Project Approach

A summary of project approach including sequences of different numerical/experimental steps of the research (discussed in chapters 2 and 3) is illustrated through in Fig. 3.16. Also, the flowchart of simulations and subsequent optimizations including numerical details (modeling, grid generation, numerical approaches, validation and post process) is shown in Fig. 3.17 (see also methodology sections of chapters 4, 5 and 6).

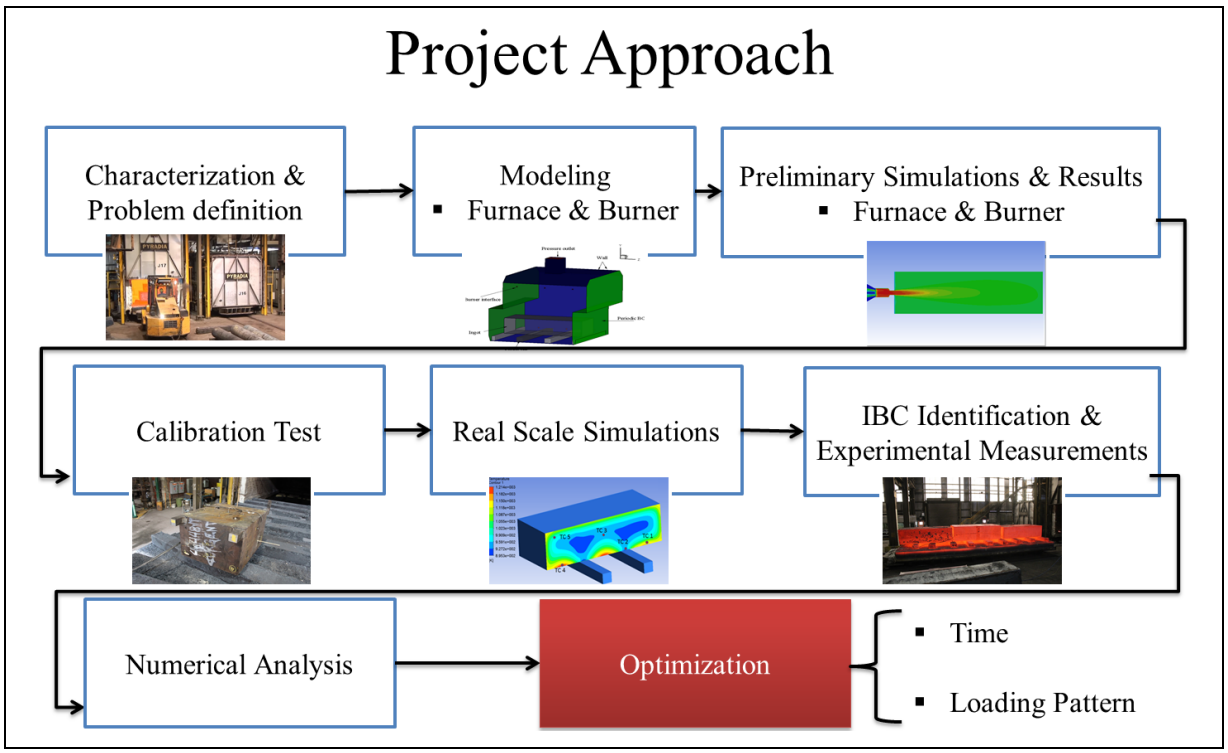

Figure 3.16 Successive numerical/experimental steps of the research through optimization objective

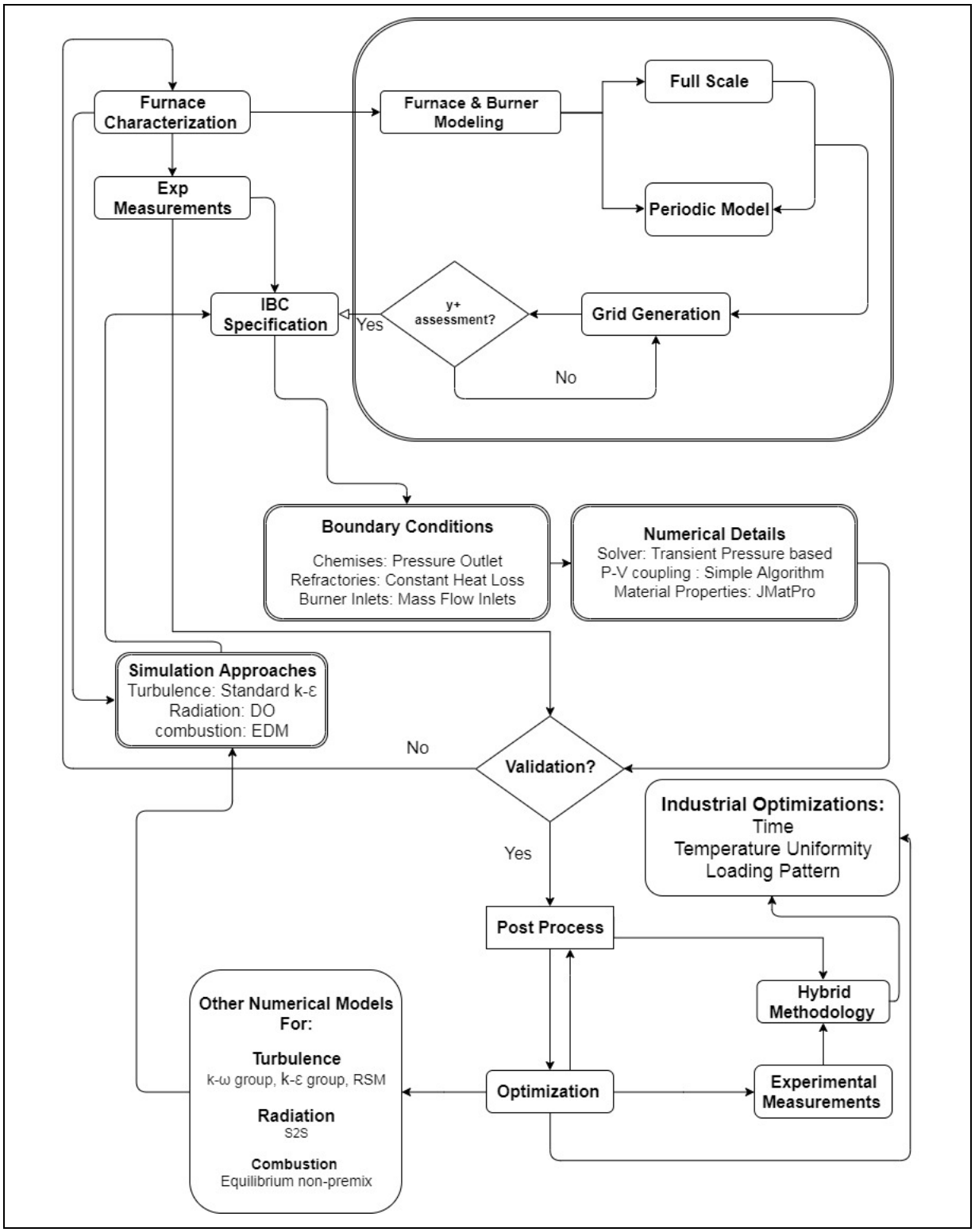

Figure 3.17 CFD simulations and subsequent optimization flowchart

CHAPTER 4

EXPERIMENTAL AND UNSTEADY CFD ANALYSES OF THE HEATING PROCESS OF LARGE SIZE FORGINGS IN A GAS FIRED FURNACE

Nima Bohlooli Arkhazloo[a,*], Yassine Bouissa[a], Farzad Bazdidi-Tehrani[b], Mohammad Jadidi[b], Jean-Benoît Morin[c] and Mohammad Jahazi[a]

[a] Département de Génie Mécanique, École de Technologie Supérieure, Montréal, Québec, Canada H3C 1K3,

[b] School of Mechanical Engineering, Iran University of Science and Technology, Tehran, Iran 16846-13114

[c] Finkl Steel Inc., 100 McCarthy, Saint-Joseph-de-Sorel, Québec, Canada J3R 3M8

Paper published in *Case Studies in Thermal Engineering,* February 2019*,*

Abstract

Comprehensive unsteady analysis of large size forged blocks heating characteristics in a gas-fired heat treatment furnace was carried out employing experimentally measured temperatures and computational fluid dynamics (CFD) simulations. Heat and fluid flow interactions, consisting of turbulence, radiation and combustion, were simultaneously considered using $k-\varepsilon$, DO and EDM models in a three dimensional CFD model of the furnace, respectively. Applicability of the S2S radiation model was also evaluated to quantify the effect of participating medium and radiation view factor in the radiation heat transfer. Temperature measurements at several locations of an instrumented large size forged block and the furnace chamber were performed. A maximum deviation of about 7% was obtained between the model predictions and the experimental measurements. Results showed that despite the unloaded furnace had uniform temperature distribution, after loading, product surfaces experienced different heating rates, resulting in temperature differences up to 200 K. Findings were correlated with furnace geometry, vortical structures and flow circulations around the workpiece. Besides, S2S model demonstrating reliable results highlighted the

importance of radiation view factor optimization in this application. The study could directly be employed for optimization of the heat treatment process of large size steel components.

Keywords: Heat treatment, CFD simulation, Gas-fired furnace, Temperature measurement, Heating uniformity, Radiation modeling

Nomenclature

Latin symbols

a	Absorption coefficient
E	Energy
F_{kj}	View factor between surface k and surface j
g	Gravity (m/s^2)
J_i^z	Diffusive flux of chemical species
h	Enthalpy (J/kg)
I	Radiation intensity
k	Turbulence kinetic energy (m^2/s^2)
k_{eff}	Effective conductivity
$\dot{m}$	Mass flux ($kg/\mathrm{m}^2.s$)
n	Refractive index
p	Pressure (Pa)
q_i,	The generic source term
q_r	Reaction heat term
$\vec{r}$	Position vector
R_z	Production rate of z_{th} component
$R_{z,r}$	Production rate of z_{th} component in the reaction
Re	Reynolds number (ud/μ)
Sc	Schmidt number
S_z	Source term of z_{th} component
s	Path length
$\vec{s}$	Direction vector
$\vec{s}'$	Scattering direction vector
t	Time (s)
t_T	Total heat treatment time (s)

T	Temperature (K)
u_i	Reynolds-averaged velocity in tensor notation
u_i'	Resolved fluctuating velocity components
Y	Mass fraction of species
X, Y, Z	Direction of coordinate axes

Greek symbols

ε	Turbulence dissipation rate (m^2 / s^3)
ε_k	Surface emissivity
Ω'	Solid angle
τ_{ij}	Viscous stress tensor
μ_t	Turbulence eddy viscosity($kg.m / s$)
σ	Stefan-Boltzmann constant
σ_s	Scattering coefficient
ρ	Density (kg / m^3)
ρ_k	Surface reflectivity
$\rho\overline{u_i' u_j'}$	Reynolds stress ($kg / \mathrm{m}.s^2$)

Superscripts

'	Fluctuations with respect to a Reynolds averaging

Subscripts

eff	Effective
i, j, k	Tonsorial indices
z	z_{th} species

Abbreviation

3D	Three dimensional
CFD	Computational Fluid Dynamics
DO	Discrete ordinates model
S2S	Surface to surface

4.1 Introduction

A significant number of high strength steel parts used for critical applications in energy and transportation industries acquire their required properties through a sequence of heat treatment processes often called Quench and Temper (Q&T) (Totten, 2006). The heating process is one of the most important steps since major microstructural changes (grain refinement, phase transformation, etc.) take place, that have a direct impact on the final mechanical properties (Kang and Rong, 2006). Hence, heat transfer from the furnace to the work piece, which fundamentally depends on the temperature distribution inside the furnace, significantly influences the quality of the final product (Gao et al., 2000). The process becomes more critical when it comes to the heat treatment of large size parts, such as turbine shafts. Specifically, a non-uniform temperature distribution may result in local changes in the microstructure, leading to non-uniform properties in different locations of the final part. Therefore, accurate temperature prediction of the parts necessitates a quantitative analysis of the transient heating and an understanding of thermal interactions within the furnace.

Comprehending the complexities of the thermal field, along with the turbulent fluid flow inside the heat treatment furnace is very challenging. Complicated load-gas-furnace thermal interactions, including transient convection-radiation heat transfer, impose strong non-linear thermal boundary conditions to the load. Chapman et al. (Chapman et al., 1990) employed analytical and Gao et al. (Gao et al., 2000) used semi analytical methods, to develop general correlations for the heat treatment schedule and temperature evolution of products. However, analytical studies are generally limited to linear problems and become very complex when non-linear transient conditions or interactions between phenomena are included. On the other hand, experimental measurements in this particular field of study are very challenging; especially, in the case of large size products, reliable data acquisition during the process is more complex.

Therefore, numerical methods such as computational fluid dynamics (CFD) offering simultaneous analysis of turbulent fluid flow, combustion and conjugate heat transfer could

be an excellent tool for simulating and subsequently optimizing the heat treatment process. 3D full scale numerical models are critical in the implementation process of smart manufacturing technology's (Industry 4.0) practices. Different furnaces such as electrically heated or gas quenching furnaces have been studied using CFD (Cosentino et al., 2013; Hao et al., 2008; J. Wang et al., 2008). However, among the above furnaces, the simulation of the heat treatment in gas-fired furnaces are more complex due to reactive flow combined with turbulent transport and conjugate heat transfer including absorbing and emitting hot combustion products. Inherently, the problem is more acute when it comes to large size furnaces and therefore little data is available in the scientific literature. Recently, Liu et al. (Y. J. Liu et al., 2016) using CFD, proposed a basic model for increasing the uniformity in continues gas-fired furnaces. Mayr et al. (B Mayr, Prieler, Demuth, Moderer, et al., 2017) used a one-step steady state CFD approach and Tang et al. (Tang et al., 2018) a combination of 3D CFD and 2D finite difference methods to predict temperature evolution in pusher type gas-fired furnaces. However, very little data is available on large size batch type furnaces. Besides, most of the experimental studies have been used as a validation tool of the simulation. The limited published studies have been devoted to one aspect of the process (i.e., burner positions, furnace chamber, or product heating characteristics). For example, Danon et al. (Danon et al., 2011) assessed burner positioning effects on the performance of multi-burner combustion furnace and Galletti et al. (Galletti et al., 2013) mainly focused on different combustion models for the burner simulation inside a semi-industrial furnace. Prieler et al. (Prieler et al., 2015) employing experimental validation demonstrated the applicability of CFD for combustion modeling of flat burners in a lab-scale heat treatment furnace. Recently, Mayr et al. (B. Mayr, Prieler, Demuth, Potesser, et al., 2017) presented a combustion model, with lower computational demand, for semi-industrial gas-fired furnaces.

The objective of the present study is therefore to carry out a comprehensive analysis of heat transfer in the heat treatment process of forged blocks in a large size gas-fired furnace employing both experimental measurements and CFD simulation. The experimental data was generated through the instrumentation of the furnace chamber (loaded and unloaded) as well as the different surfaces of the block during the heat treatment process. Unsteady CFD

analysis using a combination of $k-\varepsilon$, EDM and DO models was employed to identify the effects of different geometrical and process related parameters on corresponding heat transfer modes. In addition, S2S radiation model was employed to assess its applicability in this type of heat treatment furnaces and to quantify the effect of radiation heat transfer parameters on the temperature evolution of the product.

4.2 Experimental procedures

The instrumented furnace was a 3.05×3.28 ×8.83 (m^3) car bottom gas-fired furnace equipped with 18 high-velocity cup burners (Baukal Jr, 2003) located on the two sides of the furnace, along the Z direction with nine burners on the upper section of the furnace left wall, (upper burners) and the nine other in the lower section of the right wall (lower burners).

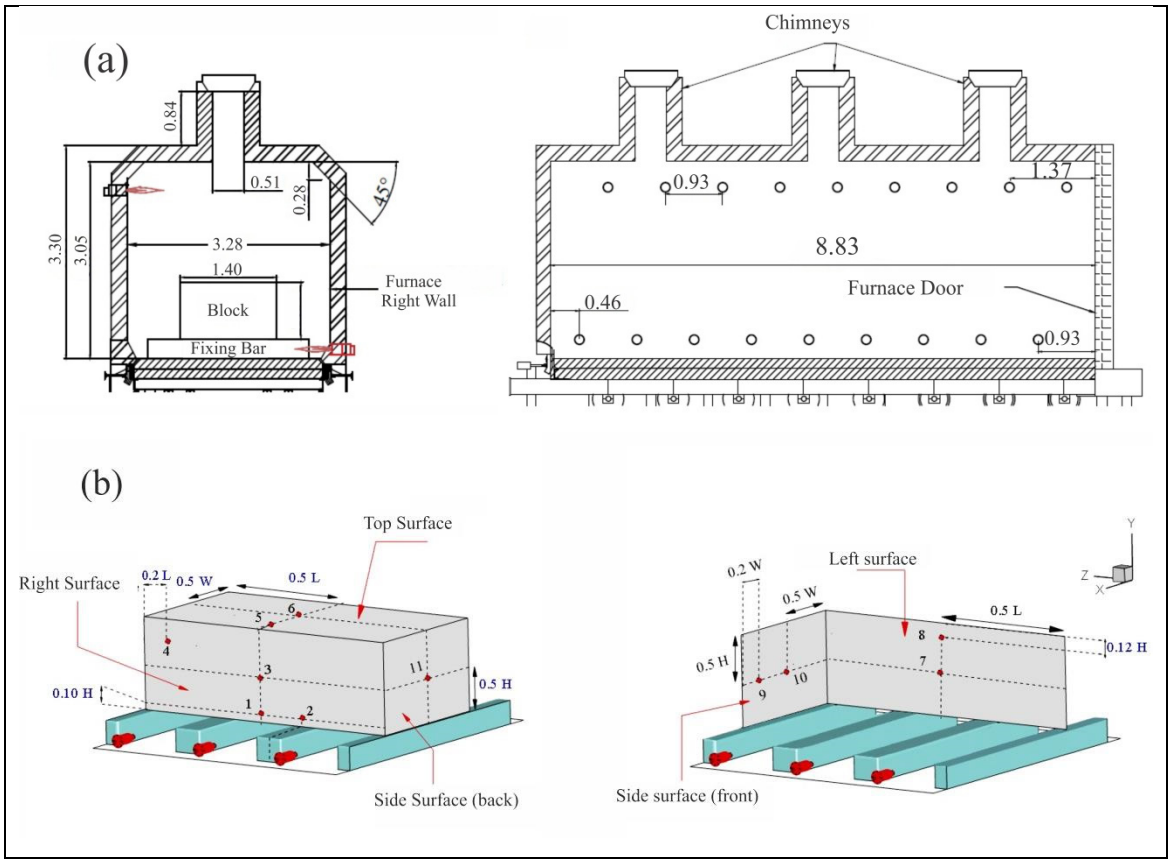

Figure 4.1 Dimensions and geometry of the car bottom gas-fired furnace and (b) Schematic views of thermocouples locations on the instrumented forged ingot.

Under ideal operational conditions, the burner flame length and the combustion product velocity at the exit of burner should be 0.508 (m) and 107 (m/s), respectively. Nine fixing bars with a cross section of 0.25 (m) × 0.25 (m) and a length of 2.60 (m) are positioned between the burners for placing the forged ingots. The furnace was operated under a positive pressure of approximately 0.2 (mbar) to minimize any air entry. The furnace medium drawings, including the dimensions are provided in Fig. 4.1 (a). Experimental measurements were divided into two steps of loaded and unloaded furnace to evaluate the loading effect on the temperature distribution inside the furnace and on the forged block. Sixteen-standard sheathed K-type thermocouples (TC) were installed at different positions of the unloaded furnace; and temperature evolution during an entire heat treatment cycle (i.e. heating, isothermal holding, and cooling). The results were used both to confirm the temperature uniformity of the furnace and to provide a basis for the heat transfer analysis of the loaded furnace.

Also, temperature evolution in the loaded furnace was recorded by placing 11 K-type TCs at different locations of a 1.4 × 0.89 ×2.72 (m^3) forged block. These thermocouples were fixed to the different surfaces of the block to evaluate the heating pattern around the workpiece (See Fig. 1(b)). To ensure a solid attachment of all TCs, small holes were drilled and TCs were solidly embedded at the bottom of the holes. The empty space of the hole was filled with iron powder of the same steel and the top of the hole was sealed with iron cement and a fixing screw. The standard accuracy of the K-type thermocouples with a stainless steel sheath is equal to $\pm 0.75 \times T$ (ISA Standard, 1982), which corresponds to an accuracy of ±6.63 (K) for the furnace operating temperature ranges. Considering the large size of the furnace and workpiece, extensive care was taken to insure accurate installation of the 11 TCs and exact positioning and alignment of forged ingot on the car-bottom furnace; however, a 1–2 (cm) error was estimated in the determination of probes positioning. In order to simulate heat transfer conditions, as close as possible to real operational conditions, two other forged blocks with 1.4 × 0.79× 2.72 (m^3) dimensions were also placed in the front and back of the instrumented block.

4.3 Computational Details

4.3.1 Flow simulation

A transient CFD simulation applying a pressure-based solver was employed to solve the density weighted Reynolds-averaged Navier-Stokes (RANS) equations, as follows (ANSYS, 2016):

$$\frac{\partial \rho}{\partial t} + \frac{\partial}{\partial x_i}(\rho u_i) = 0 \tag{4.1}$$

$$\frac{\partial}{\partial t}(\rho u_i) + \frac{\partial}{\partial x_j}(\rho u_i u_j) = -\frac{\partial p}{\partial x_i} + \frac{\partial \tau_{ij}}{\partial x_j} - \frac{\partial}{\partial x_i}(\rho \overline{u_i' u_j'}) + F \tag{4.2}$$

$$\frac{\partial}{\partial t}(\rho E) + \frac{\partial}{\partial x_j}(\rho u_i h) + \frac{\partial}{\partial x_j}(u_i p) = \frac{\partial}{\partial x_i}(\mathrm{k}_{eff}\frac{\partial T}{\partial x_i} - \sum_{z=1}^{n} h_z \overset{\mathrm{r}}{J}_z + u_i \tau_{ij}) - \frac{\partial}{\partial x_j}(\overline{\rho u_i' h_s'}) + q_s \tag{4.3}$$

where, the stress tensor, τ_{ij}, is given by:

$$\tau_{ij} = \left[\mu\left(\frac{\partial u_i}{\partial x_j} + \frac{\partial u_j}{\partial x_i}\right)\right] - \frac{2}{3}\mu\frac{\partial u_l}{\partial x_l}\delta_{ij} \tag{4.4}$$

and the diffusive flux of combustion product species is defined by the Fick's law:

$$\overset{\mathrm{r}}{J}_z = -\frac{\mu_t}{Sc_k}\frac{\partial Y_z}{\partial x_i} \tag{4.5}$$

The definition of all the variables and related units are provided in the nomenclature page. According to the literature (Liu et al., 2014) the two-equation standard k - ε turbulence model (Launder & Spalding, 1972), could be reliably used to determine the turbulence associated with the gas combustion in the gas-fired furnaces by solving the additional turbulence kinetic energy (k) and dissipation rate (ε) equations (Launder & Spalding, 1972).

4.3.2 Radiation modeling

In the present work, the discrete ordinates (DO) model (Chui & Raithby, 1993) was used to solve the radiative transfer equation (RTE), Eq. (4.6), considering the absorption and emission effects.

$$\frac{\mathrm{d}\, I\,(\vec{r},\vec{s})}{ds}+(a+\sigma_s)I\,(\vec{r},\vec{s})=a\,\mathrm{n}^2\,\frac{\sigma T^4}{\pi}+\frac{\sigma_s}{4\pi}\int_0^{4\pi} I\,(\vec{r},\vec{s})\phi\,(\vec{r},\vec{s})\,\mathrm{d}\,\Omega' \qquad (4.6)$$

I is the radiation intensity and $(a+\sigma_s)$ is the optical thickness of the medium. Due to the presence of combustion products the weighted-sum-of-gray-gases model (WSGGM) using the coefficients provided by Smith et al. (Smith, Shen, & Friedman, 1982) was employed to compute the radiative properties inside the furnace. For WSGGM model, the domain-based approach was employed to calculate the mean beam length (ANSYS, 2016).

The applicability of the S2S model, as a computationally effective method in the optically thin medium, was also evaluated in the present work along with the DO model. The S2S model assumes any absorption, emission, or scattering of radiation by the medium can be ignored; thereby, reducing the computational cost by only considering the surface-to-surface radiation. In this model, the radiation heat transfer to a surface from another surface is a direct function of the surface-to-surface view factor. Therefore, the radiation energy balance for each surface follows Eq. (4.7).

$$q_{out,k}=\varepsilon_k\sigma T_k^4+\rho_k\sum_{j=1}^{N}F_{kj}q_{out,j} \qquad (4.7)$$

F_{kj} is the view factor between surface k and surface j.

4.3.3 Combustion modeling

Combustion inside the burner and furnace domains was modeled using the eddy-dissipation model (EDM). It should be noted that, because in the gas-fired furnace the burners create high velocity combustion products, the Arrhenius chemical kinetic calculations were not considered thereby the computational cost is significantly reduced. In EDM, the species

transport formulation for the local mass fraction species (Y_z), for the z_{th} species, was solved assuming that the reaction rates were dominated by turbulence (B. F. Magnussen & Hjertager, 1977) Therefore, the species transport equation becomes as follows (ANSYS, 2016):

$$\frac{\partial}{\partial t}(\rho Y_z) + \nabla.(\rho \bar{v} Y_z) = -\nabla.\overline{J_z} + \dot{R}_z + \dot{S}_z \quad (4.8)$$

where, $\dot{R}_z$ represents the net production rate of the z_{th} component. In the above equation, the reaction rate is calculated on the basis of eddy mixing scale, k/ε, and the eddy-break (Launder & Spalding, 1972).

4.3.4 Numerical simulation procedure and boundary conditions

CFD simulations were carried out using the finite-volume based ANSYS-FLUENT software (ANSYS, 2016). The unsteady SIMPLE algorithm (H K Versteeg & Malalasekera, 2007) was applied to 15,155,000 hexahedral non-uniform computational grids as illustrated in Fig. 4.2. Grid value includes 356,000 non-uniform cells in each burner domain (6,408,000 in total for 18 burners) and finer grids near the burner exit to capture the combustion phenomenon and heat and fluid flow coming from burners to the furnace domain. Non-uniformly distributed grids with finer grid sizes near the walls and burner interfaces were employed to consider the effects imposed by velocity and thermal boundary layers. Also, second order discretization is used for the simulations. Averaged heat loss of 594 (W/m^2), calculated based on the approach proposed by Hadata et al. (Hadała et al., 2017), was applied to the furnace walls. The emissivity of the furnace refractories and the steel workpiece were set to 0.75 and 0.8 (corresponding to an oxidized steel surface), respectively. The mass flow inlet boundary conditions with averaged values of 0.018 (kg/s) and 0.516 (kg/s) were considered for the gas and air inlets, respectively, while pressure outlet was considered for the chimney exhaust. Calculations at each time step continued up to a convergence criterion (residual) of 10^{-5}, 10^{-6}, and 10^{-9} for the continuity, energy and radiation equations, respectively.

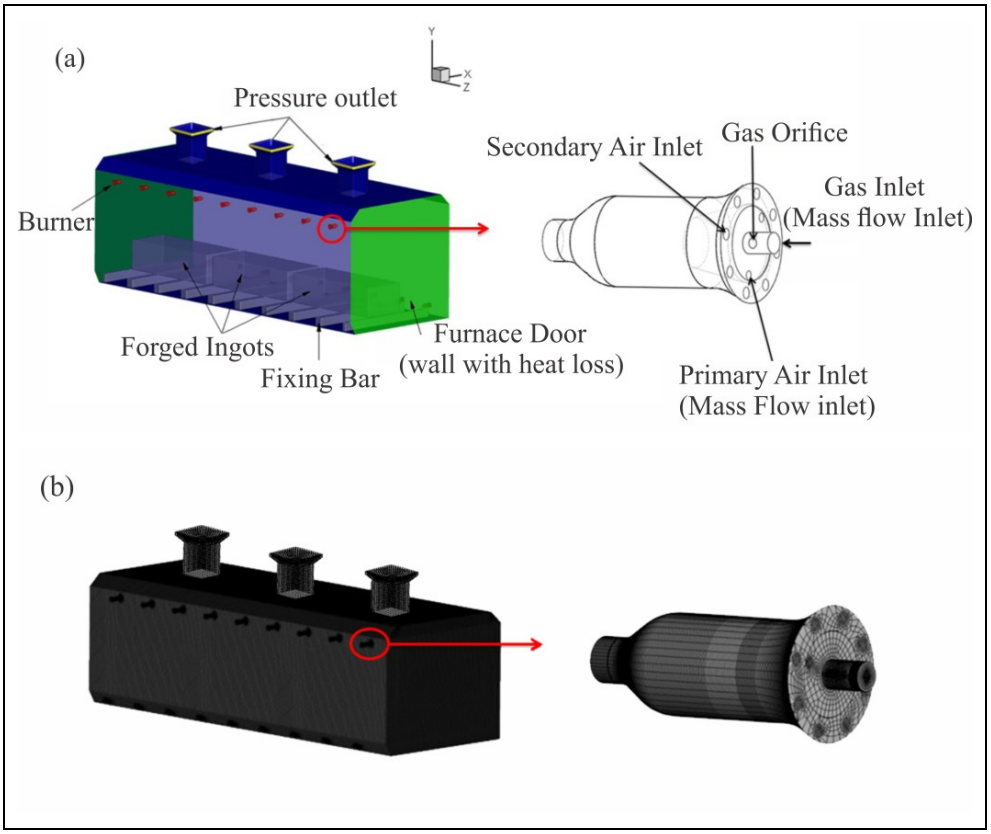

Figure 4.2 Computational domain, including: (a) boundary conditions and (b) computational grids.

Table 4.1 Chemical analysis of the test forged ingot used for thermo-physical properties calculation % weight (Finkl Steel Inc.)

C	Mn	Si	Mo	Cr	Ni	Other
0.35	0.85	0.4	0.45	1.85	0.47	Micro-alloying

4.4 Results and Discussion

4.4.1 Experimental Analysis

The uniformity test results of the unloaded furnace showed a very conformity with the predefined heating pattern with a maximum standard deviation value of 5.28°C during the ramp stage with the furnace increasing its temperature to reach the target temperature.

Therefore, it can be considered that the unloaded furnace presents a good temperature uniformity over its entire volume during the entire heat treatment cycle.

The measured temperature histories of different locations of the forged block are illustrated in Fig. 4.3. The results reveal a clear difference in temperature evolution as a function of the location of the TCs (i.e. considered face and TCs position on the surface).

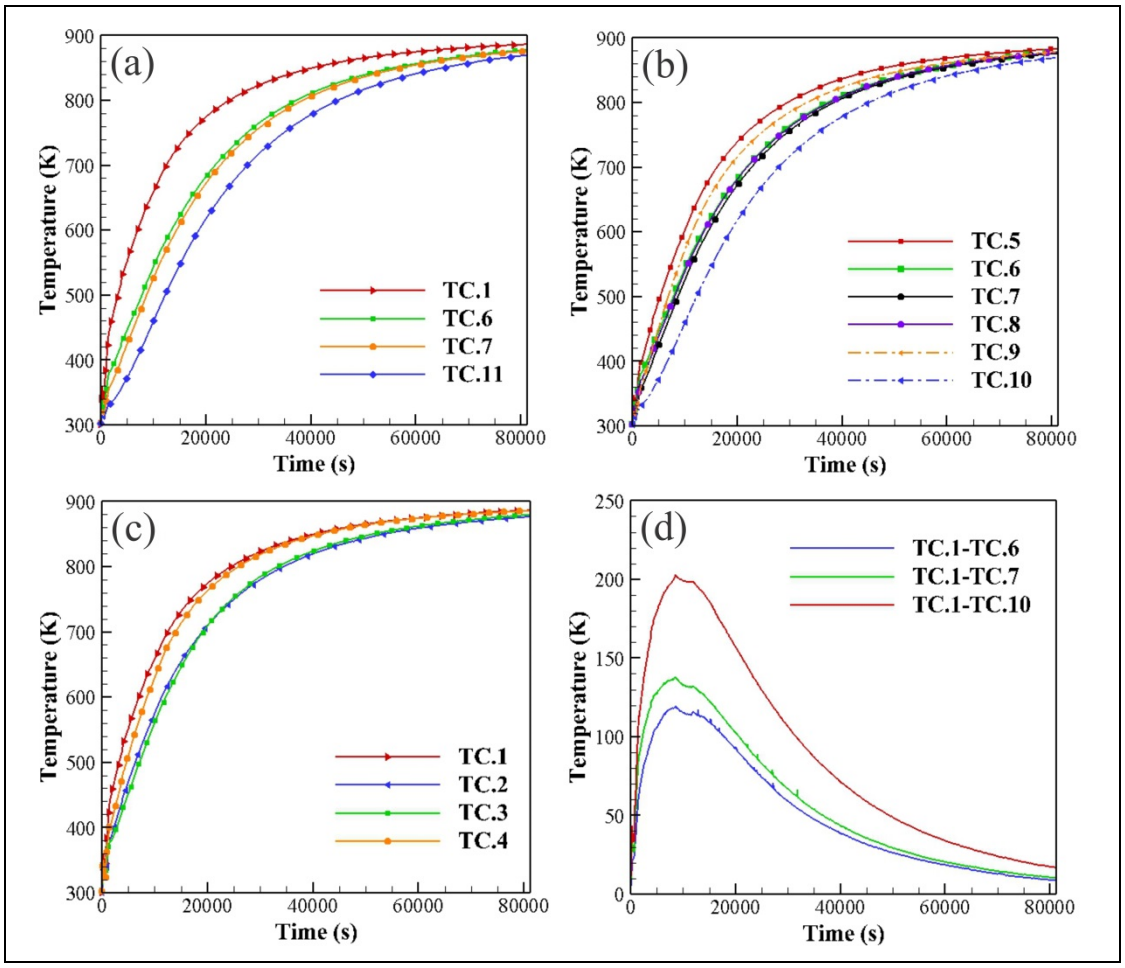

Figure 4.3 Experimentally measured temperature evolution of TCs on: (a) different surfaces of the forged ingot, (b) left, top and side surfaces, (c) right surface and (d) their relative temperature differences.

Usually, severity and continuity of the temperature gradient between the surface and the center of the workpiece is one of the main concerns of steel making industries, as it directly

impacts the quality of the final product (Totten, 2006). However, Fig. 4.3 (a) shows that apart from the temperature gradient inside the workpiece, differences in temperature can also be found on the surfaces themselves (see Fig. 4.1 for locations of TCs). Although, temperatures of all TCs on the surfaces ultimately converge to the target pre-defined temperature at the end of the process, the temperature histories of different points of the forged ingot are not identical. This variability in the heating history could affect the microstructural transformations from one end to another end of the product (subsequently its properties), and needs to be taken into consideration when developing microstructure based models of phase transformation.

As indicated in Fig. 4.3, it is clear that the TC on the right surface (TC.1), located at a shorter distance to the burner (lower burners) had higher temperatures in comparison to those of the left and the top surfaces. Besides, TCs of the side surfaces (TC.10 and TC.11) had the minimum temperatures during the process. These surfaces, due to their relative positions in the furnace, were faced with adjacent forged blocks instead of furnace walls or burners; i.e., they had limitations regarding any direct thermal radiation from the furnace and due to the small gap between the blocks, they had relatively smaller radiation view factors from the furnace parts. Fig. 4.3(b) also shows that among the thermocouples on the other surfaces, those that are closer to the right surface or product edges (TC.5, TC.8, and TC.9) had higher values. The edge effect is also visible in Fig. 4.3(c) where it can be seen that TC.4 has relatively higher temperatures as compared with the TC.3 and TC.2 on the same surface. Another interesting finding is the relatively lower temperatures of the TC.2, which was located above the fixing bar on the right surface. Although TC.2 had a relatively short distance to the burner, in comparison with TC.4 and TC.3, it experienced lower temperatures.

Finally, the temperature differences between selected thermocouples in different faces are presented in Fig. 4.3(d). It can be seen that the maximum difference between TC.1 (on the right surface) and TC.10 (on the side surface) could reach up to 200 K. Further, this difference for TC.1-TC.6 and TC.1-TC.7 could reach up to 140 K and 120 K, respectively. Considering the previously discussed initial temperature uniformity of the unloaded furnace

at different temperatures, the observed non-uniformity could be correlated to the presence of the forged ingots. Therefore, the transient heating history should be analyzed by considering both convection and radiation heat transfer modes.

4.4.2 CFD Analysis

To comprehensively analyze the heating patterns, temperature non-uniformities and the share of each heat transfer mode during the heat treatment process, CFD simulations results are discussed in this section.

4.4.2.1 Validation

Table 2 shows the distribution of the available heat in different parts of the furnace, obtained from the CFD analysis. The furnace efficiency was defined by the ratio of the net heat received by the forged blocks and the available heat input to the furnace (78 GJ) as follows (B Mayr, Prieler, Demuth, Moderer, et al., 2017):

$$\eta_{furnace} = \frac{Q_{ingot}}{Q_{available}} \tag{4.9}$$

Based on the measurements made on the gas flow meters installed on the furnace, furnace efficiency was estimated to be 36.6%, while the CFD simulation predicted a value of 40.1%, which are quite close considering the large size of the furnace. The observed difference is probably due to a combination of factors such as air leakage into the furnace and difference in the exact location of the TCs between the experimental and modeled conditions, which cannot be really predicted by the model.

Table 4.2 Predicted heat distribution within the furnace.

Item	Ingots	Walls	Flue Gas	Fixing Bars	Other
Absorbed/lost heat (GJ)	28.08	7.65	25.74	9.2	5.42

Results of the numerically predicted and experimentally measured temperatures at different locations of the block are presented in Fig. 4.4(a). The CFD model predicts the temperature evolution fairly well with a maximum deviation of about 7%, which is mostly related to the initial heating stage. As mentioned above, the differences between the experimental and simulation results are reasonable considering the large dimensions of the furnace and the blocks. Although some over-predictions can be observed for the surface temperatures, Fig. 4. 4(a) shows that the simulation results are valid and further investigation can be carried out using the present CFD model. Therefore, models such as standard k-ε with a relatively lower computational cost in comparison with the more complex ones (such as the RSM turbulence model) can be employed effectively in this application for furthered detailed studies or optimization purposes. Nonetheless, employment of more sophisticated models such as RSM and their related boundary conditions for turbulence modeling or increasing the mesh size could result in better accuracy. Also, increasing the number of control angles in the angular discretization of the DO model could result in more accurate predictions of the local thermal radiation, where strong variations of spatial temperatures exist (i.e., the burner area). However, these recommendations will add to the computational costs in the solution procedure and therefore, computational cost/benefit analysis needs to be carried out on a case by case basis.

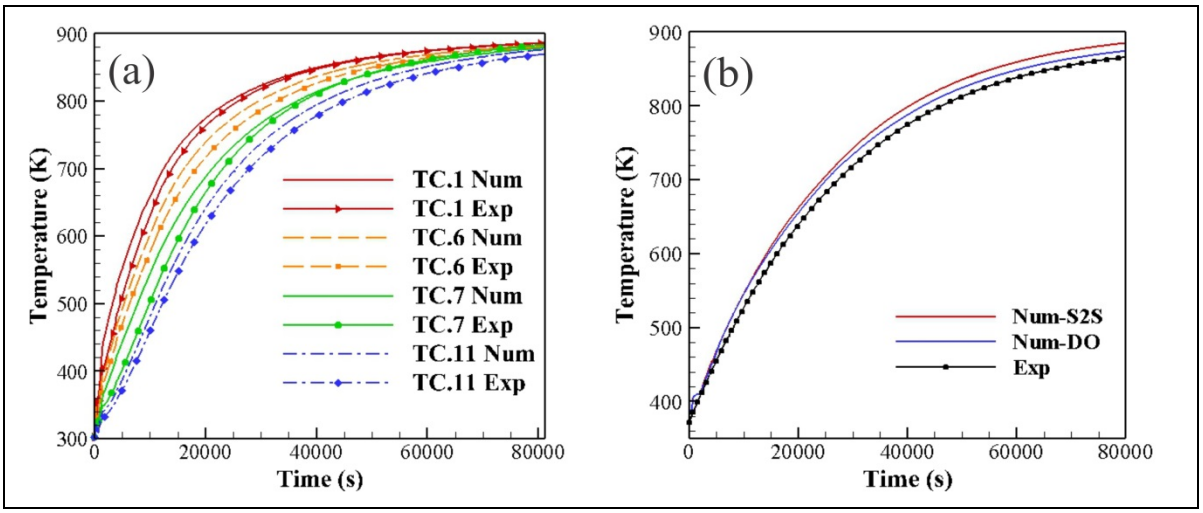

Figure 4.4 Comparison between numerically predicted and measured temperatures of the workpiece.

Radiation view factor of the workpiece surfaces and participating medium are the two main active parameters for the analysis of the radiation heat transfer, in the present application. The influence of participating medium on the final temperature history was evaluated using the S2S model and the results are reported in Fig. 4.4(b). It can be seen that, neglecting the effect of combustion products participation in the absorbed radiation of the workpiece, characteristic of the S2S model, produces about 1.5% over prediction in comparison to the DO model. Thus, although DO model provides more accurate predictions, S2S model with lower computational cost, can be effectively used in this application. Furthermore, because 98.5% of radiation heat transfer is controlled by the radiation view factor of the surfaces, loading pattern optimization for this type of furnaces can be done only by view factor optimization when the radiative heat transfer is considered.

4.4.2.2 Analysis of the heating process of the loaded furnace

Transient contours of temperature evolution of the loaded furnace (in an x-y plane) and ingot surfaces during the heating process are depicted in Fig. 4.5. The simulation results clearly confirm a non-uniform temperature distribution during the heating process as observed during the experimental phase (Fig. 4.3). Ingot transient temperature history shows that the side surfaces have relatively lower temperatures in comparison with the other surfaces. Gradual heating from the right surface to the left and top surfaces and finally side surfaces is evident. A maximum temperature difference of about 262 K exists from one side of the product to the other.

Results of furnace heating history show that the temperature of the furnace starts increasing from regions close to the burners, and then gradually extends to the center. Similarly, an increase in temperature begins rapidly on the right side of the block where the lower burners are located; while the left and side surfaces are heated latterly. Results also indicate that the fluid in the vicinity of the left surface and the top surface was also heated with delay in comparison with the right surface where the lower part of the right surface hindered the fluid

flow circulation (Fig. 4.5(e)). These findings further confirm the results reported in experimental measurements.

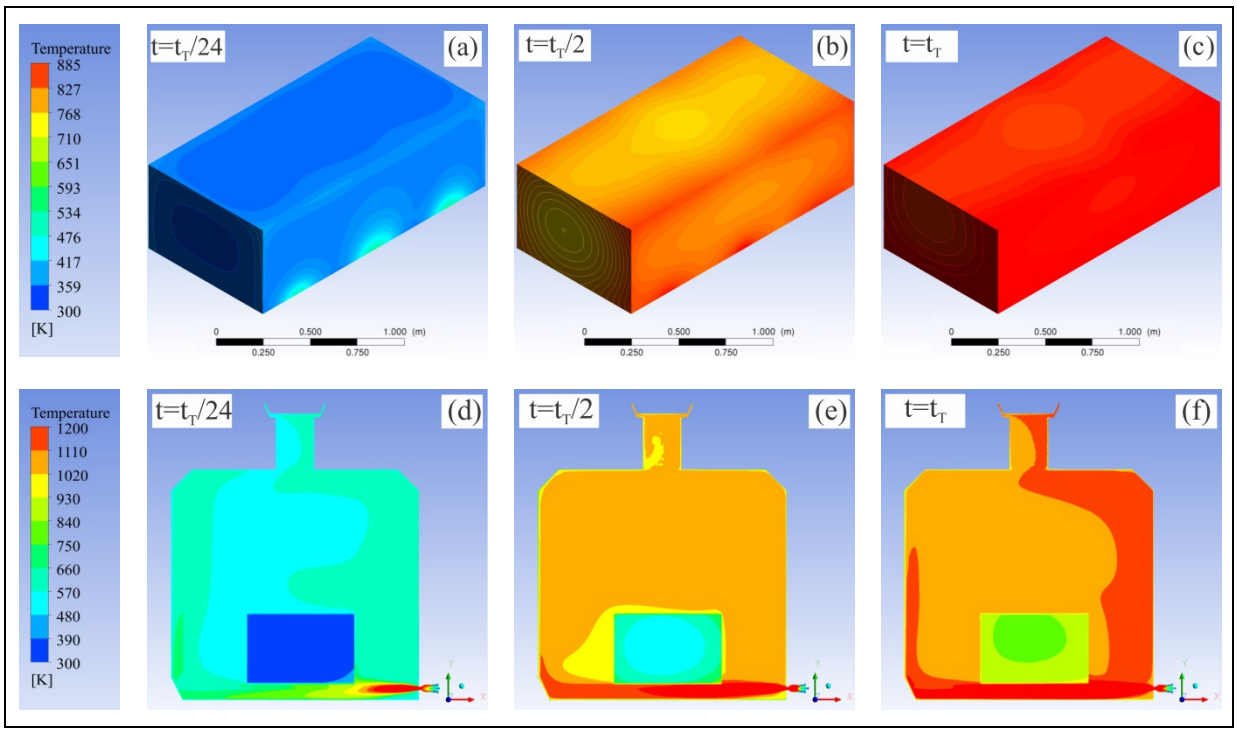

Figure 4.5 Transient contours of temperature evolution of the forged ingot surfaces and furnace central cross section in 2D and 3D views, respectively.

Fig. 4.6 shows the transient history of average total heat flux, average radiation heat flux and average surface heat transfer coefficient on the right, left and side surfaces of the workpiece during the heat treatment process. A considerable difference between the total heat flux rates in the first period of the process is revealed, which is in direct relation to the identified non-uniformities (see Figs. 4.3 and 4.4). Both radiation and convection heat transfers modes show the same identified differences in their transient histories. However, as it can be seen, the right surface due to the high velocity of burner product, is mainly heated by the convection heat transfer at the beginning of the process, while for the left surface, radiation heat transfer plays the most important role due to the blockage of the fluid flow by the workpiece. The results indicate that heat transfer coefficient in the first part of the process for the side surface is less than those on the right and left surfaces and in the peak zone its value is 0.32 of the

one for the right surface. On the other hand, the radiation heat flux at this surface in the first period of the process was about 12% and 17% of the left and the right surfaces fluxes, respectively. Due to the small gap between the blocks, side surfaces have lower radiation view factors and convection heat transfer coefficients. Therefore, the loading effect by reducing both heat transfer modes (mainly the radiation heat flux) affects the temperature history of the side surface, whilst for the right and left ones it mainly changes the heat transfer modes and heating pattern.

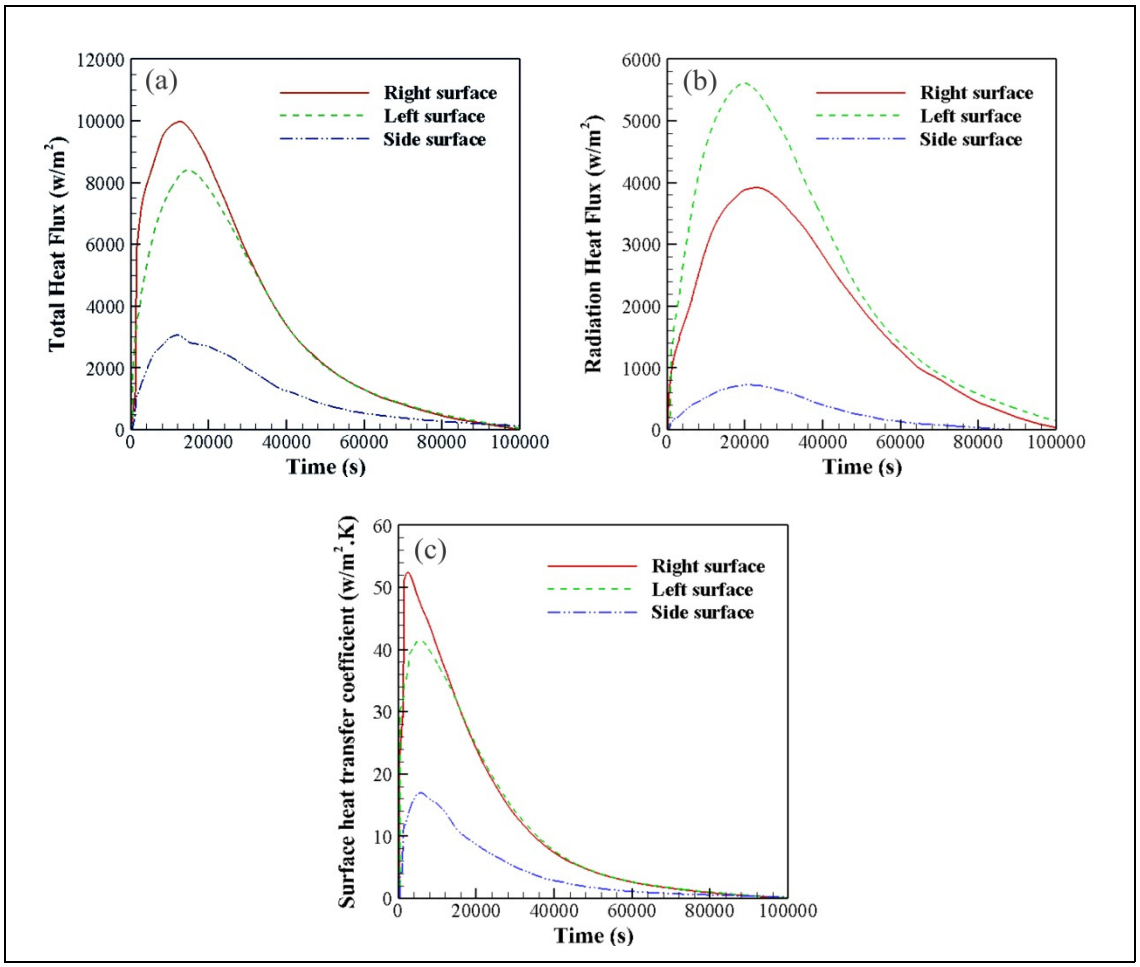

Figure 4.6 Transient history of a) total heat flux, b) radiation heat flux, and c) heat transfer coefficient for different surfaces.

Local temperature distributions (contours) on the right surface and the bottom surface of the forged ingot are presented in Fig. 4.7. Three significant temperature gradients (red regions),

equal to the number of burners facing the block, are observed. The high temperature region in the middle of the right surface (Fig. 4.7(a)) has higher temperatures in comparison to the side ones. This could be due to the fact that the side surfaces are affected by gaps between the blocks. High temperatures are also visible near the edges of this surface as shown in Fig. 4.7(a). Usually, the temperature on the edges is higher relative to the other points due to more radiative heat flux in these regions (more surfaces to absorb radiation from furnace walls and combustion products (B Mayr, Prieler, Demuth, Moderer, et al., 2017)). However, the results indicate that the edge effect on the temperature distribution of the right surface is not as strong as the burner effect. The temperature gradient on the right surface could reach up to 159 K which shows the importance of burner locations inside the heat treatment furnaces.

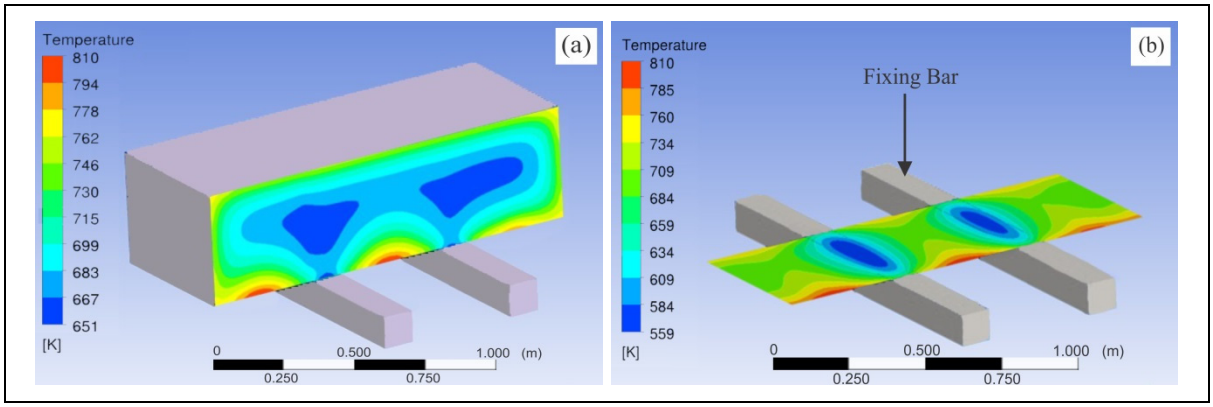

Figure 4.7 Contours of temperature distribution on a) right surface, and b) bottom surface of the forged ingot at $t = t_T/6$.

The effect of the fixing bars on temperature distribution of the product is illustrated in Fig. 4.7(b). Two blue colored areas near to the fixing bars at the right surface confirm the measured temperature of the TC.2 in Fig. 4.3. In addition, Fixing bars covering part of the bottom surface prevent the active radiation and convection heat transfer of the furnace (i.e., these areas are heated by conduction only). The shadow effect of the fixing bars can also have a major effect on temperature distribution inside the forged block. A combination of burner's effect (higher temperatures) and fixing bars shadows (lower temperatures) on the bottom surface is probably the origin of the significant thermal gradient on this surface (up to 251 K). Therefore, the geometrical effect of the furnace such as burner's location and the

position of the fixing bars should be carefully taken into account for an accurate and reliable analysis of the heat treatment within large size furnaces.

4.4.2.3 Analysis of fluid flow structures

The local convection heat transfer to the forged ingot in the context of objects facing with flow stream, called as bluff body, should also be analyzed based on the formation of flow structures (also called as vortical structures or vortices) around the object (Ničeno, Dronkers, & Hanjalić, 2002). It should be noted that the formation of vortical structures around can cause non-uniform temperature distributions on the forged block surfaces (Ničeno et al., 2002). Vortical structures are characterized by different parameters such as size, scale, shape, velocity, vorticity and energy. It has been reported that one of the main characteristics of the vortical structures is the formation of coherent circulation in parts of the flow field (Hussain, 1983). Therefore, fluid flow circulation inside the furnace is visualized in Fig. 4.8, using time-averaged streamlines at x-y planes. Streamlines show a blockage of fluid flow by the load in the impingement zone (creation of stagnation point) and the formation of a wake region in the downstream (existence of a wake vortex in the vicinity of the left surface). This behavior can be seen in the formation of vortical structure around a typical bluff body (Ničeno et al., 2002). Fig. 4.8 shows that there is a clockwise circulation of fluid flow inside the furnace at each section, which is in correlation with the heating trend in the furnace. Fig. 4.8 also, shows the presence of a strong vortex at the center of the furnace in both planes (perpendicular to the lower burner and between fixing bars). Further, a detachment of fluid from the block near the left side of the top surface and the upper side of the left surface is clear. The coexistence of wake vortices and detachment of fluid near the left surface of the forged ingot and the presence of a cold area in this zone shows the interrelation between the convection heating pattern and the fluid flow structures inside the furnace. A similar behavior can also be observed on the top surface and its adjacent vortex. Moreover, creation of a small vortex near the right surface where the burner products faced directly with the forged ingot surface (stagnation point) also indicates the interrelation between forged ingot heating and the vortical structures. Therefore, tracking the vortical structures within the furnace should be

considered as an important parameter for the process optimization and multiple loading scenarios. The effect of these structures is expected to be more significant at lower temperatures, where the convective heat transfer mode could dominate the radiation one and the maximum non-uniformity identified.

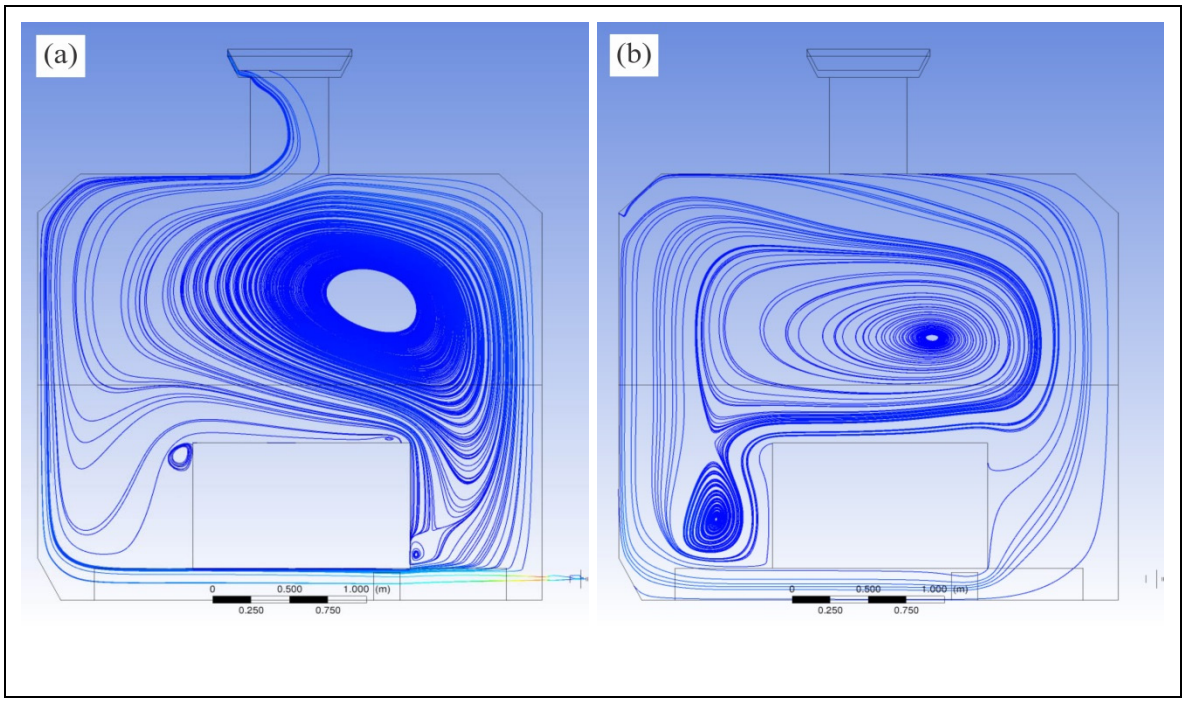

Figure 4.8 Streamlines of planes at a) between fixing bars and perpendicular to down burner face and b) center of fixing bars.

4.4.2.4 Assessment of heating process inside the large size forgings

Investigation of the temperature distribution inside the block can help to quantify the impact of the non-uniform heating of the surfaces on the temperature evolution inside the forging. It can be seen in Fig. 4.9 that the central planes also affected by non-uniform heating of the surface and the same pattern of heating from the bottom and right side of the forged block to the left, top and finally side surfaces is visible inside the workpiece. Cold area is mainly extended longitudinally between two side surfaces. Fig. 4.9(c) also shows that the coldest point in the lateral plane is actually not located at the center of the forged block and shifted toward the left and top surfaces. The results clearly demonstrate that product loading,

geometrical parameters and fluid flow circulation around the forged block influence the heating pattern inside the product. However, the strength of the above-mentioned parameters is more visible on the surface temperature distribution, as compared with the inside of the workpiece. Generally, it is assumed that the differentiation in the mechanical properties of the forged ingot mainly varies as a function of the distance from the surface. However, considering the temperature gradient from one side to the other and different temperatures at the same depth of the forged block, the above assessment should be relativized and a more precise approach should consider the heating pattern and its directions.

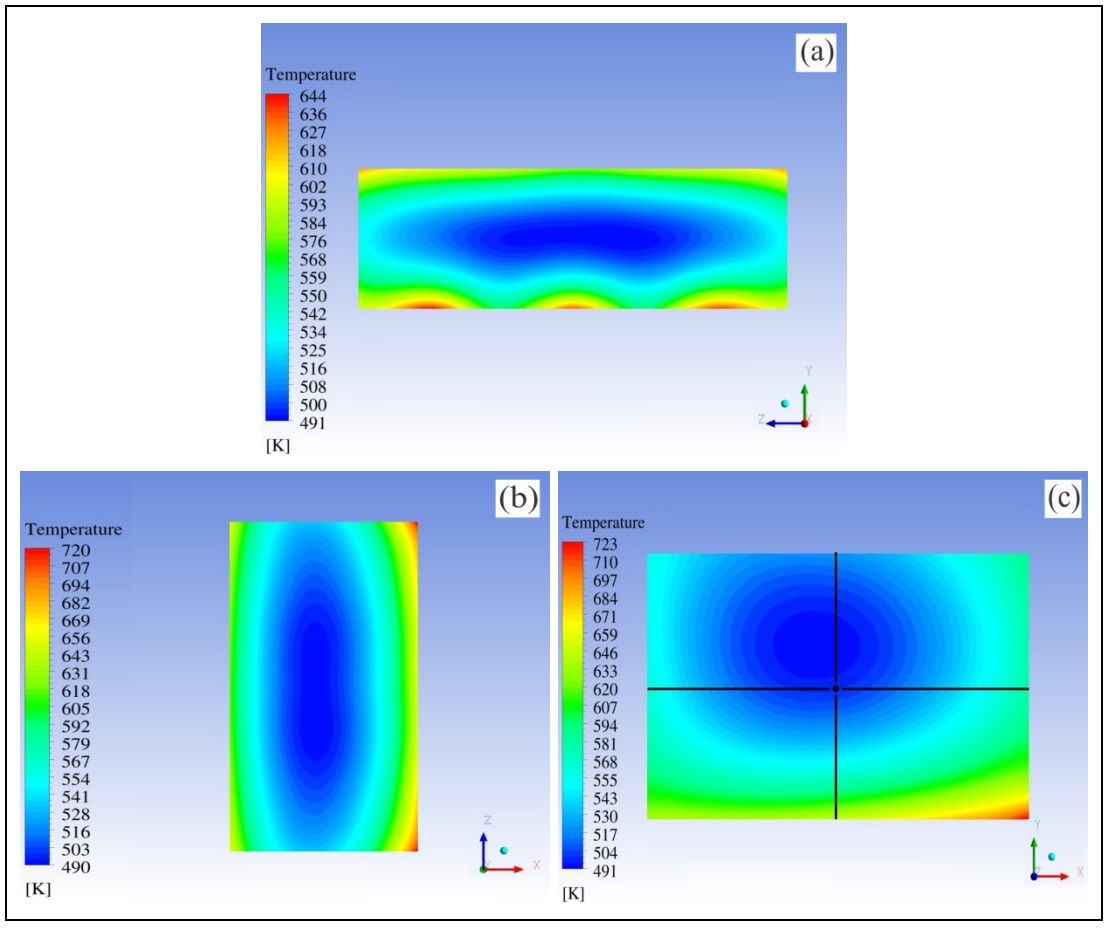

Figure 4.9 Temperature contours of cross-sectional planes at the center of the forged ingot in: (a) longitudinal, (b) transversal and (c) lateral planes at $t = t_T/6$.

4.5 Conclusions

Comprehensive analysis of heat transfer in the heat treatment process of forged blocks in a large size gas-fired heat treatment furnace was investigated in the present work. Experimental temperature measurement and unsteady CFD simulations were employed for simultaneous analysis of fluid flow interactions inside the furnace including turbulent combustion, fluid flow structures and also conjugate heat transfer during the heating. Concluding remarks are summarized as follows:

1. The developed 3D CFD model provided good agreement with experimentally measured data.

2. Both DO and S2S radiation models could be reliably used for this application. An over-prediction of less than 2% was predicted when using the S2S model in comparison with the DO model, which indicates that the computationally effective S2S model can be employed for this type of gas-fired heat treatment furnaces. The analysis of the results also showed that radiation view factor has a higher contribution than participating medium when analyzing radiation heat transfer during heat treatment of large size components.

3. Analysis of experimental temperature measurements showed that the unloaded furnace domain was uniform during the test. However, after loading, temperature non-uniformities, up to 200 K, were found during the heating process, which could affect microstructure evolution.

4. The influence of geometrical effects such as burner locations and fixing bars as sources for temperature non-uniformities must be taken into consideration for optimizing the heat treatment process of large size components.

5. The formation of vortical structures in the turbulent flow field results in significant changes in the convection heat transfer of the affected area, which demonstrates the

interrelation between the heating pattern and the fluid flow structures inside the furnace.

6. The developed CFD model was validated using experimental measurements. The obtained data could be directly applied for the optimization of the operational conditions and loading patterns of large size gas-fired heat treatment furnaces.

CHAPTER 5

THERMAL ANALYSIS OF FURNACE RESIDENCE TIME AND LOADING PATTERN DURING HEAT TREATMENT OF LARGE SIZE FORGINGS

Nima Bohlooli Arkhazloo[a,*], Farzad Bazdidi-Tehrani[b], Jean-Benoît Morin[c] and Mohammad Jahazi[a]

[a] Département de Génie Mécanique, École de Technologie Supérieure, Montréal, H3C 1K3, Canada

[b] School of Mechanical Engineering, Iran University of Science and Technology, Tehran, 16846-13114, Iran

[c] Finkl Steel Inc., 100 McCarthy, Saint-Joseph-de-Sorel, QC J3R 3M8, Canada,

Paper submitted to *Journal of Materials Processing Technology,* In December 2019*,*

Abstract

A combination of unsteady 3D CFD simulations and experimental temperature measurements was employed to determine the effect of loading patterns on the temperature distribution within large size heavy steel forgings inside a gas-fired heat treatment furnace. This was aimed to obtain a more homogenous temperature distribution. Besides, a hybrid methodology using 3D numerical simulations and a high resolution dilatometer allowed improving residence time of forgings inside the heat treatment furnace. The influence of the loading patterns and skids on temperature distribution and residence time of forgings was examined using four different loading patterns. Comprehensive unsteady thermal analysis of the products heating allowed quantifying the impact of skids usage and their dimensions on the extent of the uniformity of temperature distribution. The results were interpreted in terms of the inter-relationship between the skids usage, their geometry, absorbed radiation and convective heat fluxes. The analysis showed that temperature non-uniformities of up to 331K could be produced for non-optimum loading patterns. Using the developed CFD approach it was possible to reduce the temperature non-uniformity of different sizes of blocks up to 32% via changing the loading pattern inside the furnace. Further, the large size slab's residence

time was improved by almost 15.5% when employing the proposed hybrid approach. This approach could directly be applied to the optimization of different heat treatment cycles of large size forgings.

Keywords: Thermal analysis, Loading pattern, Temperature uniformity, Residence time, Hybrid approach, Experimental measurements, Numerical simulation

Nomenclature

Latin symbols

a	Absorption coefficient
d	Characteristic dimension (m)
E	Energy (J)
g	Gravity (m/s^2)
J_i^z	Diffusive flux of chemical species
h	Enthalpy (J/ kg)
k	Turbulence kinetic energy (m^2/s^2)
k_{eff}	Effective thermal conductivity
p	Pressure (Pa)
R_z	Production rate of z_{th} component
$R_{z,r}$	Production rate of z_{th} component
S_z	Source term of z_{th} component production
Sc	Schmidt number
m^{g}	Mass flux ($kg/\mathrm{m}^2.s$)
q_s	The generic source term
Re	Reynolds number (ud/ν)
t	Time (s)
T	Temperature (K)

t_T	Total heat treatment time
u_i	Reynolds-averaged velocity in tensor notation
u_i'	Resolved fluctuating velocity components
Y	Mass fraction of species
x, y, z	Direction of coordinate axes

Greek symbols

ε	Turbulence dissipation rate (m^2 / s^3)
τ_{ij}	Viscous stress tensor
ν	Kinematic Viscosity (m^2 / s)
μ_t	Turbulence eddy viscosity ($kg.m / s$)
ρ	Density (kg / m^3)
$\rho\overline{u_i' u_j'}$	Reynolds stress ($kg / \mathrm{m}.s^2$)

Superscripts

'	Fluctuations with respect to a Reynolds averaging

Subscripts

i, j, k	Tonsorial indices tensor
z	z_{th} species

Abbreviation

3D	Three dimensional
CFD	Computational Fluid Dynamics
DO	Discrete ordinates model
DSK	Double Skid
DSKC	Double skid + Central spacer skid
HRC	Rockwell C hardness

SK	Single Skid
SKC	Single Skid + Central spacer skid
RTE	Radiative transport equation

5.1 Introduction

Gas-fired furnaces are extensively used in the steel industry in the heat treatment process. Specifically, in the case of heavy forgings made of high strength steels, a heat treatment process called Quench and Temper (Q&T) is used to obtain the desired mechanical properties (e.g., hardness). The Q&T process is carried out in two steps: initially the parts are heated to a certain temperature and hold for a period of time before being quenched in water. In the second step (tempering) the parts are heated to a lower temperature (non-isothermal tempering) and kept for a period of time (isothermal tempering) before being air cooled. It is of paramount importance to ensure a high quality heat treatment operation as major microstructural changes (grain refinement, phase transformation, etc.) take place at this stage which have a determining effect on the final mechanical properties (Canale et al., 2008; Kang & Rong, 2006). According to the literature final mechanical properties and microstructural features are affected significantly by tempering temperature and holding time inside the furnace (Janjušević, Gulišija, Mihailović, & Patarić, 2009). Therefore, uniformity of the heating process, in other words, the temperature distribution's uniformity during the non-isothermal tempering up to the target temperature is of great importance for the quality of final products (Gao et al., 2000; B. Wu, Arnold, Arnold, Downey, & Zhou, 2007) specifically for the large-size products (Bohlooli Arkhazloo et al., 2019; Gur & Pan, 2008). However, considering that parts, are rarely single loaded in the furnace, their loading pattern (e.g., distances between the parts, stacking mode, etc.) as well as furnace geometry (burners' and skids' positions), will influence temperature evolution within their volume resulting in non-uniform temperature distribution that may affect the final properties. The possible use of longer holding times is not a viable solution as it will bring other microstructural damages and is not energy friendly (Hao et al., 2008). Hence, predicting, controlling and consequently optimizing the heating process or the transient temperature of the part as a function of the furnace temperature and the related thermal interactions and subsequently possible reduction

in the tempering process time, is a necessary task for energy saving and quality control (Hao et al., 2008).

However, an exact prediction of the furnace temperature distribution and, consequently, the temperature experienced by the product would require a more fundamental understanding of the interactions between heat transfer parameters, process parameters and parts configurations within the furnace. At the present time such data in thermal analysis of large size products heating characteristics is not available and therefore often empirical correlations are used to estimate the heat treatment cycle parameters (Kang & Rong, 2006). These correlations are usually defined as a function of the total furnace load and selected loading patterns of the parts inside the furnace (Korad et al., 2013). Hence, they show large deviations in the case of multiple loadings and complex furnace configurations (Hao et al., 2008). On the other hand, in most of the studies and evaluations in the field of metallurgy (Cheng et al., 1988; Primig & Leitner, 2011; Talebi et al., 2017), the non-isothermal tempering procedure was simplified assuming a constant heating rates rather than a variable one which is actually experienced by the products in the real production cycle. The problem is more acute in the case of large size products (that encompass high temperature gradient from one end to another) at high temperatures due to operational difficulties and high costs of experimentation. Therefore, employing a constant temperature and time in the correlations such as Hollomon-Jaffe (Janjušević et al., 2009) may result in deviation from what is really experienced by the large size forgings during the whole tempering process.

While both analytical and numerical methods could be used to study the problem, limitations of analytical methods in solving coupled non-linear phenomena (i.e., turbulent combustion along with conjugate heat transfer and fluid flow) do not allow their effective use in these cases (Chapman et al., 1990; Gao et al., 2000). Computational fluid dynamics (CFD) comprising various numerical methods has become in recent years a very cost effective and reliable technique to study the thermal interactions inside the heat treatment furnaces. Several studies such as those of Wang et al.(J. Wang et al., 2008), Hao et al. (Hao et al., 2008), Kang and Rong (Kang & Rong, 2006) and Defaee et al. (Rad, Ashrafizadeh, & Nickaeen, 2017)

employing CFD, investigated flow and heat distributions inside electrically heated, gas quenching and hot air treating furnaces.

Due to the complexity of the reactive flow analysis inside the gas-fired furnaces, the long operating time of the heat treatment process and the totally transient conditions of the process, little information is available regarding the transient studies of the real-scale gas-fired heat treatment furnaces. The existing studies have been focused either on small- to medium-scale gas-fired furnaces (Galletti et al., 2013) or simplified steady-state simulations (Danon et al., 2011; García et al., 2019; B. Mayr, Prieler, Demuth, Moderer, et al., 2017; Prieler, Demuth, Spoljaric, & Hochenauer, 2015; Prieler et al., 2016). For instance, Yang et al. (Yang et al., 2007) studied the performance of small-scale mobile heat treatment furnaces and Prieler et al. (Prieler, Mayr, et al., 2015) and Mayr et al. (B Mayr, Prieler, Demuth, Potesser, et al., 2017) investigated the oxy fired laboratory-scale and semi-industrial gas-fired furnaces heat distribution in a single loading configuration using steady-state assumption, respectively.

Recently, Bohlooli et al. (Bohlooli Arkhazloo et al., 2019) reported on the experimental and numerical analyses of the heating process of large size forged ingots inside a gas-fired furnace. Comprehensive experimental analysis of instrumented large size ingot and gas-fired furnace temperature's history proved that large-scale products can affect the furnace temperature's uniformity and consequently products' heating uniformity. A full-scale three-dimensional (3D) model of the process revealed that the identified non-uniform heating of the large-scale products had a relationship with the fluid flow structure, geometrical parameters of the furnace (including burner locations) and loading patterns of ingots (including their relative locations and distances). The effect of vortical structures and loading pattern on the heat treatment process and temperature history of small scale products had been mentioned in the numerical study of Wang and Shang (Z. J. Wang & Shang, 2010) who investigated the flow and heat exchange in the high-pressure gas quenching chamber. Macchion et al (Macchion, Zahrai, & Bouwman, 2005) Kang and Rong (Kang & Rong, 2006) and Korad et al. (Korad et al., 2013) also analyzed the loading pattern's effect on the

heating and cooling rates of products in different furnaces. Concentrating on the metallurgical aspects and toward reducing the process cost, the steady state CFD simulations of indirect fired homogenization furnace (used for aluminum billet treatment) in Korad et al.'s (Korad et al., 2013) study showed that different billets stacked in the furnace experienced different temperature distributions (temperature non-uniformity) as a result of loading pattern inside the furnace during the non-isothermal tempering. Macchion et al. (Macchion et al., 2004) in a CFD simulation of gas quenching chamber of small parts pointed out that the position of parts inside the furnace could significantly affect the temperature uniformity of products during the heat treatment furnaces. Also, Kang and Rong (Kang & Rong, 2006) using CFD simulations investigated the heating history (non-isothermal tempering) of two different loading patterns of small size parts inside an electrically heated furnace. Their study revealed that the loading pattern even in small size products could change the heating history of the parts and furnace performance. However, up to now, little data is available on the interactions between heat transfer parameters, stacking strategy, heat treatment process variables (specifically temperature uniformity and heating time in non-isothermal tempering) in relation to loading pattern of large size forgings inside gas-fired furnaces. Besides, most of the studies investigating the effect of constant heating rates (rather than a series of a variable heating rates resulting in real temperature history experienced by the products inside the furnace) and subsequent certain holding times on the mechanical properties of the steels (Ray, Ganguly, & Panda, 2003; Revilla, López, & Rodriguez-Ibabe, 2014; Talebi et al., 2017; B. B. Wu, Chen, Shang, Xie, & Misra, 2019; Zou, Ying, Zhang, & Fang, 2010). Simultaneous analysis of isothermal and non-isothermal tempering history of large size forgings inside gas-fired furnaces in order to reduce the residence time of the products has not been addressed in the literature.

The present paper reports on an investigation aiming to address the above challenges using 3D CFD modeling complemented with experimental validation. Four possible loading patterns of heavy forgings in a gas-fired furnace were analyzed. This is not only aimed to have maximum temperature distribution's uniformity and similar heating rates, but also to reduce the time to reach the target temperature during the non-isothermal tempering stage.

Besides, a hybrid methodology combining 3D CFD numerical predictions and high resolution dilatometer machine was introduced and used to further reduce the residence time of the forgings during the isothermal tempering based on the real-life temperature experience of steel parts in the large-size gas-fired furnaces.

5.2 Loading Patterns

The studied furnace was a 3.05× 3.28 × 8.83 (m^3) batch type gas-fired furnace. The furnace was heated by 18 high-velocity cup burners (Baukal Jr, 2003) including 9 upper burners (located on the uppers section of the furnace left wall) and 9 lower burners (installed in the lower section of the furnace right wall). Fig. 5.1 illustrates the furnace and four different loading patterns used for the CFD simulations (See also Fig. 5.3). A total weight of 130 metric tons, corresponding to the loading capacity of a large size furnace, was fixed in all the four patterns. Two types of forgings, called large size block and slab, with dimensions of 1.4 × 0.89 ×2.72 (m^3) and 1.1×0.5×2.25 (m^3), were used in different configurations. Blocks were mounted on oxidized steel skids in car-bottom furnace. The following denominations were used to characterize each of the four configurations:

Single Skid (SK): A combination of one large size block and one slab stacked on its top.

DSK (Double skid): The second case study was used to see the effect of double height skids in the gas-fired furnaces. According to the Bohlooli et al. (Bohlooli Arkhazloo et al., 2019), lower burners in the furnace are one of the main root causes of non-uniform temperature distributions. Therefore, this simulation will allow quantifying the impact of the skid height.

SKC (Single skid + Central spacer): The third case study was aimed to evaluate the effect of spacing skids (made of steel with an oxidized surface) on the stacking patterns and subsequent uniformity and residence time of blocks in the heat treatment

furnaces. Two sizes of spacers with the cross-sectional dimensions of 0.254×0.245 (m^2) and 0.127×0.127 (m^2) were used.

DSKC (Double skid + Central spacer skid): A combination of double skids at the bottom and center spacers between the large block and the slab was the fourth loading pattern used for the simulations.

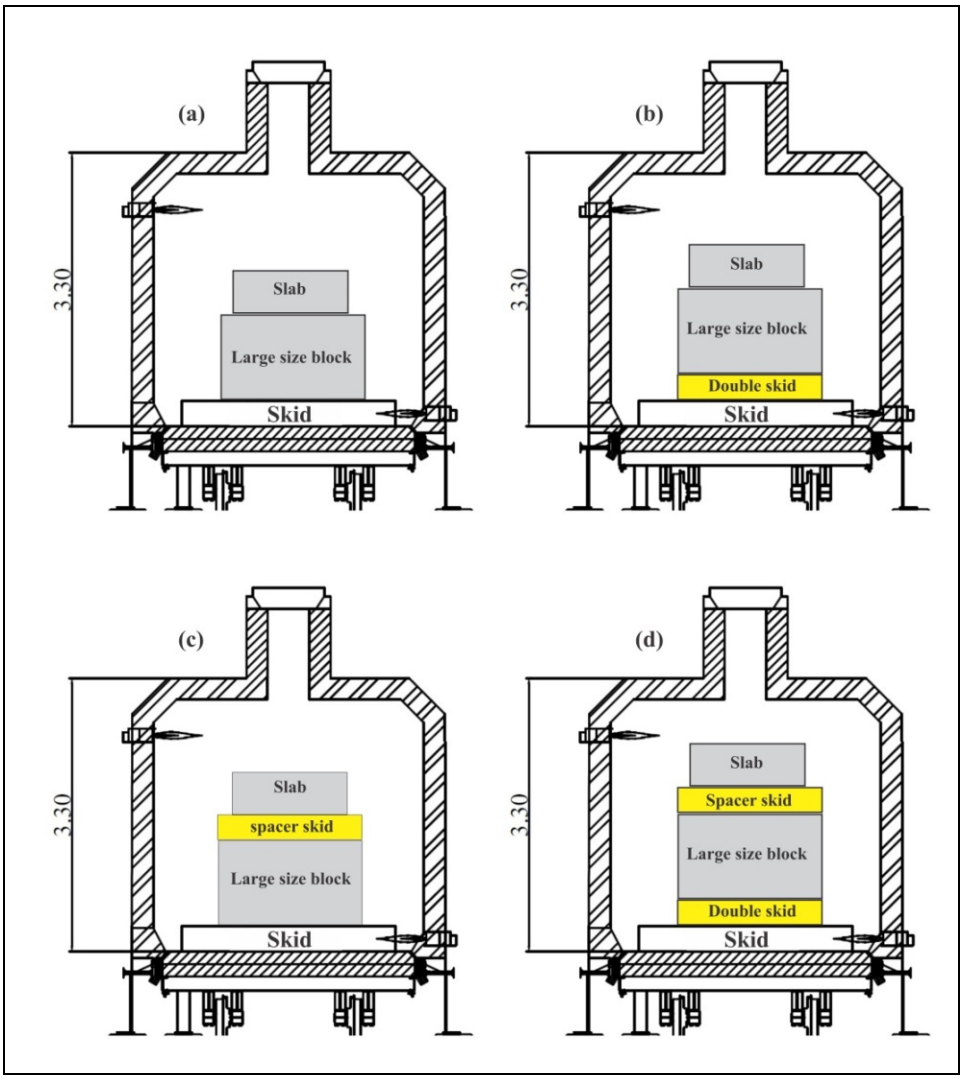

Figure 5.1 Four different loading patterns of forgings using skids inside gas-fired heat treatment furnace: a) SK, b) DSK, c) SKC and d) DSKC.

5.3 Methodology

5.3.1 Computational Details

The previously developed and validated CFD model in the authors' study (Bohlooli Arkhazloo et al., 2019) was employed as the basis for the numerical simulation. The transient CFD simulations employing a pressure-based solver were carried out using the finite-volume based ANSYS-FLUENT software (ANSYS, 2016) to solve the Reynolds-averaged Navier-Stokes (RANS) equations, as follows (ANSYS, 2016).

$$\frac{\partial \rho}{\partial t}+\frac{\partial}{\partial x_i}(\rho u_i)=0 \tag{5.1}$$

$$\frac{\partial}{\partial t}(\rho u_i)+\frac{\partial}{\partial x_j}(\rho u_i u_j)=-\frac{\partial p}{\partial x_i}+\frac{\partial \tau_{ij}}{\partial x_j}-\frac{\partial}{\partial x_i}(\rho\overline{u_i' u_j'})+F \tag{5.2}$$

$$\frac{\partial}{\partial t}(\rho E)+\frac{\partial}{\partial x_j}(\rho u_i h)+\frac{\partial}{\partial x_j}(u_i p)=\frac{\partial}{\partial x_i}(\mathrm{k}_{eff}\frac{\partial T}{\partial x_i}-\sum_{z=1}^{n} h_z \overset{\mathrm{r}}{J}_z+u_i\tau_{ij})-\frac{\partial}{\partial x_j}(\overline{\rho u_i' h_s'})+q_s \tag{5.3}$$

where, the stress tensor, τ_{ij}, in the above momentum and energy equations (Eq. 5.2 and Eq. 5.3, respectively) is given by:

$$\tau_{ij}=\left[\mu\left(\frac{\partial u_i}{\partial x_j}+\frac{\partial u_j}{\partial x_i}\right)\right]-\frac{2}{3}\mu\frac{\partial u_l}{\partial x_l}\delta_{ij} \tag{5.4}$$

and the diffusive flux of combustion product species (in Eq. 5.2) is defined by the Fick's law:

$$\partial \overset{\mathrm{r}}{J}_z=-\frac{\mu_t}{Sc_k}\frac{\partial Y_z}{\partial x_i} \tag{5.5}$$

The turbulent combustion and fluid flow were simulated using the standard $k-\varepsilon$ turbulence model proposed by Spalding (Spalding, 1971). It must be noted that, the above model has already been applied to gas-fired furnaces and its reliability had been approved (Ishii et al., 2002; Y. Liu et al., 2014). Due to the high velocity of the combustion products coming from the burner outlet, Arrhenius chemical kinetic calculations were not taken into account and the eddy dissipation model (EDM) (B. F. Magnussen & Hjertager, 1977) was used to simulate

the combustion phenomenon. In this model, assuming that the reaction rates are dominated by the turbulence, the species transport formulation (Eq. 5.6) for the local mass fraction species (Y_z) is solved (ANSYS, 2016).

$$\frac{\partial}{\partial t}(\rho Y_z) + \nabla.(\rho \bar{v} Y_z) = -\nabla.\overline{J_z} + \dot{R}_z + \dot{S}_z \tag{5.6}$$

where, $\dot{R}_z$ represents the net production rate of the z_{th} component. The unsteady SIMPLE algorithm (Henk Kaarle Versteeg & Malalasekera, 2007) was applied for pressure-velocity coupling in a computational domain including 15,155,000 hexahedral non-uniform grids, as depicted in Fig. 5.2.

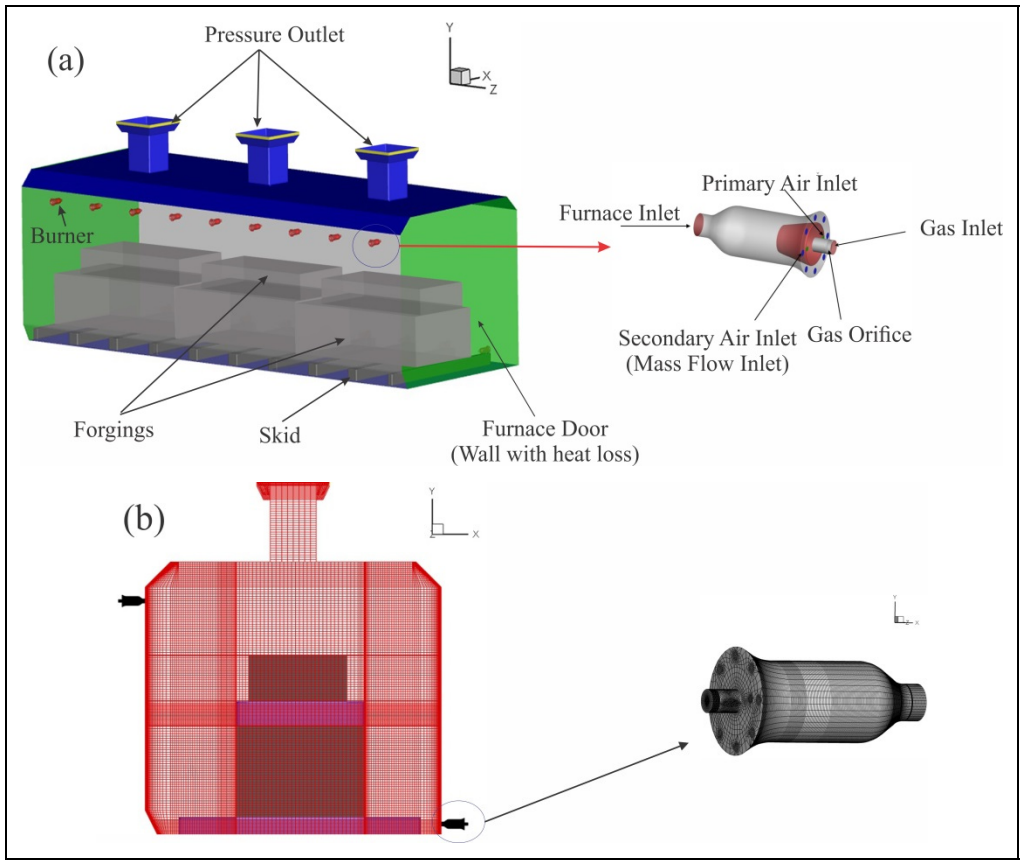

Figure 5.2 Computational domain, including: (a) boundary conditions of SK case study and (b) computational grids in SKC loading pattern.

Finer cells with low growth rate were used near the burners to resolve significant variations of the complex flow in this region (in the range of high temperature and species

concentration gradient). The grid size includes 6,408,000 non-uniform cells in the burner domains (356,000 cells in each burner). Grid independency tests were performed using two other meshes including 10,597,900 and 19,712,100 cells. The difference between results of the mesh with 15,155,000 and the fine mesh were negligible (See Fig. 5.3). Therefore the medium mesh with 15,155,000 cells was used in the simulations. Further details of the simulations procedure and boundary conditions specifications were discussed by Bohlooli et al. (Bohlooli Arkhazloo et al., 2019). The discrete ordinates model DO (Raithby & Chui, 1990) using the weighted-sum-of-gray gases model (WSGGM) (Smith et al., 1982) was also employed to solve the radiative transfer equation (RTE) considering the absorption and emission effects of the furnace medium.

5.3.2 Forgings Temperature Measurements

This part of experimentations includes temperature measurements at the surface of the forgings in the gas-fired heat treatment furnace. Measurements were conducted in a gas-fired furnace at Finkl steel-Sorel (Finkl steel Inc.). The furnace with three relatively similar zones was loaded with a total weight of 130 tons. Six K type thermocouples were embedded in different locations of the parts in the central zone of the furnace. Details regarding other characteristics of the furnace and the methods developed for reliable installation and temperature reading are provided in a recent publication by Bohlooli et al. (Bohlooli Arkhazloo et al., 2019).

5.3.3 Hybrid Approach

A hybrid methodology combining the CFD simulation results and experimental dilatometer tests was used to determine the minimum heat treatment time that is required to achieve the desired mechanical properties. Specifically, the transient temperature histories of the hottest and coldest regions of the parts were first predicted by the developed CFD model. These two points were then used as the critical points to evaluate and optimize the isothermal stage of the heat treatment cycle. This methodology includes laboratory physical simulations of the

tempering cycle during the isothermal and non-isothermal tempering (acquired through the CFD simulation) and subsequent hardness measurements of the steel for the critical points. It was started with finding the hardness of samples after applying non-isothermal tempering history of the critical points. Then several isothermal tempering were carried out to find an equivalent isothermal tempering times leading to the measured hardness in step one and desired hardness at the end of the tempering process. The difference between these two times was considered as the optimum holding time in the isothermal part of the tempering process.

The chemical composition of the investigated high-strength low-alloy steel is provided in Table 5.1. Cylindrical samples 10 mm in length and 4 mm in diameter were cut from near the surface and central zones of the slab, which had underwent open-die forging at around 1260ºC.

Table 5.1 Chemical analysis of the investigated steel - Wt. % (Finkl Steel Inc.).

Fe	C	Mn	Si	Mo	Cr	Ni	Other
Bal.	0.35	0.85	0.4	0.45	1.85	0.47	Micro-alloying

The initial tempering process of the present slabs with dimensions of 1.1×0.5×2.25 (m^3) was around 60 hours to achieve a nominal final hardness between 31-34 HRC (in the case of multiple loading). This heat treatment cycle includes a nominal 24 hours of heating stage up to 855 K (non-isothermal tempering) and 38 hours of holding at this temperature (isothermal tempering). All the heat treatment cycles applied to the parts in the furnace were physically simulated using the high-resolution TA DIL 805A/D dilatometer machine (TA instruments, New Castle, DE, USA). The heating rates using the validated CFD results were adjusted to simulate that of actual heating cycle of forgings during non-isothermal tempering. A prior austenitization process (including heating up to 870ºC, followed by 10 minutes holding at this temperature for homogenization) and subsequent cooling rate of 3ºC to produce a martensitic microstructure resembling the expected microstructure on the surface of an actual forging after water quenching (i.e., before starting the tempering process in the heat treatment furnace) was considered for the sample preparations. Dilatometry tested samples were then cut along their longitudinal axis and then polished according to standard metallography

preparation methods. Finally, Rockwell C hardness measurements were made according to ASTM E18-19 on the polished surfaces to determine the impact of the heat treatment conditions on mechanical properties. A minimum of 25 measurements with a load of 1kg and a dwell time of 10s were used.

5.4 Results and Discussion

5.4.1 Validation

Comparison between the present numerical prediction and the experimental measurement of transient temperature of the ingot at the upper surface of the large size forged block in the SK configuration is represented in Fig. 5.3. Although a slight over-prediction (maximum value of 3%) can be observed, the validity of the CFD model is therefore confirmed and further investigations could be carried.

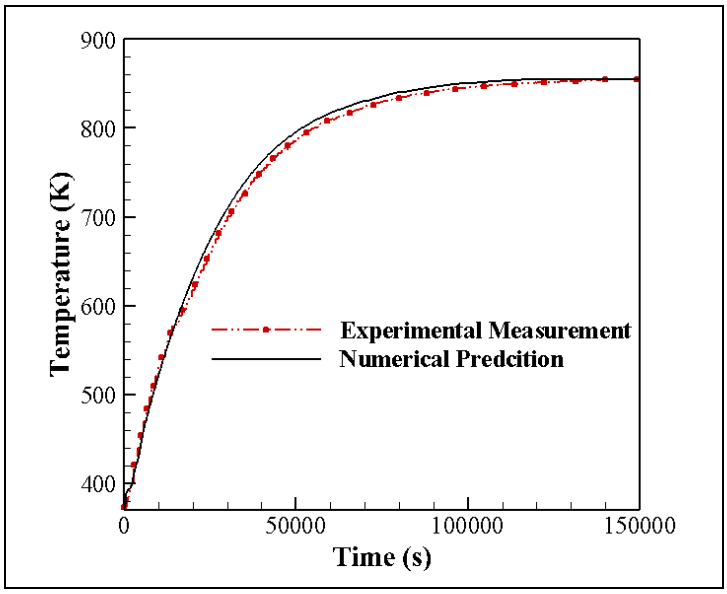

Figure 5.3 Validation of CFD simulations in fully loaded furnsce configurations.

5.4.2 Loading Pattern Analysis

Temperature evolutions of different locations of the large size forged block and the slab in the conventional SK loading pattern (first case study) are shown in Fig. 5.4. There is a considerable temperature difference between the forgings maximum temperature and the interface of the large size block and the slab, hereafter called stacking point. This point which is actually at the surface of the large block is heated after the center of the block. The difference is also observed for the slab where the stacking point at the surface of the slab has noticeably lower temperatures in comparison with the center of the block (on the contrary to the expectation of a regular heat treatment from surface to center). In this figure center modified represents the minimum temperature of the whole loadings during the heat treatment (i.e., center of the whole geometry).

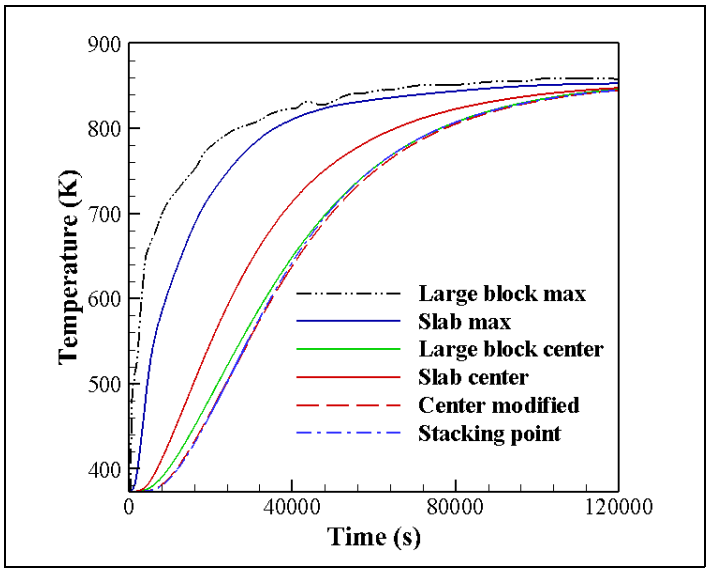

Figure 5.4 Temperature evolutions of forgings in conventional SK loading pattern.

Fig. 5.5 illustrates transient histories of maximum temperature difference (i.e., maximum non-uniformity) of the large size block and slab surfaces for the four different loading patterns.

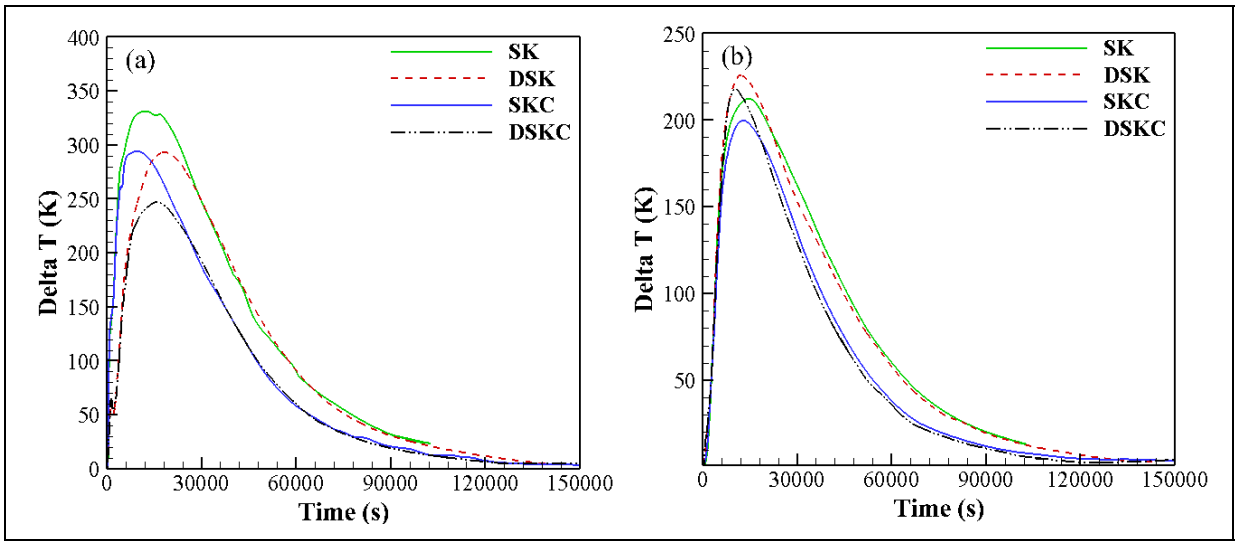

Figure 5.5 Comparison of maximum identified temperature non-uniformities for different loading patterns at the surface of: a) large size, block and b) slab.

Analysis of the data in Fig. 5.5 showed that a maximum non-uniformity of 331 K was produced in the single skid (SK) case study in the large size block. This severe non-uniformity could probably be related to the loading pattern of the blocks and geometrical parameters of the furnace including the burners' positions which were located on opposite side of the furnace close to the bottom or top of the walls (Bohlooli Arkhazloo et al., 2019). For example, the bottom right of the large block surface near the lower burners was very rapidly heated while the upper surface, intersection of the stacked slab on the large size block experienced lower heating rates and subsequently leaded to the identified non-uniformity. However, it can be seen that the use of spacers as well as double-height skids in the DSK, SKC and DSKC patterns (the second to fourth case studies) could reduce maximum non-uniformity down to 293 K, 294 K and 246 K (approximately 11.4%, 11.1% and 25.6% reductions), respectively. Besides, in Fig. 5.5 the area under each curve represents the total non-uniformity of block during the heat treatment. Therefore, the differences from one case to another would be representing the difference in total non-uniformities. Fig. 5.5 also shows that shrinkage of the total non-uniformity (area under each curve) was clearly affected when skids and spacers were used. As shown in Table 5.2, the combination of double-height skids and central spacers in DSKC could lower the temperature non-uniformity of the large size block up to 32%, which is a very significant gain. The effects of spacers and double-height

skids are also interpreted by using Fig. 5.5 and Table 5.2. The SKC case study giving a reduction in the temperature non-uniformity of almost 21%, as compared with the 12% of DSK, demonstrates a higher effectiveness of the central spacers in reducing temperature non-uniformities.

Fig. 5.5 (b) and Table 5.2 summarize the trends observed for the slab. Specifically, the maximum non-uniformity and total non-uniformity for the SKC case study were reduced by 7% and 18%, respectively. However, in contrast to the large block, under the DSK configuration the maximum and total temperature non-uniformity increased compare to the SK configuration. It is also interesting to know that for the DSKC case, while approximately the same reduction in the total non-uniformity was observed; however, the maximum temperature non-uniformity (pack of the curve) of the slab slightly increased by 2.6%. This reverse effect could be related to the fact that the spacers in SKC loading pattern increasing the treatment height, reduced the distance between the upper surface of the slab and upper burners, leading to a higher temperature at this surface (see Fig. 5.6).

Table 5.2 Total temperature non-uniformity reduction of forgings
for different loading patterns in comparison with conventional SK loading.

Forgings	DSK	SKC	DSKC
Large-size block	12%	21%	32%
Slab	-1%	18%	19%

Contours of the temperature distributions in the central cross-section of the forging blocks for the four different loading patterns, $t = t_T/6$, are represented in Fig. 5.6. These are for when the maximum temperature non-uniformity occurred in the SK case study (see Fig. 5.5). It should be noted that a distance of 0.5 cm was considered (with a layer of air) between the forged ingots corresponding to the real experience of forged block stacking due to their shape which is not completely flat. However, in the case of existence of spacers a perfect contact was considered due to the weight of blocks. It can be seen that in the SK configuration considerable irregular temperature non-uniformities existed in the blocks from one end to

another.. The cross-section of the large size forged ingot encompass three high temperature regions facing with the down burners and very cold region at the upper surface where the slab was positioned on the top of the large size block. As shown in Fig. 5.6 (a), the coldest part of the large block in the conventional SK case study is not at the center of the block and, on the contrary to the general expectation, it occurs in the upper quarter of the block near the upper face (see also the curve of center modified in Fig. 5.4). The same behaviour can be seen for the slab where the minimum temperature occurs near the bottom surface rather than at the center of the block. This finding is of significant impact from a practical point of view for the steel industry. That is, that part loading configurations need to be taken into account as they could introduce important temperature non-uniformities, and hence, non-uniform properties through the volume of the part even though the total heat treated mass is identical. Analysis of the results reported in Fig. 5.6 (c) and Fig. 5.6 (d), demonstrate that the use of central spacing's between the forgings in the SKC and DSKC increased the temperature of the upper surface of the large size block and the bottom surface of the slab. This resulted in 21% reduction in temperature non-uniformity for the case of SKC in comparison to the conventional SK loading pattern. The results also show that when double height skids were used (Fig. 5.6 (b) and Fig. 5.6 (d)), the high temperature zones located in the lower part of the block were eliminated, resulting in a 12% reduction in temperature non-uniformity in the case of DSK and a total drop of 31% when double height skids alongside central spacers were used (Fig. 5.6 (d)). However, the double-height skids could not affect the temperature uniformity of slabs and these blocks are mainly affected by the central spacers.

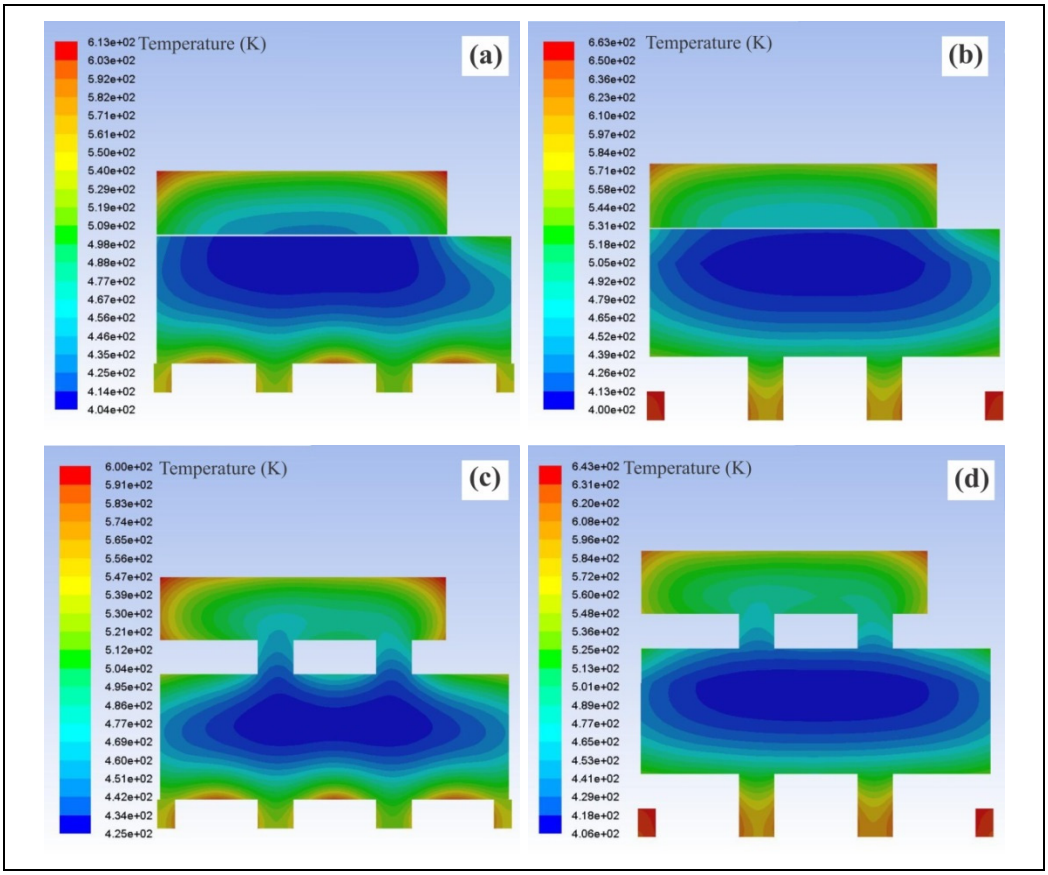

Figure 5.6 Contours of temperature distribution in central cross sections of forgings at $t = t_T/6$. a) SK, b) DSK, c) SKC, and d) DSKC.

5.4.2.1 Influence of spacer skids size on heat transfer modes

The above results clearly demonstrated that the inclusion of the spacers in the analysis affected the severity and distribution of temperature non-uniformity. Although, convection and radiation are the two most important heat transfer mechanisms during the heat treatment process of large size forgings in gas-fired furnaces (Totten, 2006), both from fundamental and application points of view it is however important to quantify the role of each mode in the presence of spacers. To this end, two different spacers with the cross-sectional areas of 0.254×0.245 (m^2) (SKC) and 0.127×0.127 (m^2), half-size SKC or SKHC, were considered for the analysis and the results are reported in Fig. 5.7 (a-d). The results of Fig. 5.7 (a) show that interestingly despite doubling the height and the width of the spacers, the total temperature non-uniformity decreased by the same amount (about 21%). In Fig. 5.7 (b), the

total heat fluxes are compared for the two conditions. The convection heat transfer coefficients were calculated for both cases, and as reported in Fig. 5.7 (c), the values are quite similar while the radiation heat fluxes are different (Fig. 5.7 (d)). This could be explained in terms of the differences in radiation view factors of the surfaces for these two different spacer sizes. Taking into account the approximately similar total heat flux and the same temperature non-uniformity distribution, it can be said that the spacers affect mainly the convection heat transfer mode and therefore the temperature distribution uniformity is controlled by a convection based mechanism rather than a radiation one.

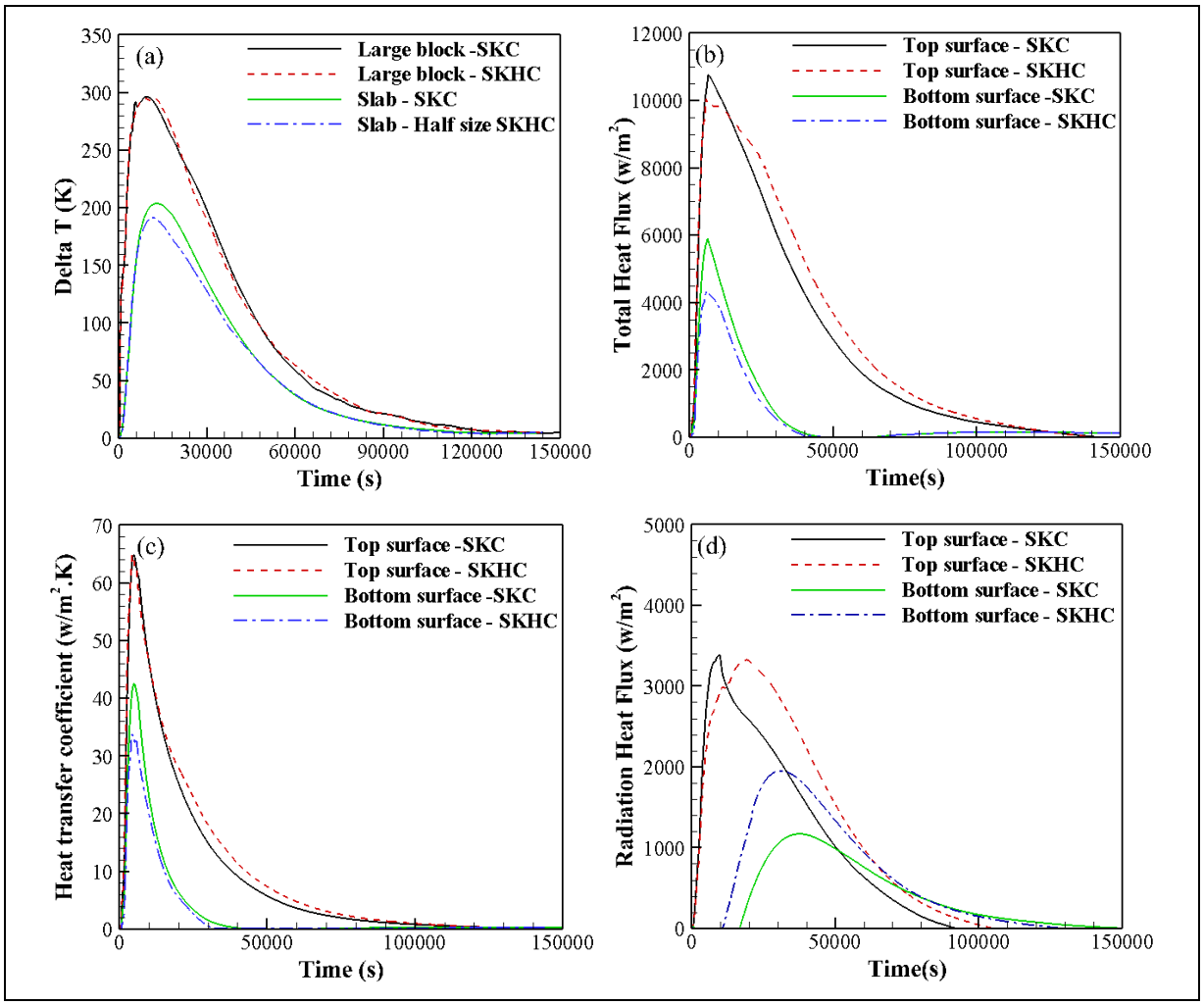

Figure 5.7 Transient history of a) maximum non-uniformity of forgings, b) total heat flux, c) convection heat transfer coefficient, and d) radiation heat flux on forgings surfaces with two different sizes of spacer skids.

5.4.2.2 Influence of loading patterns on the non-isothermal tempering residence time

The evolution of transient average temperature of the forgings and derivation of temperature with respect to time (heating rate) for the different loading patterns are presented in Fig. 5.8.

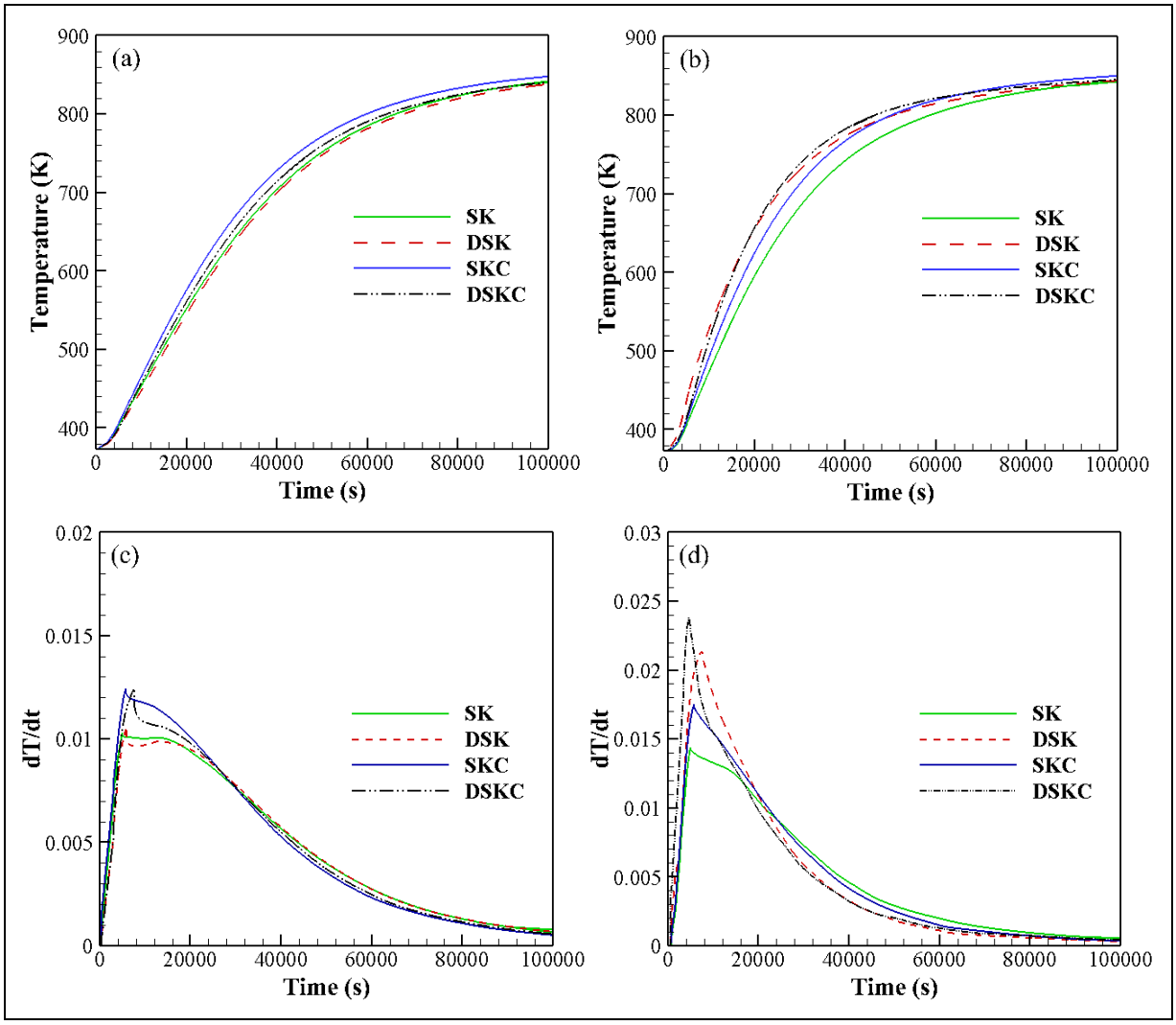

Figure 5.8 Forgings average temperature evolution: a) large size block, b) slab and derivative of temperature evolution with respect to time, c) large size block, and d) slab in different loading pattrens.

It can be seen that positioning of skids and spacers inside the furnace and between the blocks could affect the average transient temperature evolution of the forgings (Fig. 5.8 (a) and Fig.

5.8 (b)) as well as their experienced heating rates in the non-isothermal part of the tempering process (Fig. 5.8 (c) and Fig. 5.8 (d)). It resulted in faster heating rates for both blocks in the SKC and DSKC configurations in comparison with the conventional SK case study leading to higher transient temperature experienced by the blocks (Fig. 5.8 (a) and Fig. 5.8 (b)). Specifically, the slab is more affected by the central spacer skids usage (see also Table 5.3). However, the DSK method resulted in slightly lower heating rates for the large size block (Fig. 5.8 (c)) and subsequently lower temperatures (Fig. 5.8 (a)) because it increased the distance between the block and lower active burners. It should be noticed that although doubling the size of the skid did not reduce the non-uniformity of the slab effectively (see Fig. 5.5 (b)); however, it increased the total height and therefore augmented the contribution of the upper burners to the heating process. This leads to higher heating rates under the DSK and DSKC conditions (Fig. 5.8 (d)).

The relative time reduction (in the heating stage) to reach the target temperature for different loading patterns in comparison with the conventional SK loading is presented in Table 5.2. Results indicated that the DSKC configuration could reduce the heat treatment process by 0.5 hours for the large block and 3 hours for the slab. Besides, the SKC configuration could reduce the process time by 2.5 hours and 3.5 hours for the large the size block and the slab, respectively. Therefore, the SKC loading pattern is more effective to reduce the non-isothermal tempering residence time of the blocks, while, the DSKC pattern is more effective with the view to obtain more homogenous temperature distribution within the large size block (See Fig. 5.5 (a) and Table 5.2).

Table 5.3 Residence time reduction of forgings at different loading patterns in comparison with conventional SK loading pattern.

Forgings	DSK	SKC	DSKC
Large-size block	-1 (h)	2.5 (h)	0.5 (h)
Slab	0.5 (h)	3.5 (h)	3 (h)

5.4.3 Residence time improvement of forgings during isothermal tempering process

The heat treatment process consists of a non-isothermal heating (i.e., the time to reach the target temperature in the loaded furnace) and an isothermal part (i.e., holding at the target temperature for a specified time). As shown in Table 5.3, the effective usage of skids and spacers could reduce the heating time (i.e. the non-isothermal heating step) by about 10% and 14.5% in comparison with the conventional SK non-isothermal tempering for large size block and slab, respectively. This would mean that the isothermal part could be reduced without affecting the final properties. To do so the hybrid methodology was used to reduce the unnecessary holding time of large size forgings inside the gas-fired heat treatment furnace. According to the simulations results the hottest and coldest points at the surface of the slab in the SKC case study reaches the target temperature of 582ºC after 24.5 and 31 hours, respectively (i.e., 6.5 hours of extra isothermal treatment for the hottest point). The dilatometer experiments were carried out with the two above non isothermal heating times and the material hardness (Rockwell C scale, HRC) values were determined. The initial hardness of 54 HRC (after austenitizing and quenching) was reduced to 37.5 ± 0.1 HRC and 37.4 ± 0.1 HRC for 24.5 and 31 hours of non-isothermal tempering, respectively. Thus, an isothermal tempering should be designed to reduce these hardness values to the final desired 34 HRC (within the acceptable range of 31-37 HRC).

Fig. 5.9 represents the detail of the conducted isothermal tempering cycles and their relevant acquired hardness. 20 hours and 46 hours of isothermal tempering at 582ºC resulted in 37.6 ± 0.1 HRC (equivalent to the hottest point hardness after the non-isothermal tempering) and 34.1 ± 0.1 HRC (desired hardness after the tempering process), respectively. Therefore, the present results indicated that a total time of 50.5 hours including 24.5 hours of non-isothermal and 26 hours (equal to the subtraction of 20 from 46 hours) of isothermal holding was needed to reach the target hardness value of 34 HRC.

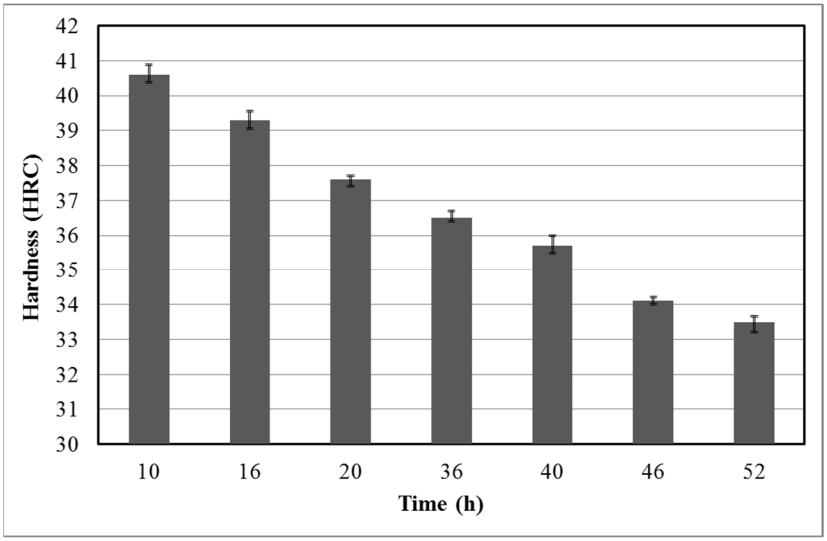

Figure 5.9 Hardness measurements after isothermal tempering at 582ºC for different holding times.

The proposed hybrid approach was validated by using two other tests where the proposed heating cycle was examined for the slab hottest and coldest points. In these experiments, the non-isothermal heating cycle taken from the CFD results followed by the optimal calculated isothermal tempering, resulted in 33.9 ± 0.1 and 34.6 ± 0.1 HRC hardness values which are in the acceptable range for this product.

On the basis of the obtained results, the total residence time of the parts inside the heat treatment furnace could be reduced by 9.5 hours (i.e., 15.5% reduction). Considering the excessive energy consumption of this type of furnaces and the very large number of the heat treated parts, such a time saving along with improving the temperature uniformity, and hence properties, of the final product could significantly contribute to the production cycle from both cost and quality points of view.

5.5 Conclusions

The loading pattern effect on the forgings temperature uniformity and their residence time inside the gas-fired heat treatment furnaces was investigated using the CFD simulation and

experimental temperature measurements. Besides, a hybrid numerical-physical simulation approach was introduced and performed to optimize the residence time of large size slabs inside gas-fired heat treatment furnaces. The following conclusions can be drawn from the present work:

1) Large size forgings in the non-optimized conventional loading pattern experienced temperature non-uniformities up to 331 K due to furnace geometry and loading pattern.
2) Using double size skids and central spacers reduced the temperature non-uniformity of large size forgings inside the gas-fired furnace up to 32%.
3) Convection heat transfer was the dominant mechanism in the presence of central spacers to affect the temperature uniformity of the heavy steel parts.
4) It was possible to reduce the total residence time of large size slabs (including non-isothermal and isothermal tempering) by about 15.5% in the gas-fired heat treatment furnace.
5) A hybrid methodology was proposed and validated for residence time optimization of large size forging. The proposed approach could be applied to other furnace types or part geometries.

CHAPTER 6

CFD SIMULATION OF A GAS-FIRED HEAT TREATMENT FURNACE: ASSESSMENT OF EQUILIBRIUM NON-PREMIX COMBUSTION AND DIFFERENT TURBULENCE MODELS

Nima Bohlooli Arkhazloo[a,*], Farzad Bazdidi-Tehrani[b], Mohammad Jadidi[b], Jean-Benoît Morin[c] and Mohammad Jahazi[a]

[a] Département de Génie Mécanique, École de Technologie Supérieure, Montréal, Québec, Canada H3C 1K3,

[b] School of Mechanical Engineering, Iran University of Science and Technology, Tehran, Iran 16846-13114

[c] Finkl Steel Inc., 100 McCarthy, Saint-Joseph-de-Sorel, Québec, Canada J3R 3M8

Paper submitted to *Energy & Fuels,* In December 2019*,*

Abstract

In this study transient computational fluid dynamics (CFD) simulations of a batch type gas-fired heat treatment furnace were carried out in order to investigate the applicability of equilibrium non-premix combustion model and the effect of different turbulence models on the thermal interactions inside the furnace. A one-third periodic 3D model of the furnace, employed for tempering of large size forgings, was used as the domain for the simulations. The performances of several transient RANS based turbulence models along with the non-premix combustion with equilibrium model approaches were evaluated. To do so, thermal interactions analyses based on temperature measurements on an instrumented large size block were performed in different locations of the forged blocks as well as critical regions in the burner area, stagnation and wake regions. Results indicated that non-premix combustion with chemical equilibrium could effectively be employed for combustion modeling of high-momentum cup burner combustion and subsequently temperature prediction of the products. A very good agreement, with a maximum deviation of about 4%, was obtained using the

periodic model indicating the reliability of the developed model. Prediction of ε/k ratio using different turbulence models could significantly affect mixture fraction variance and subsequently flame length and product temperature at the stagnation point. RSM was found as the most reliable turbulence model compared to the experimental measurements. Furthermore, it was found that the realizable $k-\varepsilon$ model reasonably predicted the global block temperature during the heat treatment process. However, it under-predicted the flame length and block temperature in the stagnation region. While, the SST $k-\omega$ model could not capture the flow recirculation behind the block and over-predicted the block temperature near the wake region and inside the block, it showed reasonable results in the stagnation region which can be used for process optimization.

Keywords: Gas-fired furnace, Computational fluid dynamics (CFD), Turbulence modeling, Equilibrium non-premix combustion, Flame length, Mixture fraction variance

Nomenclature

Latin symbols

d	Characteristic dimension (m)
$C_{1\varepsilon}$,$C_{2\varepsilon}$,$C_{3\varepsilon}$	Constants in $k-\varepsilon$ equations
C_g, C_d	Constants in mixture fraction variance transport equation
E	Energy (J)
$\bar{f}$	Mean Mixture fraction
$\bar{f}'^2$	Mixture fraction variance
g	Gravity (m/s^2)
J_i^z	Diffusive flux of chemical species
h	Enthalpy (j/kg)
H	Block height
k	Turbulence kinetic energy (m^2/s^2)
k_{eff}	Effective thermal conductivity

L	Furnace length in longitudinal direction
m^{g}	Mass flux ($kg/\mathrm{m}^2.s$)
OH	Hydroxide
p	Pressure (Pa)
q_i,	The generic source term
q_r	Reaction heat term respectively
q_s	The generic source term
R_z	Production rate of z_{th} component
$R_{z,r}$	Production rate of z_{th} component
Re	Reynolds number (ud/μ)
S_z	Source term of z_{th} component production
Sc	Schmidt number
t	Time (s)
T	Temperature (K)
t_T	Total heat treatment time
u_i	Reynolds-averaged velocity in tensor notation
u_i'	Resolved fluctuating velocity components
$X, \mathrm{Y}, \mathrm{Z}$	Direction of coordinate axes

Greek symbols

ε	Turbulence dissipation rate (m^2/s^3)
ν	Kinematic Viscosity (m^2/s)
μ_t	Turbulence eddy viscosity ($kg.m/s$)
ρ	Density (kg/m^3)
$\sigma_k, \sigma_\varepsilon$	Prenatal number for the kinetic energy and dissipation rate, respectively

σ_t	Constant in mixture fraction variance equation
σ, σ_s	Stefan-Boltzmann constant and scattering coefficient
$\rho\overline{u_i' u_j'}$	Reynolds stress ($kg/\mathrm{m}.s^2$)
Ω'	Solid angle
τ_{ij}	Viscous stress tensor

Superscripts

'	Fluctuations with respect to a Reynolds averaging

Subscripts

i, j, k	Tensorial indices
z	z_{th} species
gas	Gas

Abbreviation

3D	Three dimensional
CFD	Computational Fluid Dynamics
DO	Discrete ordinates model
EDM	Discrete ordinates model
RANS	Reynolds-averaged Navier–Stokes equations
RNG	Re-normalization group
RSM	Reynolds stress model
RFL	Rich Flammability Limit
RTE	Radiative transfer equation
RTE	Radiative transport equation
SST	Shear stress transport
TKE	Turbulence kinetic energy

6.1 Introduction

Steel industry extensively employs gas-fired heat treatment furnaces to raise the temperature of steel parts to desired levels at which different metallurgical processes such as phase transformation and carbide precipitation take place. This is to allow for achieving the targeted mechanical properties (Totten, 2006). Final material properties are usually optimized by tempering parameters modification (such as temperature, time, etc.) in the gas-fired heat treatment furnaces (Kang & Rong, 2006; Yan et al., 2017). Therefore, accurate heat transfer and temperature distribution prediction of the parts necessitates a comprehensive analysis of thermal interactions and their subsequent effects on the transient temperature evolution of the product within the furnace. This analysis should consider furnace operation complexities including combustion, heat exchange within furnace, turbulence, flame, furnace characteristics (geometry, bottom skids, etc.), the composition of the steel products, and their internal heat conduction. However, due to the high temperatures, experimental measurements in gas-fired furnaces are complex and expensive to perform (Gao et al., 2000). Measurements and data acquisition become more difficult when it comes to the analysis of large size steel parts' heat treatment inside such furnaces. Besides, analytical studies due to their limitation in non-linear transient applications show large deviations with the real thermal experiences of the products (Gao et al., 2000). Therefore, due to the lack of such data, the current practice for the heating cycle schedule is based on empirical correlations and is mostly limited on monitoring of the furnace temperature as a function of the furnace load (Kang & Rong, 2006; S. F. Zhang et al., 2009). Empirical correlations, however, cannot be used precisely to predict products temperature and show large deviations with the loading pattern or furnace configurations (Gur & Pan, 2008; Hao et al., 2008).

Recently, computational fluid dynamics (CFD) has been used for the evaluation of different industrial furnaces and their relative thermal interactions (B Mayr, Prieler, Demuth, Moderer, et al., 2017; Yang et al., 2006). Several studies such as those of Hao et al. (Hao et al., 2008), Lior (Lior, 2004), Kang and Rong (Kang & Rong, 2006) and Wang et al. (J. Wang et al., 2008) employed CFD to analyze the flow and thermal interactions within electrically heated

or gas quenching furnaces. However, due to the complexity of reactive flow, little data is available for gas-fired heat treatment furnaces where the products are subjected to long transient heating cycles. Gas-fired furnaces are mostly heated by high momentum gas-fired burners. Owing to the high momentum of burner products and working temperatures, both radiation and convection heat transfer modes are active in the heating process. Such furnaces, aside from the existence of turbulent reactive flows inside the system, contain absorbing and emitting hot combustion product gases which make the radiation simulation more complex. Besides, probably due to the high computational cost of batch type gas-fired furnaces' simulation, most of the studies have been focused on simplified cases. Specifically, steady-state simulation of continoues heat treatment furnaces (Tang et al. (Tang et al., 2017) and Mayr et al. (B Mayr, Prieler, Demuth, Moderer, et al., 2017)) or small scale or laboratory scale heat treatment furnaces (such as those of Yang et al. (Yang et al., 2007), Prieler et al. (Prieler, Mayr, et al., 2015), Govardhan et al. (Govardhan et al., 2011) and Mayr et al.(B Mayr, Prieler, Demuth, Potesser, et al., 2017)) or only one part of the process rather than simultaneous analysis of furnace domain and products heating (like Galletti et al, (Galletti et al., 2013) and Danon et al. (Danon et al., 2011)) can be found in the literature. However, the above studies have been performed with different research purposes, namely, product temperature prediction, combustion simulation, non-uniformity identification and loading pattern or residence time optimization. This makes it difficult to evaluate the strengths and limitations of different CFD approaches for the prediction of thermal interactions such as turbulent convection heat transfer within the furnace. Besides, a good agreement with CFD simulations for temperature (scalar) is not necessarily the result of a correct flow-field computation.

The accuracy of CFD predictions of the flow field are significantly affected by the applied numerical modeling approaches (Tominaga & Stathopoulos, 2013). For example, determination of proper turbulence modeling and combustion modeling approaches is of great importance since they form the cornerstones of a CFD simulation and directly affect the conjugate heat transfer (convection and radiation heat transfer to the load) and fluid flow regime inside the furnace. Besides, such flow-field data provide complementary information

to the combustion evaluation in the gas-fired furnaces. Regions with high gradient of velocity, rotation and mixing like wake region, flame region or stagnation region need to be considered in a systematic approach. Therefore, high performance turbulence models are required to capture the physics of the problem, while maintaining simplicity in the formulation, stability in convergences and competitive computational time. However, very few studies have systematically investigated the sensitivity of the results to these computational approaches in large size furnaces. Among the few studies published on gas-fired furnaces, Prieler et al. (Prieler, Demuth, et al., 2015) investigated the steady-state heat transfer in oxygen enriched combustion environment in lab-scale and semi-industrial heat treatment furnaces emphasizing on the application of steady flamelet model (SFM) for combustion of oxy-fired burners. Three $k-\varepsilon$ group models as well as the RSM model were compared and according to the authors, the realizable $k-\varepsilon$ along with RSM model showed very similar results regarding temperature and flame length predictions. In another study (Prieler et al., 2016), the same authors investigated the turbulence modeling of the process in a walking hearth type reheating furnace and found that the realizable $k-\varepsilon$ model predicted similar flame shape and temperature but a longer flame length in the vicinity of the burner when compared to the RSM model. This resulted in 30-50 K over-prediction of furnace wall temperature by the realizable $k-\varepsilon$. However, there is no available data for the transient simulation of large size steel parts inside batch type industrial heat treatment furnaces with high momentum gas-fired burners. An accurate transient simulation requires a simultaneous analysis of turbulence and combustion modeling in different critical points of the furnace and the product.

The present paper aims to address the above challenges and uses different numerical approaches to simulate the heat treatment process of large size steel parts inside a gas-fired heat treatment furnace. In this regard, a one-third 3D CFD model of a large size gas-fired furnace in a periodic configuration was proposed as the computational domain. Details of the numerical simulations, including boundary conditions were specified and the model predictions were experimentally validated by instrumenting the blocks with K type thermocouples and recording temperature evolution during the heat treatment process. Then,

six different RANS based turbulence modeling approaches were assessed to determine the most reliable predictions of turbulent flow field inside the gas-fired heat treatment furnace. Besides, the applicability of a non-premix combustion model with a chemical equilibrium model to simulate the combustion of high-momentum cup burner in the excess air mode was assessed. Analysis of different critical points from turbulence and combustion points of view was performed for the assessments. The results were analyzed and interpreted in terms of the temperature predictions in critical regions inside the furnace and around the block, namely, stagnation point, wake region etc. Analyses of flame length, vortical structures and turbulence characteristics were considered for the analyses.

6.2 Furnace Description

The present investigation was conducted on a large size batch- type gas-fired heat treatment furnace with the internal dimensions of 3.05 (m), 3.28 (m), and 8.83 (m), in the X, Y and Z directions, respectively. The furnace was heated by 18 high-momentum Tempest cup-burners (Baukal Jr, 2003) located in an asymmetric arrangement. Nine burners were located along the Z direction of the furnace on the upper section of the furnace left wall, and the other nine burners were installed on the lower section of the furnace right wall. Nine skid bars with the rectangular cross section of 0.25 (m) × 0.25 (m) were positioned between the burners for placing the large size forged blocks. An approximately 0.2 (mbar) positive pressure was considered in the design of the furnace to minimize air entry.

The combustion process in the Tempest burner was done in two steps; the primary air flow (20% of total air) was mixed with gas before the ignition (at the primary chamber) and the secondary air flow (80% of total air) was added to the mixture, afterward. The primary and secondary chambers were fed by air swirls with a 45^{o} angle slope. According to the manufacturer, the flame length was 0.508 (m) and the combustion product velocity at the exit of burner was 107 (m/s) for the nominal air pressure of 110 (kPa) at the burner inlet.

6.3 Numerical Details

6.3.1 Flow and Energy modeling

The Reynolds averaged Navier-Stokes (RANS) equations including continuity, momentum and energy equations are defined as in Eq. 6.1 to Eq. 6.3. The solution to these equations in the transient CFD simulations (i.e., to predict the time-dependent thermal interactions inside the furnace) employing a double precision pressure-based solver, was carried out in the finite-volume based ANSYS-FLUENT software (ANSYS, 2016), as follows.

$$\frac{\partial \rho}{\partial t}+\frac{\partial}{\partial x_i}(\rho u_i)=0 \tag{6.1}$$

$$\frac{\partial}{\partial t}(\rho u_i)+\frac{\partial}{\partial x_j}(\rho u_i u_j)=-\frac{\partial p}{\partial x_i}+\frac{\partial \tau_{ij}}{\partial x_j}-\frac{\partial}{\partial x_i}(\rho\overline{u_i' u_j'})+F \tag{6.2}$$

$$\frac{\partial}{\partial t}(\rho E)+\frac{\partial}{\partial x_j}(\rho u_i h)+\frac{\partial}{\partial x_j}(u_i p)=\frac{\partial}{\partial x_i}(\mathrm{k}_{eff}\frac{\partial T}{\partial x_i}-\sum_{z=1}^{n} h_z \mathrm{r}J_z+u_i\tau_{ij})-\frac{\partial}{\partial x_j}(\overline{\rho u_i' h_s'})+q_s \tag{6.3}$$

where, ρ, u, p, F, h, q_i ,and k_{eff} represent fluid density, fluid velocity, pressure, body forces, enthalpy, generic source and effective heat conduction coefficient, respectively. In Eq. 6.2 and Eq. 6.3 τ_{ij} is the stress tensor given by:

$$\tau_{ij}=\left[\mu_t\left(\frac{\partial u_i}{\partial x_j}+\frac{\partial u_j}{\partial x_i}\right)\right]-\frac{2}{3}\mu_t\frac{\partial u_l}{\partial x_l}\delta_{ij} \tag{6.4}$$

and $\mathrm{r}J_z$ is the diffusive flux of combustion product species defined by the Fick's law:

$$\partial \mathrm{r}J_z=-\frac{\mu_t}{Sc_k}\frac{\partial Y_z}{\partial x_i} \tag{6.5}$$

The group of two equation $k-\varepsilon$ models (standard, RNG and realizable) as well as the $k-\omega$ models (standard and SST $k-\omega$) along with RSM were assessed in the present study. The standard $k-\varepsilon$ model, proposed by Launder and Spalding (Launder & Spalding, 1972), using the Boussinesq's isotropic linear eddy-viscosity concept, showed good agreement with the experimental measurements according to the literature (Bohlooli Arkhazloo et al., 2019; Y.

Liu et al., 2014; J. Zhang, Prationo, Zhang, & Zhang, 2013). In this model the following two additional transport equations for the turbulence kinetic energy, k, and turbulence dissipation rate, ε, are solved:

$$\frac{\partial}{\partial t}(\rho k)+\frac{\partial}{\partial x_j}(\rho k u_i)=\frac{\partial}{\partial x_j}\left[\left(\mu+\frac{\mu_t}{\sigma_k}\right)\frac{\partial k}{\partial x_j}\right]+G_k+G_b-\rho\varepsilon \tag{6.6}$$

$$\frac{\partial}{\partial t}(\rho \varepsilon)+\frac{\partial}{\partial x_j}(\rho \varepsilon u_i)=\frac{\partial}{\partial x_j}\left[\left(\mu+\frac{\mu_t}{\sigma_\varepsilon}\right)\frac{\partial \varepsilon}{\partial x_j}\right]+C_{1\varepsilon}\frac{\varepsilon}{k}(G_k+C_{3\varepsilon}G_b)-C_{2\varepsilon}\rho\frac{\varepsilon^2}{k} \tag{6.7}$$

where $C_{1\varepsilon}$, $C_{2\varepsilon}$ and $C_{3\varepsilon}$ as well as the mean turbulent Prandtl number for the kinetic energy (σ_K) and dissipation rate (σ_ε) are constant according to Launder and Spalding (Launder & Spalding, 1972). While, G_k and G_b are related to turbulence kinetic energy due to the velocity gradient and buoyancy effect, respectively. In above equations, $(\mu+\mu_t/\sigma_k)$ and $(\mu+\mu_t/\sigma_\varepsilon)$ are also called as effective diffusivity of k and ε, respectively. The realizable $k-\varepsilon$ model has been tested in several applications such as curvature streamlines and steady state simulations of lab scale gas-fired furnaces (Kim, Choudhury, & Patel, 1999; Bernhard Mayr et al., 2015). The major difference after tuning the equation constants for more complex flow field, with respect to the standard $k-\varepsilon$, is the calculation of eddy viscosity and dissipation rate (Shih et al., 1993). The re-normalization group $k-\varepsilon$ model, also called the RNG model, using analytical re-normalization technique with scale expansions for the Reynolds stress, provides modified constants of the standard $k-\varepsilon$ model. Besides, $C_{1\varepsilon}$ in this model is replaced by $C^*_{1\varepsilon}$ which is calculated from an auxiliary function (Yakhot et al., 1992).

The standard $k-\omega$ model based on the Wilcox $k-\omega$ model (Wilcox, 1998) is an empirical model that solves the transport equations for k and ω, which can also be considered as the ratio of ε/k. This model was reported to present reliable results in far wakes, mixing layers and more importantly wall-bounded flows and free shear flows (Wilcox, 1998). Shear-stress transport (SST) $k-\omega$ (Menter, 1994) has a blending function to use the capabilities of near wall region of the standard $k-\omega$ model with the free-stream independence of the $k-\varepsilon$ model in the far field. The definition of turbulent viscosity as well as modeling constant is

modified in the SST $k-\omega$ model with respect to the standard $k-\omega$ model (Menter, 1994). In the two equation models, the turbulent viscosity is calculated using empirical or theoretical correlations between turbulence kinetic energy and eddy dissipation rate for the specific flow conditions. The RSM model, on the other hand, solves all Reynolds stresses and turbulence dissipation instead of using eddy-viscosity concept. In this respect, RSM solves seven turbulence transport equations for 3D flows considering the turbulence anisotropy. This is in contrast to the two equation models which assume isotropic turbulence field (Cant, 2001).

6.3.2 Combustion and radiation modeling

In the present study, the equilibrium non-premix combustion model was used to predict the natural gas combustion inside the burner and furnace domains. The applicability of the eddy-dissipation model (EDM) (B. F. Magnussen & Hjertager, 1977) for an accurate prediction of the temperature distribution in large size forgings within gas-fired furnaces was recently reported (Bohlooli Arkhazloo et al., 2019). Considering that in the Tempest burner natural-gas and oxidizer enter into the reaction zone in distinct streams (20% of air with the gas reacts in the primary chamber and 80% of air reacts in the secondary chamber) the applicability of non-premix combustion with the chemical equilibrium model using β-shape probability-density function (PDF) was assessed in the present investigation. The non-premix with PDF model was developed for the turbulent diffusion flame with a fast chemistry assuming that the reaction in the turbulent combustion is sufficiently rapid to reach equilibrium resulting in lower computational cost in comparison with the EDM model (Ismail, Ng, & Gan, 2012).

In the non-premix model, combustion is simplified to a mixing problem by assuming equal diffusivities for all the species and species concentration is derived from the predicted mixture fraction fields stored in a table (ANSYS, 2016). Therefore, computations of non-linear reaction rates are avoided. The mixture fraction is defined as (Ishii, Zhang, & Sugiyama, 1998):

$$f = \frac{z_i - z_{\mathrm{i},ox}}{z_{\mathrm{i},gas} - z_{\mathrm{i},ox}} \tag{6.8}$$

Where z_i is the elemental mass fraction of species z. In the case of secondary stream (including fuel or oxidizer) the sum of all three mixture fractions (f_{fuel}, f_{sec} and f_{ox}) is equal to unity. The density averaged solved mixture fraction is then, as follows:

$$\frac{\partial}{\partial t}(\rho \bar{f}) + \frac{\partial}{\partial x_j}(\rho \mathrm{r}\bar{v}\bar{f}) = \nabla.\left[\left(\frac{\mu_t}{\sigma_t}\right)\nabla \bar{f}\right] \tag{6.9}$$

Further conservation equation for the mixture fraction variance, $\bar{f}'^2$, should also be solved (ANSYS, 2016).

$$\frac{\partial}{\partial t}(\rho \overline{f'^2}) + \nabla.(\rho \mathrm{r}\overline{v f'^2}) = \nabla.\left[\frac{\mu_l + \mu_t}{\sigma_t}\nabla \overline{f'^2}\right] + C_g \mu_l.(\nabla \bar{f})^2 - C_d \rho \frac{\varepsilon}{k}\overline{f'^2} + S \tag{6.10}$$

According to the experimental studies and reviews in the literature (Bowman, 1991; Sivathanu & Faeth, 1990) for lean combustion conditions, as in the present study, where 5% excess air was entered to the burners, the generalized state relationships approximate the thermodynamic equilibrium. Therefore, an equilibrium chemistry with a rich flammability limit (RFL) of 0.1 to accommodate chemical non-equilibrium was employed for the combustion simulation. According to Bohlooli et al. (Bohlooli Arkhazloo et al., 2019) the discrete ordinates model (DO) (Raithby & Chui, 1990) can effectively be used in the simulation of the present gas-fired heat treatment furnace. The absorption and emission effects of the furnace medium in the solution of the radiative transfer equation (RTE) were taken into consideration by using the weighted-sum-of-gray gases model (WSGGM), as reported in (Smith et al., 1982).

6.3.3 Simulation procedure

A pressure-velocity coupling was carried out using the SIMPLE algorithm (Henk Kaarle Versteeg & Malalasekera, 2007) in a computational domain consisting of 4,842,940 hexahedral non-uniform grids, as shown in Figs. 6.1 and 6.2. Due to the significant variations in the range of high temperature and gradient in species concentration near the burner regions, finer grids with low growth were used in those regions. Enhanced wall treatment

with $y^+ < 1$ criteria was considered for the simulations. An averaged heat loss of 594 (W/m^2) was applied to the furnace wall (covered by refractory ceramic fibers with a typical thickness of 0.254 (m)) in accordance with the approach proposed by Hadala et al. (Hadała et al., 2017). The mass flow inlet boundary condition for the natural-gas (with a typical methane mole fraction of 0.94) and air inlets was employed at the burner inlets.

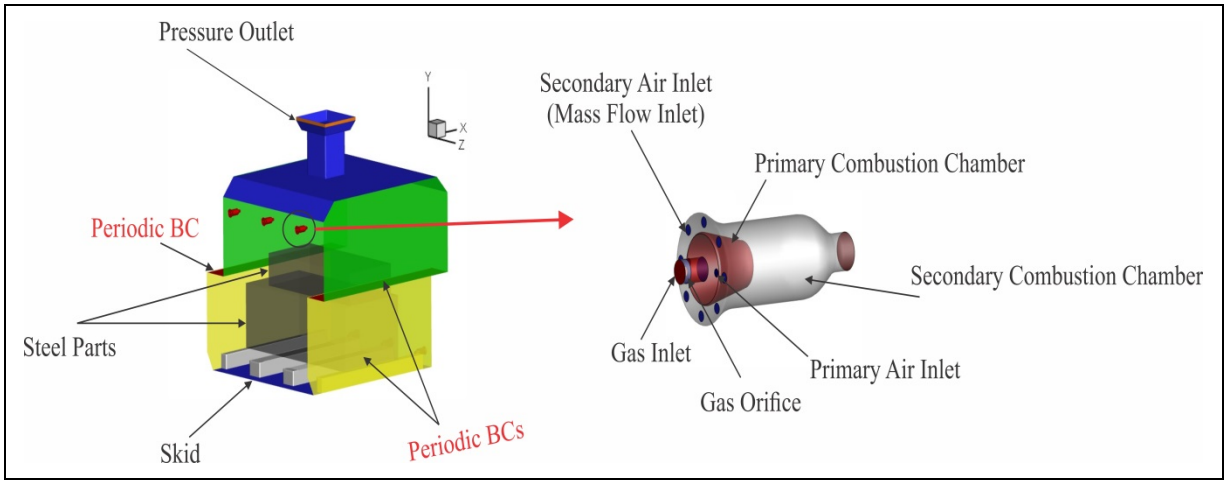

Figure 6.1 Computation model boundary conditions.

The furnace temperature during the experimental measurements was controlled using a Honeywell UDC 2500 PID controlling system. PID controller divided the furnace length into three similar zones and by controlling the gas flow rate in each zone balanced the geometrical effects (door or back-wall) on the temperature variations in these zones. Therefore, the large size blocks in the three zones experienced almost the same heating history along the length of the furnace and the middle zone can be a reliable representative of the three zones. Thus, a one-third model of the furnace was specified for the simulations. In this respect, periodic boundary conditions were applied in the Z direction (refer to Fig. 6.1). The convergence criteria for the continuity, energy and mean mixture fraction equations at each time step were 10^{-5}, 10^{-9} and 10^{-6}, respectively.

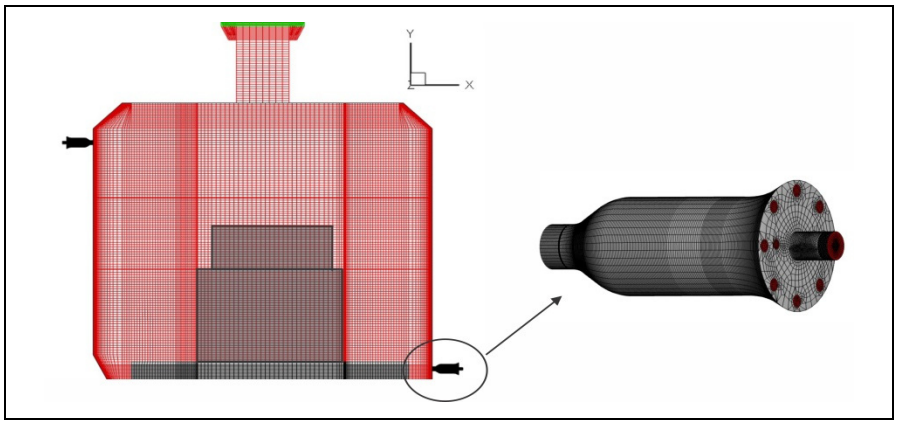

Figure 6.2 Grid resolution of furnace domain and its details including gas-fired burner.

Due to the high amount of temperature variance during the heat treatment process, temperature dependent thermo-physical properties were taken into account in the present simulations. These properties were estimated using JMatPro software (JMatPro Users Guide 6.2.1.), as shown in Fig. 6.3 (a). The chemical compositions of the steel parts used in this computation are presented in Table 6.1. The emissivity of steel parts, as oxidized steel surface, was set to 0.8 while, refractories' emissivity was set to 0.75. The pressure outlet boundary conditions were assumed for the chimneys' exhaust.

Table 6.1 Chemical Analysis of the test Ingot - Weight % (Finkl Steel Inc).

Fe	C	Mn	Si	Mo	Cr	Ni	Other
Bal.	0.35	0.85	0.4	0.45	1.85	0.47	Micro alloying

6.4 Experimental measurements

Transient temperature measurements of the block as well as gas and air flow metering of the burners were carried out during the heat treatment process. Specifically, a 1.4×0.89×2.72 (m^3) forged block and a 1.09×0.50×2.25 (m^3) slab, placed on its upper surface, were considered as the case study. The two other sets of blocks were positioned with the same relative distance, so as not to disturb the uniformity in the Z direction. The K type thermocouples were embedded at different locations of the block including the stagnation

region, side walls and wake region in the central zone of the furnace. Details of the temperature measurement procedure including installation and positioning are provided in the recent publication of Bohlooli et al. (Bohlooli Arkhazloo et al., 2019). Gas and air flow rates were measured using high precision orifice plate flow meters. Fig. 6.3 (b) illustrates the transient history of the furnace gas consumption during the heat treatment process. As it can be seen, at the early stages of the process, the gas consumption is high and gradually decreases until it stabilizes at a certain level which corresponds to the target holding temperature.

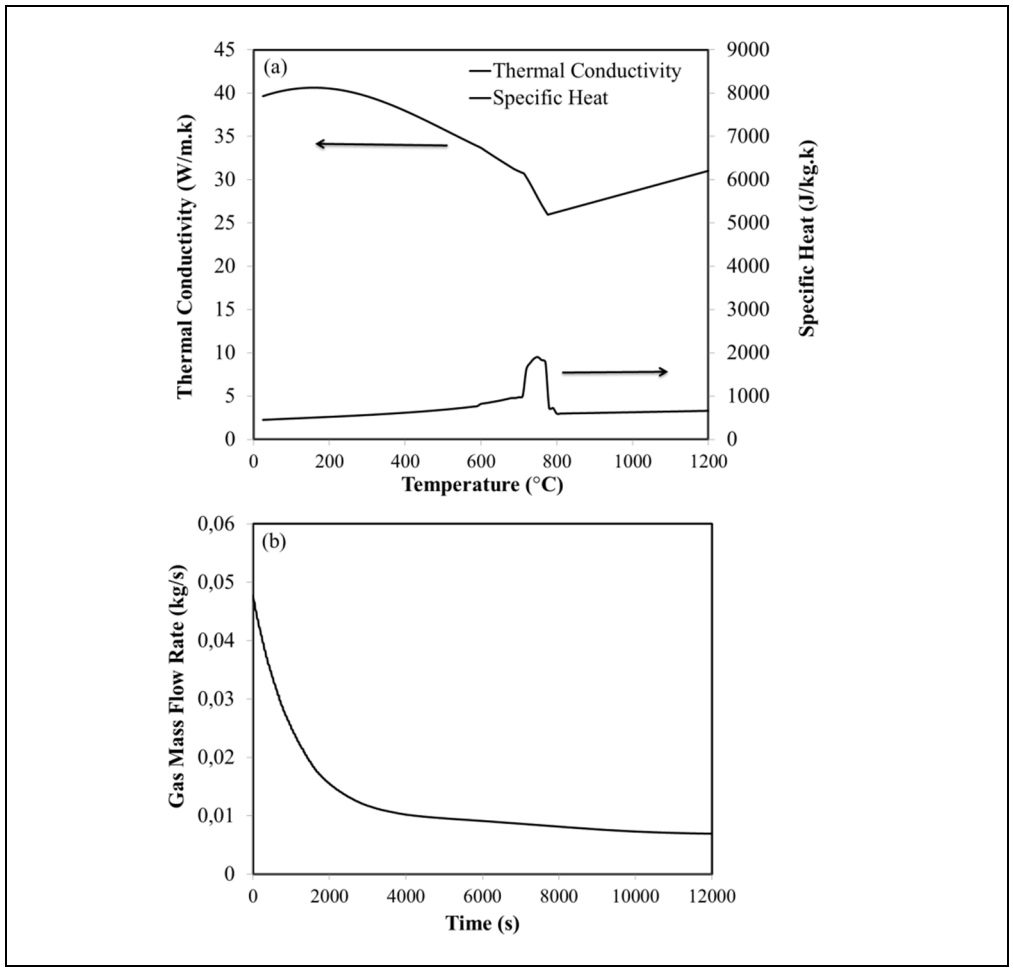

Figure 6.3 CFD model inputs a) temperature dependent thermo-physical properties of steel parts estimated by JMatPro software, and b) measured furnace gas consumption.

6.5 Results and Discussion

6.5.1 Validation of periodic CFD model and combustion approach

A comparison between the CFD model predictions and the transient measured temperature is presented in Fig. 6.4. The CFD model, consisting of the one-third periodic domain and adopting the non-premix combustion with the equilibrium model together with the standard $k-\varepsilon$ model was used for the validation. It can be observed that the present CFD model predicts the transient temperature history of the steel parts in the gas-fired furnace reasonably well with a maximum over-prediction of 4%. Therefore, the chemical equilibrium non-premix combustion model which requires a lower computational cost, as compared with EDM, was employed as the basis for the assessment of turbulence modeling in the investigated application.

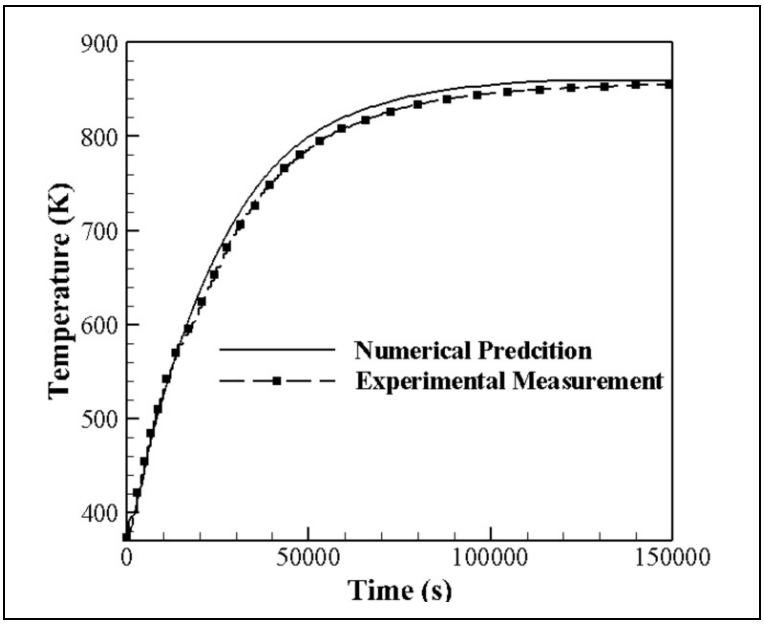

Figure 6.4 Periodic CFD model including equilibrium non-premix combustion model validation.

6.5.2 Assessment of turbulence models

6.5.2.1 Temperature predictions of forged block

Accurate prediction of the temperature of bluff bodies and the corresponding flow fields in a turbulent fluid flow is a challenging task (Ničeno et al., 2002). The thermal analysis of the forged block mounted on the skid bars facing with burners' flow stream, share several similarities to the typical bluff bodies flow field such as stagnation point, wake region and flow around the block (Bohlooli Arkhazloo et al., 2019). Therefore, these similarities were used to analyze the thermal interactions in the present application. Fig. 6.5 represents the temperature predictions by six various RANS based turbulence models at three different locations of the forged block. Also, the measured data at the point in time ($t = t_T/6$), where the maximum temperature non-uniformity of the product was found (Bohlooli Arkhazloo et al., 2019), are illustrated.

Accurate prediction of the stagnation point is one of the critical points when analyzing flow over a bluff body and an impingement jet. Different turbulence models have been used to predict the stagnation point's temperature with various levels of accuracy, as reported by Ničeno et al. (Ničeno et al., 2002) and Murakami (Murakami, 1993). In the present study, the flow coming from the lower burners is faced with the right surface of the large block, resulting in a stagnation point having similarities to an impingement jet application. Figure 6.5 (a) depicts the comparison between the measured temperature at a point (perpendicular to the burner center line and 5 (cm) above the lower face of the block) in the stagnation region and the corresponding predictions by the turbulence models. It can be seen that the standard and realizable $k-\varepsilon$ models under-predicted by about 3.5% the temperature of the stagnation region. This finding is in agreement with the results reported by Pulat et al. (Pulat, Isman, Etemoglu, & Can, 2011) who also found that $k-\varepsilon$ group under-predicts the temperature of the stagnation point in a typical impingement flow field.

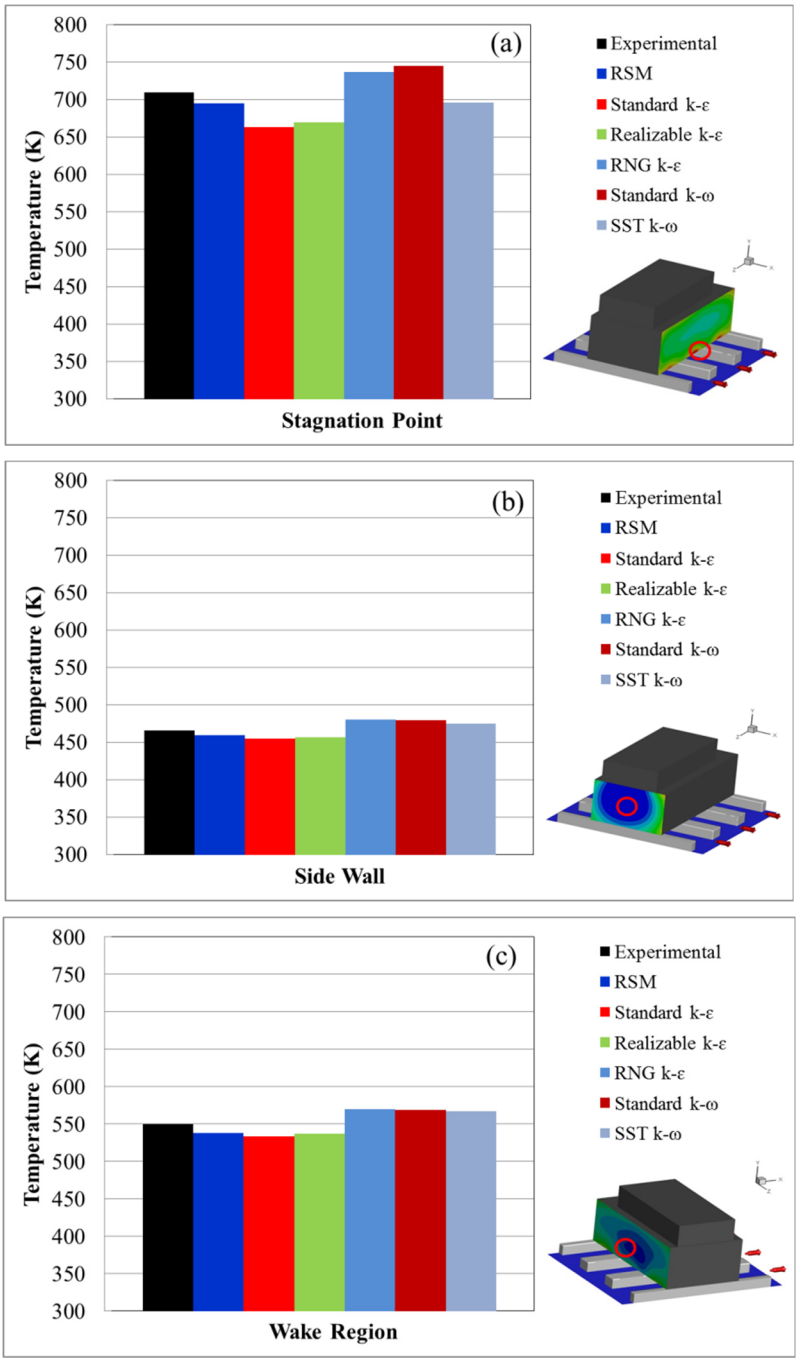

Figure 6.5 Comparison of temperature predictions by various turbulence models and experiment at different locations of forged block: a) stagnation point, b) side wall, and c) wake region at $t = t_T/6$.

On the other hand, the standard $k-\omega$ and RNG $k-\varepsilon$ models showed a significant over-prediction of the stagnation temperature, while, SST $k-\omega$ and RSM lead to better agreements with the experimental data. The capability of the SST $k-\omega$ model in the accurate prediction of the stagnation region regarding an impingement jet application has been reported by several researchers (Ortega-Casanova & Castillo-Sanchez, 2017; Zuckerman & Lior, 2006) and the present work confirms this for the application to gas-fired furnaces. The better performance of SST $k-\omega$ is probably due to the fact that the influence of the viscous sub-layer is considered in this model. This allows for taking into account large gradients of velocities, temperature and turbulence scalar quantities that are present near the wall region and therefore provide a better representation of the actual conditions. Fig. 6.5 (a) also shows that the RSM model solving all Reynolds stresses and turbulence dissipation and considering turbulence anisotropy exhibited reliable predictions compared to the experimental measurements.

Fig. 6.5 (b) displays the temperature predictions of different models for the region located at the center of the block's side wall (front and back walls). It should be noted that the difference between temperature measurements on the side walls was less than 0.5% and, therefore, only those for the front wall are illustrated. It can be seen that there is an acceptable consistency between all the predictions and the experimental data with a maximum deviation being about 3% for the RNG $k-\varepsilon$ model.

Furthermore, Fig. 6.5 (c) shows clearly that the wall in the wake region plays a critical role in the selection process of the turbulence model. For instance, it can be seen that the realizable $k-\varepsilon$ model had more consistency with the measured data (2.3% under-prediction) among the $k-\varepsilon$ group and the SST $k-\omega$ model (about 3% over-prediction) from the $k-\omega$ group showed better predictions. The RSM model with 2.1% under-prediction concerning the temperature prediction of the wall in the wake region showed reasonable consistency with the measured data. On the basis of the above analysis and the temperature predictions of the three different walls of the block, the RSM model can be considered as the most accurate model in the context of the present study.

6.5.2.2 Combustion flow field predictions

Fig. 6.6 depicts the contours of time-averaged temperature around the high momentum burner in the lateral plane perpendicular to the lower burners' central cross-section.

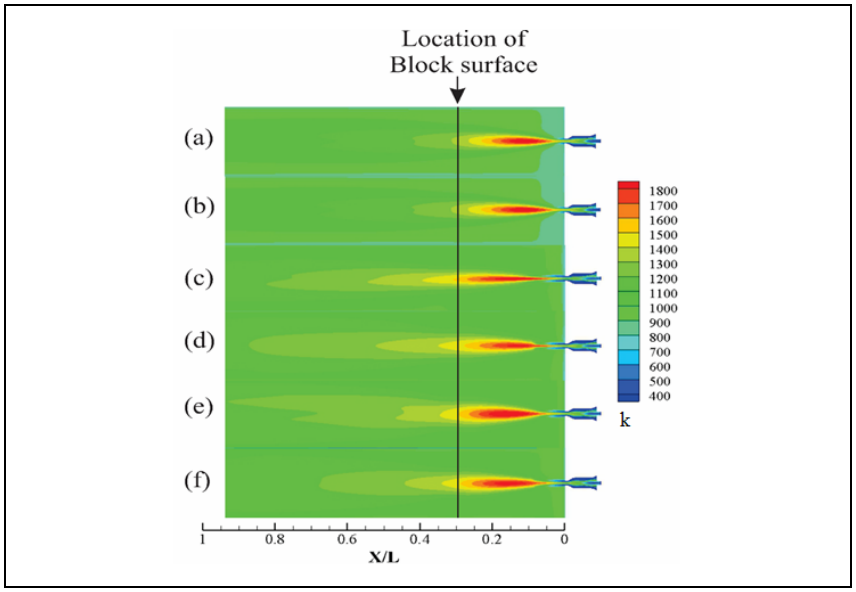

Figure 6.6 Time averaged temperature contours of a high momentum lower burner predicted by a) Standard $k-\varepsilon$, b) Realizable $k-\varepsilon$, c) standard $k-\omega$, d) SST $k-\omega$, e) RNG, and f) RSM models.

Results reveal that the standard and realizable $k-\varepsilon$ models (Figs. 6.6 (a) and 6.6 (b)) under-predicted the flame temperature, as compared with the RSM model. Lower temperatures were experienced around the stagnation line regarding these models' predictions, while standard $k-\omega$ predicted the highest level of contour near the stagnation line (Fig. 6.6 (c)). However, it should be mentioned that the standard and realizable $k-\varepsilon$ models could predict the flame temperature fairly well in the lateral direction, whereas a thin flame is revealed as a result of the simulation by standard $k-\omega$ model. This is because the $k-\omega$ model is originally developed to solve the near-wall region. On the other hand, the standard $k-\varepsilon$ model, which is well suited for high Reynolds number flows, is more reliable to solve the turbulent core region of the flow near the burners. An over-prediction of the time-averaged

temperature around the burner region is also visible for RNG and SST $k-\omega$ simulations, as compared with the RSM model. However, the same temperature range was experienced near the stagnation line by SST $k-\omega$ and RSM, as also illustrated in Fig 6.5 (a). The RNG model also predicts higher temperatures in the flow field and near the stagnation line, as shown in Fig. 6 (e), which further confirms the discussion of Fig. 6.5.

Contours of the time-averaged temperature distribution in the lower burner region and around the stagnation point on the forged block at $t = t_T/6$, as predicted by the different turbulence models, are demonstrated in Fig. 6.7. The highest value of the temperature concerning all the models was predicted inside the furnace and after the burner's nozzle exit. It can be seen that, that the flame as well as the stagnation point for the standard $k-\omega$ and RNG models showed higher range of temperatures in comparison with the other models, in agreement with the results reported in Figs. 6.5 and 6.6. The results reported in Fig. 6.7 show also that an over-prediction of the flame temperature in the longitudinal direction by the standard $k-\omega$ and RNG models resulted in higher temperatures in the stagnation region. Meanwhile, standard $k-\varepsilon$ predicted the lowest values around the stagnation line and flame direction, when compared to RSM. Furthermore, although SST $k-\omega$ over-predicted the flame temperature in the longitudinal direction, in absolute terms, this value was however lower compared to those predicted by standard $k-\omega$ and RNG. It should be mentioned that the group of $k-\omega$ models over-predicted the temperature of flow field and the block in the wake region.

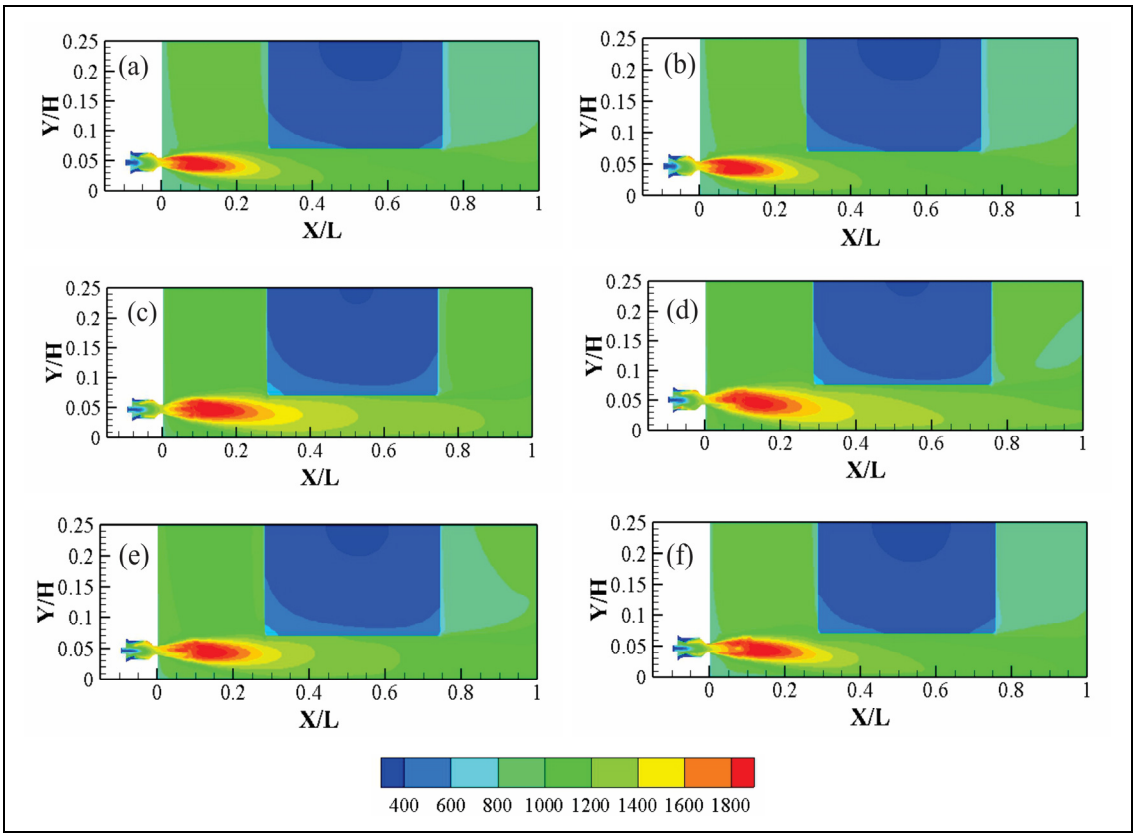

Figure 6.7 Mean temperature contours of lower burner as predicted by a) standard $k-\varepsilon$, b) realizable $k-\varepsilon$, c) standard $k-\omega$, d) SST $k-\omega$, e) RNG $k-\varepsilon$, and f) RSM turbulence models.

Considering the results depicted in this sub-section, it can be concluded that the RSM model could predict the stagnation region's temperature in good agreement with the measured data. The SST $k-\omega$ could also predict the scalar field in that region with a reasonable accuracy, while the group of $k-\varepsilon$ models under-predicted the scalar field both in the furnace and on the large block. In order to study the impact of the selection of a turbulence model on the accurate predictions of combustion and temperature evolution during the heat treatment process, a detailed analysis of the thermal interactions was carried out with a focus on three specific models: 1) RSM as the most sound RANS based model, 2) Realizable $k-\varepsilon$ as the most referred and suggested model in the literature (Prieler, Demuth, et al., 2015), and 3) SST $k-\omega$ which could deliver consistent results, as compared with the measured temperatures on the stagnation side of the block.

6.5.2.3 Turbulence modeling effect on combustion simulation

Distributions of the OH (hydroxide) mass fraction in the axial direction (X/L), as a representation of the flame length (main reaction zone), predicted by the three turbulence models, are displayed in Fig. 6.8. For all the models, the maximum OH fraction is near the burner exit ($X/L < 0.1$). However, lower radical concentrations in the furnace were predicted by the realizable $k-\varepsilon$ model, as compared with RSM, which further confirms the shorter flame length reported in Figs. 6.6 and 6.7. On the other hand, the SST $k-\omega$ model shows more OH fractions in the furnace both in the peak region and in the flame direction ($X/L > 0.2$), resulting in a longer flame length.

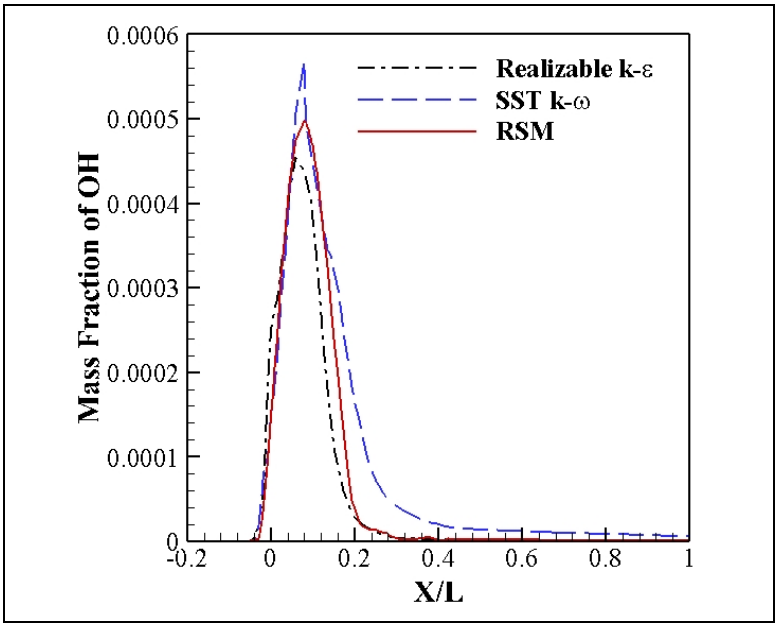

Figure 6.8 Distribution of OH mass fraction in burner's axial direction.

The above findings can be analyzed in terms of the mixture fraction variance ($\overline{f'^2}$) calculation in the non-premix combustion model. The ratio of eddy dissipation rate to turbulence kinetic energy (ε/k), calculated by the different turbulence models, directly

affects the term $C_d\rho\overline{f'^2}(\varepsilon/\mathrm{k})$ (see Eq. (6.10)). The term $C_d\rho\overline{f'^2}(\varepsilon/\mathrm{k})$ imposes the effect of turbulence modeling to the reaction flow simulation (ANSYS, 2016).

Figs. 6.9 (a) and 6.9 (b) depict the mean mixture fraction and the mixture fraction variance of the combustion along a lower burner centerline, respectively. Mixture fraction depends on the fuel mass with the maximum value inside the burner ($X/L = -0.1$) and it is very small when the entire fuel is consumed (i.e., far from the flame region). After initiation of the combustion in the primary and secondary chambers, its value decreases until the end of the flame within the furnace. Results in Fig. 6.9 also show that realizable $k-\varepsilon$ predicted lower mean mixture fraction along the burner centerline both inside the burner and the furnace, as compared with the other two models. The SST $k-\omega$ model also under-predicted the mixture fraction inside the burner. However, it gives more consistent predictions relative to RSM in the furnace region which indicates that the identified differences in the flame length should be mostly related to mixture fraction variances. Fig. 6.9 (b) shows on the other hand that SST $k-\omega$ over-predicted the mixture fraction variance when compared to RSM, while realizable $k-\varepsilon$ under-predicted it. Fig. 6.9 (c) shows the axial variations of the flame scalar dissipation rate along the centerline of the burner for the three different turbulence models. The scalar dissipation rate is zero except in the flame region and it is maximum where the maximum rate of chemical reactions takes place, as a result of turbulence and flame strain (Bazdidi-Tehrani, Mirzaei, & Abedinejad, 2017). It can be seen that the realizable $k-\varepsilon$ model predicted lower scalar dissipation rate values compared to the RSM model both in the burner region ($X/L < 0$) by up to 50%, and furnace medium ($X/L > 0$) by up to 42%. However, both models provided approximately the same value near the burner exit ($X/L \approx 0$). In other words, the identified flame length should be related to the scalar dissipation rate in the furnace region. Meanwhile, the SST $k-\omega$ over-predicted the scalar dissipation rate by about 32%, as compared with RSM in the burner exit ($X/L = 0$).

Comparison of the ε/k ratios regarding Fig. 6.9 (d) shows that the observed trends in Figs. 6.9 (a) and 6.9 (b) have a direct relation with the prediction of the ε/k ratio. Specifically, the under-prediction made by the realizable $k-\varepsilon$ model and the over-prediction by the SST $k-$

ω model clarifies the identified relation. Similar values of the ε/k ratio was observed by SST $k-\omega$ and RSM, in the range of $0.04<X/L<0.08$, leading to comparable results for the scalar dissipation rate. However, the over-prediction of the ε/k ratio after $X/L > 0.1$ is probably the root cause for observing higher values for the mixture fraction variance by the SST $k-\omega$ model in comparison with RSM.

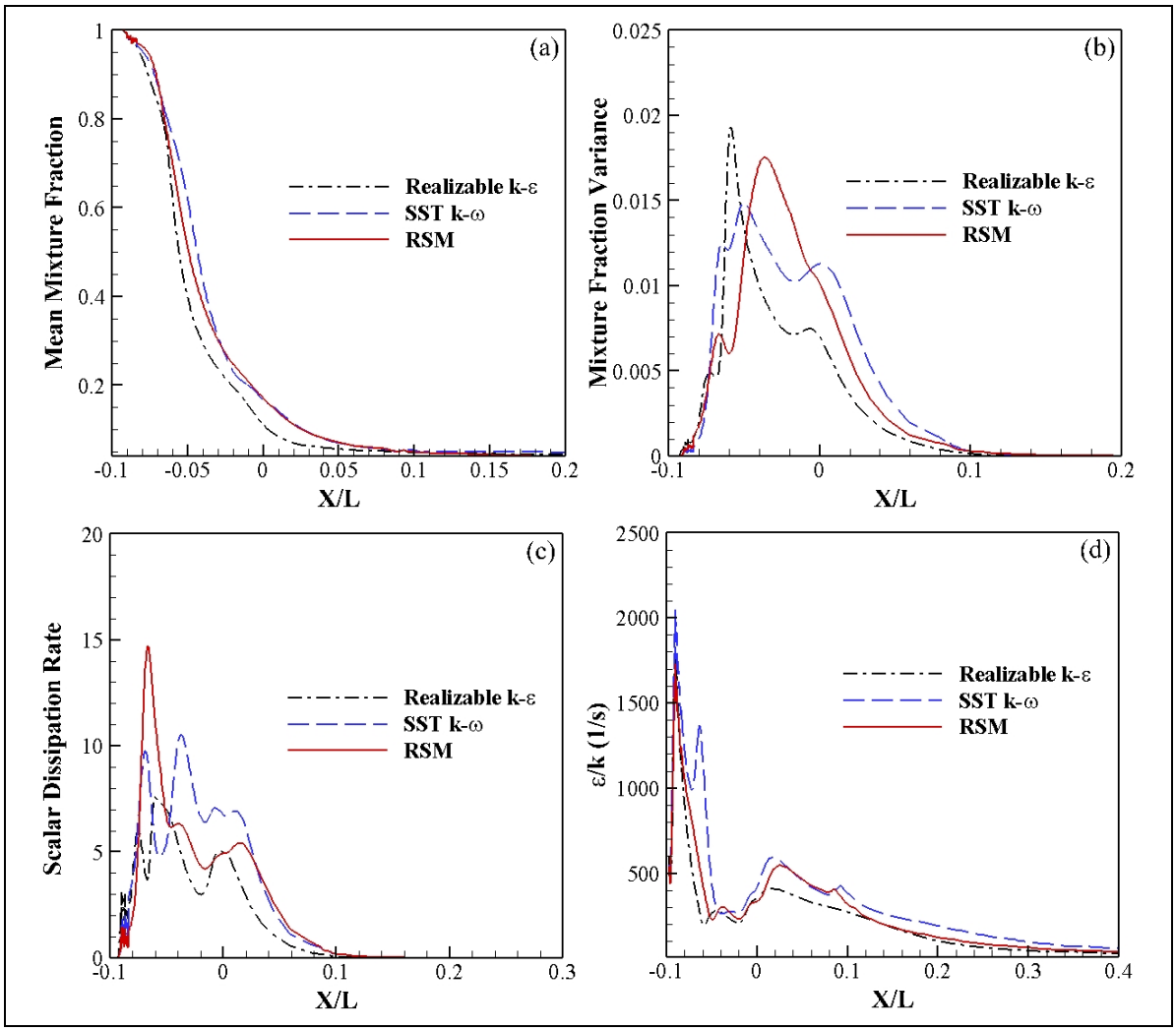

Figure 6.9 Influence of turbulence modeling on axial distribution of a) mean mixture fraction, b) mixture fraction variance, c) scalar dissipation rate, and d) ε/k ratio at burner centerline.

The observed trends in the ε/k ratio can be interpreted by analyzing the results of Fig. 6.10, where the contours of the turbulence kinetic energy near the lower burner region are depicted.

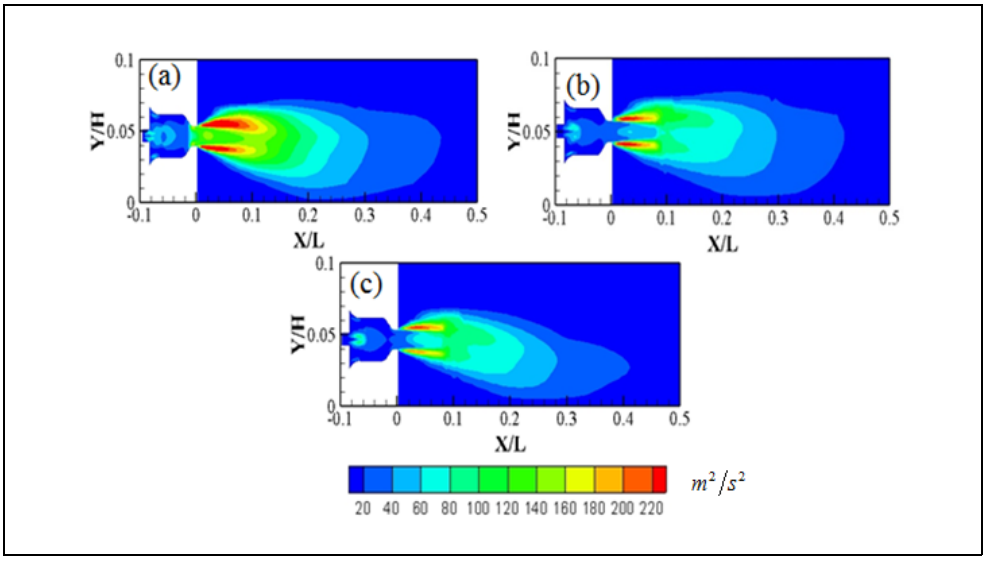

Figure 6.10 Turbulence kinetic energy contours of lower burner region by a) realizable $k-\varepsilon$, b) SST $k-\omega$, and c) RSM turbulence models.

It is revealed that the turbulence kinetic energy, TKE, was highly over-predicted near the nozzle exit ($0<X/L<0.1$) and along the centerline by the realizable $k-\varepsilon$ model in comparison with the other two models. This excessive TKE prediction could be related to an over-estimation of the turbulence production term, because in realizable $k-\varepsilon$ an isotropic eddy viscosity condition is assumed, which is a significant over-simplification for the present case where a highly anisotropic flow field is present. The over-prediction of TKE by the group of $k-\varepsilon$ models has already been mentioned in several turbulence included applications pointing out the fact that the $k-\varepsilon$ models fail to resolve the normal stress anisotropy (Leschziner, 2006; Tominaga & Stathopoulos, 2013). It should be noted that the eddy viscosity models have some limitations in systems with rotation, swirl secondary strains, large strain rates and impingement which should be taken into consideration in the analysis (Tominaga & Stathopoulos, 2013). It can be seen that SST $k-\omega$ gave a reasonably similar range of TKE compared to RSM at the burner exit ($X/L<0.1$) which is in agreement

with the findings in Fig. 6.9 (d). Considering the negligible difference in the results of the eddy dissipation predictions by different models, it can be concluded that the TKE prediction has a direct impact on the ε/k ratio and, subsequently, on the scalar dissipation rate and the mixture fraction variance.

6.5.2.4 Turbulence modeling impact on block's temperature distribution

Investigation of the temperature distribution inside the forged block can help quantifying the impact of turbulence modeling on the overall temperature distribution of the products within gas-fired heat treatment furnaces. In this regard, Fig. 6.11 displays the temperature distributions inside the forged block along three lateral lines, X/W (W indicates the width of block), at the heights of Y/H= 0.25, 0.5, and 0.75. Increasing the height resulted in the reduction of the temperature levels, which could be related to the presence of heating sources (i.e., combustion of lower burners) adjacent to the bottom surface. Apart from the stagnation point (see also Fig. 6.5), the three turbulence models provided similar predictions of the temperature on the wall of the stagnation side. However, a slight over-prediction of the temperature (a maximum of 2.6%) on the stagnation side was found for SST $k-\omega$ at Y/H=0.75 (Fig. 6.11 (c)). Results indicate that all the models predicted almost the same temperatures around the block center (X/W=0) at Y/H=0.25 and 0.5. However, the SST $k-\omega$ over-predicted the block temperature by about 7% in the center of the block, at Y/H=0.75. In addition, SST $k-\omega$ over-predicted the temperature of the wake region wall (by up to 9% at Y/H=0.75) in comparison with RSM. On the other hand, Realizable $k-\varepsilon$ showed good consistency with RSM, not only on the stagnation side, but also inside the block.

The above results demonstrate that the realizable $k-\varepsilon$ model could reasonably predict the temperature evolution of the block within the gas-fired furnace. This particular model characterized with a lower computational cost per iteration, as compared with RSM, could be a reliable model for the block temperature predictions. Although, SST $k-\omega$ showed reasonable results on the stagnation line and computation of the maximum temperature of the block (which can be used for the residence time optimization of the products inside the

furnace) it has limitations regarding the temperature predictions of the wake region. However, an accurate prediction of the wake region behind the block is of great importance for the temperature prediction as well as evaluation of turbulence modeling in applications where large size parts are used.

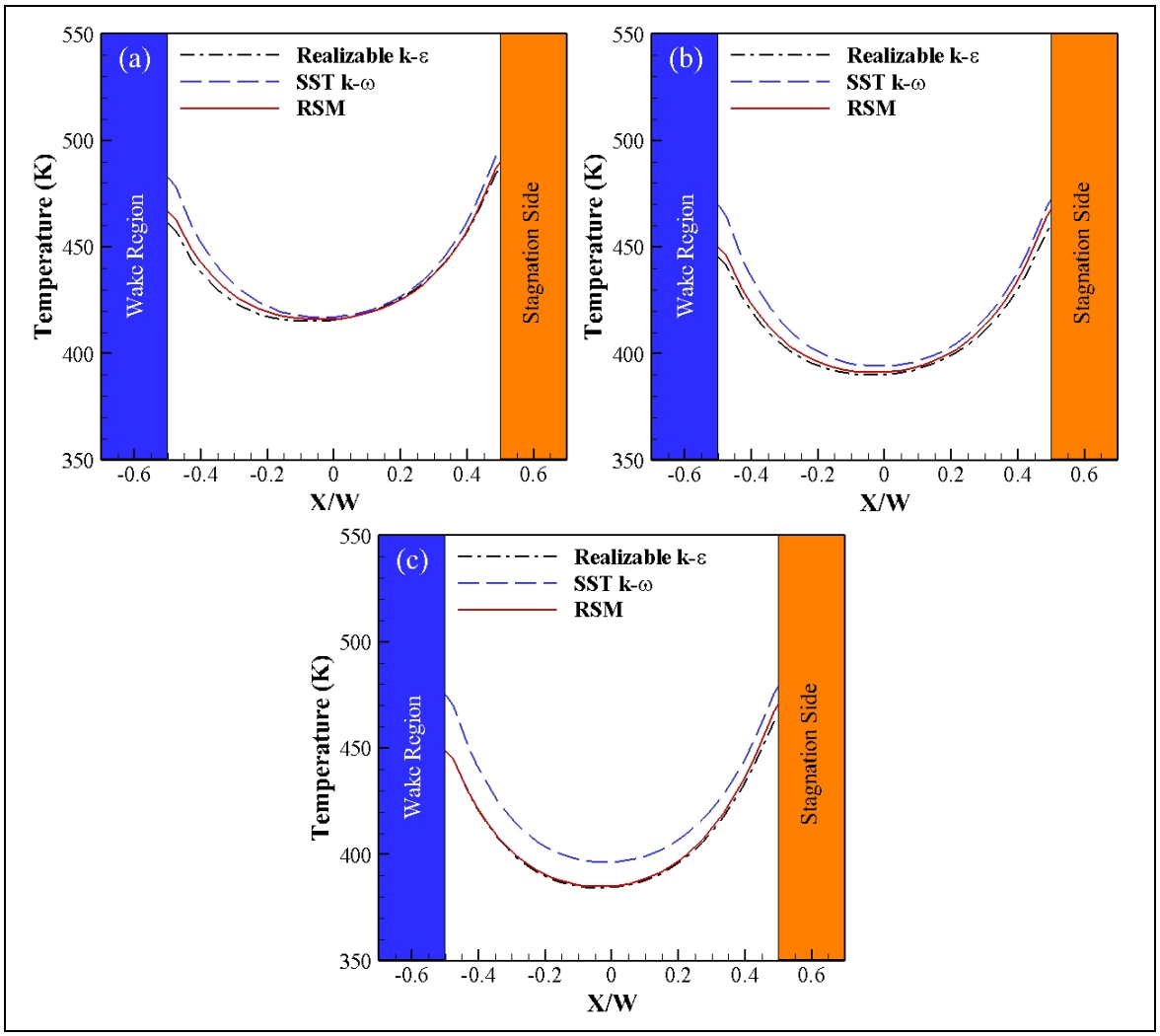

Figure 6.11 Temperature distribution of large size block predicted by three turbulence models at non-dimensional heights of a) Y/H=0.25, b) Y/H=0.5, and c) Y/H=0.75.

6.5.2.5 Analysis of vortical structures

The influence of the vortical structures formation on the transient temperature history of the forged block inside the furnace was discussed in a recent publication by Bohlooli et al. (Bohlooli Arkhazloo et al., 2019). Fig. 6.12 represents the streamlines of flow field as predicted by the three various turbulence models.

Although, inconsistencies can be observed on the upper side of the furnace, realizable $k-\varepsilon$ and SST $k-\omega$ fairly captured the streamlines attached to the top surface of the slab. However, realizable $k-\varepsilon$ could not capture the vortical structure on the top of the block. An over-prediction of the turbulence kinetic energy by the group of $k-\varepsilon$ models results in a high value of the eddy viscosity computation. Consequently, an excessive mixing effect reduced the reversed flow on the top surface of the block. Besides, SST $k-\omega$ and realizable $k-\varepsilon$ could not accurately predict the locations and strength of vortical structures on the wake region. For example, the location of a strong recirculating vortex on the wake region was not consistent for the three models. This may be related with the fact that the velocity fluctuation induced by the vortices cannot be produced by the two equation models. A similar behavior was reported by Tominaga and Stathopoulos (Tominaga & Stathopoulos, 2013) in the simulation of flow and dispersion around a cubic model building. According to reference (Tominaga & Stathopoulos, 2013), the two equation RANS based models can not accurately reproduce the vortex shedding velocity fluctuation behind the bluff body. This inconsistency in the local prediction of the flow recirculation could be the reason for the over- and under-prediction of the temperature at the wake side of the block by the SST $k-\omega$ and the realizable $k-\varepsilon$, respectively. The recirculating part was formed on the bigger heights for SST $k-\omega$, as compared with RSM, which could be related to the over-prediction of the temperature at Y/H=0.75 in Fig. 6.11 (c), as a result of a reattachment of the high temperature fluid to the block wall. On the other hand, although the realizable $k-\varepsilon$ could not accurately predict the location of the vortical structure in comparison with the RSM, it resulted in a similar attachment of the fluid flow near the wake region wall giving similar temperatures in this region (see Fig. 6.11).

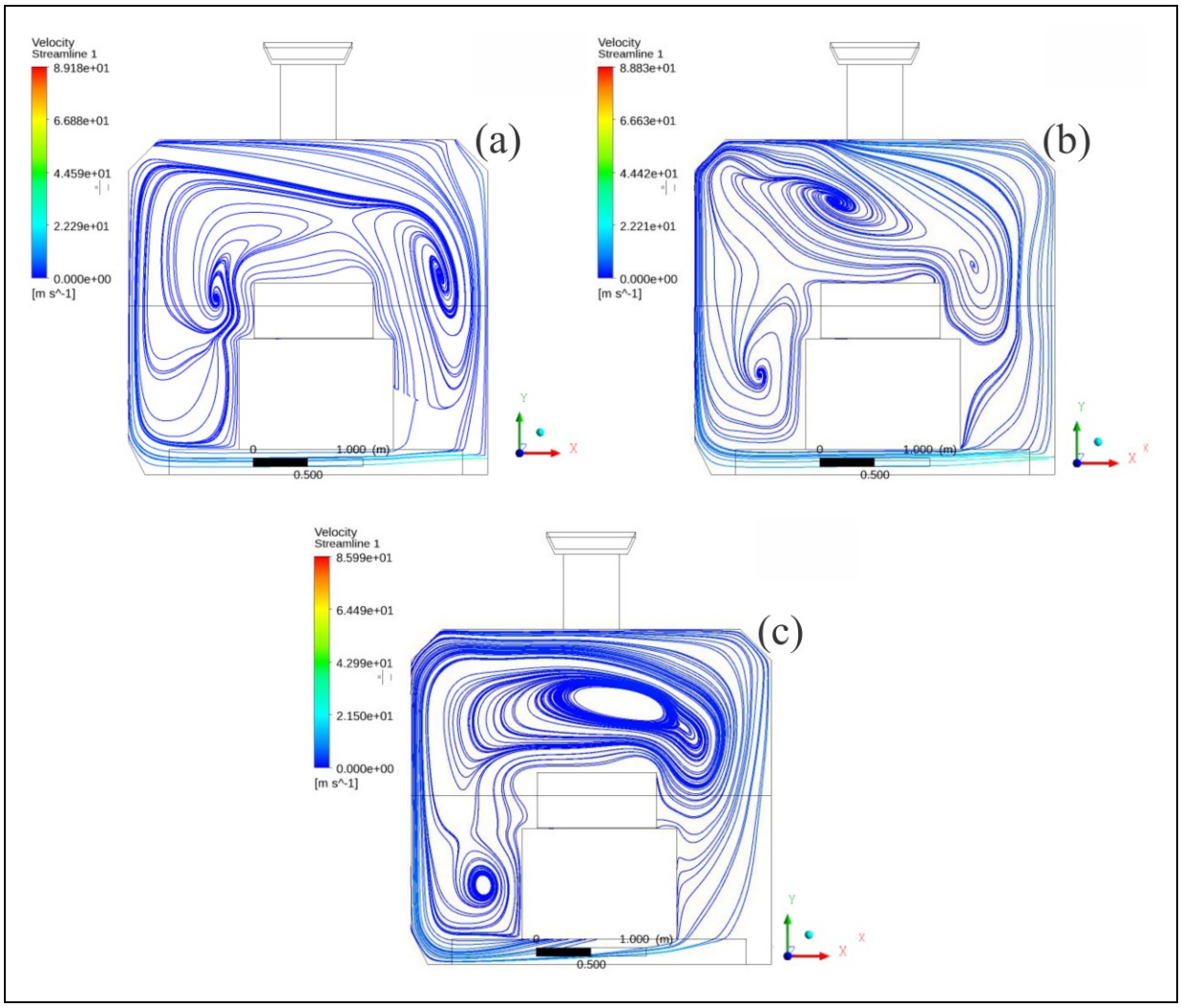

Figure 6.12 Streamlines at a plane along with lower burner centerline by a) realizable $k-\varepsilon$, b) SST $k-\omega$, and c) RSM models $t = t_T/6$.

6.6 Conclusions

A comprehensive evaluation of the turbulence and combustion modeling, employing a one-third periodic 3D model of a gas-fired heat treatment furnace, was performed for both the scalar and flow field predictions. The following main conclusions may be drawn from the present transient CFD simulations:

1. The periodic one-third CFD model including chemical equilibrium non-premix combustion model could be a reliable representative of the present gas-fired furnace revealing good agreement with the presently measured data.

2. The present work showed that the choice of a turbulence model has a significant effect on the prediction of combustion and heat transfer phenomena around the block and the burners.

3. Prediction of the ε/k ratio in the mean mixture fraction variance transport equation, which changes the scalar dissipation rate in the combustion zone could directly affect the flame length and heat transfer rates to the block. The $k-\varepsilon$ group of models by providing an over-prediction of the turbulence kinetic energy and consequently under-prediction of the ε/k ratio, under- estimated the flame length and heat transfer rates around the burner compared to the RSM and SST $k-\omega$ models, as well as temperature measurements..

4. The RSM model could predict the most accurate results, as compared with the measured data in the context of the present study.

5. Although some under-predictions were observed for the flame length and stagnation region's temperature predictions, the realizable $k-\varepsilon$ provided the block temperature history and the wake region turbulence flow field with an acceptable consistency, as compared with RSM.

6. The $k-\omega$ group of models over-predicted the temperature field inside the large size block, mainly due to a failure in capturing the wake region.

CONCLUSION

The work presented in this thesis focused on the numerical/experimental analysis of large size forgings heat treatment process inside gas-fired furnaces. Thermal interactions inside the furnace were analyzed to reduce temperature non-uniformity distribution of forgings as well as reduction of their residence time inside large size gas-fired heat treatment furnaces. Details of thermal interactions including combustion, radiation, and turbulence inside the furnace were discussed. Also, a systematic investigation of strength and limitations of different numerical models to simulate radiation, combustion and turbulence in the present context was presented. Enlisted are the drawn conclusions from this research.

1. 3D CFD models including one-third periodic configuration covering practical details of the furnace such as high momentum burners and fixing bars was capable enough to capture the experimentally measured temperature evolution of the forged ingot.

2. Analysis of experimental temperature measurements showed that the unloaded furnace domain was uniform during the test. However, after loading temperature non-uniformities on the forged ingot surfaces (up to 200 K and 331 K for the conventional single and multiple loading, respectively) were found during the process. Findings indicate the forged ingots loading and their sizes, could affect the uniformity performance of the furnace and subsequently the final product properties.

3. The identified temperature distribution non-uniformities were affected by influence of geometrical effects (such as burner locations and fixing bars), turbulence flow field (formation of vortical structures), and loading patterns inside the furnace. These items should be taken into consideration for optimizing the heat treatment process of large size components.

4. Taking the advantages of skids and spacers usage in the multiple loading configurations can effectively help the process optimization. It could reduce the

temperature non-uniformity of large size forgings inside the gas-fired furnace up to 32%.

5. The hybrid methodology proposed and validated for residence time optimization of large size forging in this work could be applied to other furnace types or steel alloys. It was possible to reduce the total residence time of large parts by about 15.5% for the process of this investigation.

6. It was found that the convection heat transfer was the dominant heat transfer mechanism in the presence of central spacers to affect the temperature uniformity of the heavy steel parts in gas-fired furnaces.

7. Analysis of results showed that the radiation view factor had a higher contribution than participating medium in the radiation heat transfer mode during the process as both DO an S2S model resulted in predictions with less than 2% differences. Therefore, S2S model which is characterized by lower computational cost model compared with DO, can be effectively used in the heat treatment analysis of large size components.

8. Applicability of non-premix combustion with equilibrium model as a computationally effective combustion model was approved along with EDM model for the context of the present study.

9. The choice of the turbulence model in the present application had a significant effect on the combustion and heat transfer phenomenon around the block and the burners. Specifically, prediction of ε/k term by different models could directly affect the mean mixture fraction variance and change the scalar dissipation rate in the combustion zone, leading to changing in the flame length and heat transfer rates to the block.

10. RSM model was approved as the soundest RANS based turbulence model in the context of present study to accurately predict the thermal interactions in critical regions around the block using standard suggested coefficients for the simulations.

11. The SST $k-\omega$ model could also predict the scalar field in this region with a reasonable accuracy.

12. It could be concluded that apart from some under-predictions observed for the flame length and stagnation region's temperature predictions by realizable $k-\varepsilon$ model, this model could illustrate global block temperature history with an acceptable consistency, as compared with RSM model and measurements.

13. Although the SST $k-\omega$ model failed to capture the wake regions revealed an over-predicted temperature field inside the large size block temperature, it resulted in reasonable predictions in the stagnation point and burner combustion (which can be used for the process optimization using developed hybrid technology). It should be mentioned that the standard $k-\omega$ model and the RNG $k-\varepsilon$ could not accurately predict the thermal interactions, neither in the stagnation region, nor on the wake region.

14. The developed CFD model and its data as well as experimental measurements including hybrid methodology could be directly applied for the optimization of the operational conditions and loading patterns during the heat treatment process of large size forged ingots within gas-fired furnaces.

RECOMMENDATIONS

The main purpose of present study was to carry out a comprehensive analysis of thermal interactions during the heat treatment of large size forgings within gas-fired furnaces; and subsequently to improve product's residence time and loading pattern in this context. Apart from directly applicable information to the real scale heat treatment of heavy forgings provided by the present study, the following future investigations are suggested:

1) Application of hybrid methodology for other grades of steels for residence time optimization of different large size heavy forgings. It is suggested to investigate different metallurgical aspects (like residual stresses, microstructural transformations) along with the hardness measurements for the further optimization.

2) In the present study natural gas and air at room temperature were employed for the combustion. It is recommended to carry out an investigation on the pre-heated air combustion effectiveness.

3) It was approved in this study that the radiation view factor was the dominant parameter for accurate simulation of radiation heat transfer in the gas-fired furnace. It is suggested to make analytical-numerical study on the optimization of radiation view factor between large size forgings to further optimize the loading pattern within gas-fired furnaces.

4) In the present study, temperature measurements of blocks were used as the main criterion for the validation of numerical simulations. It is suggested to use particle image velocimetry (PIV) measurement technique for further validation of combustion process in the high-momentum gas-fired burner and subsequently investigate the combustion products distributions within the furnace.

LIST OF REFERENCES

ANSYS. (2016). ANSYS Fluent Theory Guide. ANSYS Inc.

Ashgriz, N., & Mostaghimi, J. (2002). An introduction to computational fluid dynamics. Fluid Flow Handbook, 1, 1–49.

Baukal Jr, C. E. (2003). Industrial burners handbook. CrC press.

Bazdidi-Tehrani, F., Bohlooli, N., & Jadidi, M. (2015). Influence of film cooling jet inlet boundary condition on large eddy simulation of model turbine blade leading edge. Progress in Computational Fluid Dynamics, an International Journal, 15(4), 214–227.

Bazdidi-Tehrani, F., Hatami, M., & Abouata, A. (2017). Effects of inlet and outlet boundary conditions on the flow field of synthetic jets. Proceedings of the Institution of Mechanical Engineers, Part E: Journal of Process Mechanical Engineering, 231(2), 107–118.

Bazdidi-Tehrani, F., Mirzaei, S., & Abedinejad, M. S. (2017). Influence of Chemical Mechanisms on Spray Combustion Characteristics of Turbulent Flow in a Wall Jet Can Combustor. Energy & Fuels, 31(7), 7523–7539.

Bazdidi-Tehrani, F., Mohammadi-Ahmar, A., Kiamansouri, M., & Jadidi, M. (2015). Investigation of various non-linear eddy viscosity turbulence models for simulating flow and pollutant dispersion on and around a cubical model building. In Building Simulation (Vol. 8, pp. 149–166). Springer.

Bennett, C. (1962). 0. and JE Myers, Momentum. Heat and Mass Transfer", McGraw-Hill Book Co., Inc., New York, NY, 291.

Bergman, E. (2012). CFD Heat Transfer Validation of Turbine Structure Heat Treatment Process.

Bhadeshia, H., & Honeycombe, R. (2017). Steels: microstructure and properties. Butterworth-Heinemann.

Bohlooli Arkhazloo, N., Bouissa, Y., Bazdidi-Tehrani, F., Jadidi, M., Morin, J.-B., & Jahazi, M. (2019). Experimental and unsteady CFD analyses of the heating process of large size forgings in a gas-fired furnace. Case Studies in Thermal Engineering, 14.

Bowman, C. T. (1991). Chemistry of gaseous pollutant formation and destruction. Fossil Fuel Combustion. John Wiley & Sons, New York.

Canale, L. C. F., Yao, X., Gu, J., & Totten, G. E. (2008). A historical overview of steel tempering parameters. International Journal of Microstructure and Materials Properties, 3(4–5), 474–525.

Cant, R. S. (2001). SB Pope, Turbulent Flows, Cambridge University Press, Cambridge, UK. Combustion and Flame, 125, 1361–1362.

Chapman, K. S., Ramadhyani, S., & Viskanta, R. (1990). Modeling and parametric studies of heat transfer in a direct-fired batch reheating furnace. Journal of Heat Treating, 8(2), 137–146.

Chattopadhyay, K., Isac, M., & Guthrie, R. I. L. (2010). Applications of Computational Fluid Dynamics (CFD) in iron-and steelmaking: Part 1. Ironmaking & Steelmaking, 37(8), 554–561.

Cheng, L., Brakman, C. M., Korevaar, B. M., & Mittemeijer, E. J. (1988). The tempering of iron-carbon martensite; dilatometric and calorimetric analysis. Metallurgical Transactions A, 19(10), 2415–2426.

Chui, E. H., & Raithby, G. D. (1993). Computation of radiant heat transfer on a nonorthogonal mesh using the finite-volume method. Numerical Heat Transfer, 23(3), 269–288.

Constantin, P., & Foias, C. (1988). Navier-stokes equations. University of Chicago Press.

Cosentino, F., Warnken, N., Gebelin, J.-C., & Reed, R. C. (2013). Numerical and experimental study of post-heat treatment gas quenching and its impact on microstructure and creep in CMSX-10 superalloy. Journal of Materials Processing Technology, 213(12), 2350–2360.

Crasto, G. (2007). Numerical simulations of the atmospheric boundary layer. Universita Degli Studi Di Cagliari: Cagliari, Italy.

Danon, B., Cho, E. S., De Jong, W., & Roekaerts, D. J. E. M. (2011). Numerical investigation of burner positioning effects in a multi-burner flameless combustion furnace. Applied Thermal Engineering, 31(17–18), 3885–3896. https://doi.org/10.1016/j.applthermaleng.2011.07.036.

Davidson, L. (2011). Fluid mechanics, turbulent flow and turbulence modeling. Chalmers University of Technology, Goteborg, Sweden (Nov 2011) (Vol. 53).

Denison, M., Borodai, S., Fox, R., & Bockelie, M. (2009). Multi-environment probability density function method for modeling turbulent combustion in industrial equipment. In ASME 2009 International Mechanical Engineering Congress and Exposition (pp. 143–149). American Society of Mechanical Engineers.

Elkatatny, I., Morsi, Y., Blicblau, A. S., Das, S., & Doyle, E. D. (2003). Numerical analysis and experimental validation of high pressure gas quenching. International Journal of Thermal Sciences, 42(4), 417–423.

Finkl Steel Inc., M., Saint-Joseph-de-Sorel, QC J3R 3M8, Canada.

Galletti, C., Coraggio, G., & Tognotti, L. (2013). Numerical investigation of oxy-natural-gas combustion in a semi-industrial furnace: validation of CFD sub-models. Fuel, 109, 445–460.

Gao, M., Reid, C. N., Jahedi, M., & Li, Y. (2000). Estimating equilibration times and heating/cooling rates in heat treatment of workpieces with arbitrary geometry. Journal of Materials Engineering and Performance, 9(1), 62–71.

García, A. M., Colorado, A. F., Obando, J. E., Arrieta, C. E., & Amell, A. A. (2019). Effect of the burner position on an austenitizing process in a walking-beam type reheating furnace. Applied Thermal Engineering, 153, 633–645.

Gongfa, L., Jia, L., Guozhang, J., Jianyi, K., Liangxi, X., Yikun, Z., & Fuwei, C. (2014). Numerical simulation of flow , temperature and phase fields in U71Mn rail-head quenching process, 18(1), 61–70.

Govardhan, J., Rao, G. V. S., & Narasaiah, J. (2011). Experimental investigations and CFD study of temperature distribution during oscillating combustion in a crucible furnace. Journal Homepage: Www. IJEE. IEEFoundation. Org, 2(5), 783–796.

Gur, C. H., & Pan, J. (2008). Handbook of Thermal Process Modeling Steels. CRC Press.

Hadała, B., Malinowski, Z., & Rywotycki, M. (2017). Energy losses from the furnace chamber walls during heating and heat treatment of heavy forgings. Energy, 139, 298–314.

Hao, X., Gu, J., Chen, N., Zhang, W., & Zuo, X. (2008). 3-D Numerical analysis on heating process of loads within vacuum heat treatment furnace. Applied Thermal Engineering, 28(14–15), 1925–1931.

Harish, J., & Dutta, P. (2005). Heat transfer analysis of pusher type reheat furnace. Ironmaking & Steelmaking, 32(2), 151–158.

Howell, J. R., Menguc, M. P., & Siegel, R. (2015). Thermal radiation heat transfer. CRC press.

https://combustion.fivesgroup.com/.

https://www.tainstruments.com.

Hussain, A. (1983). Coherent structures-Reality and myth.[in turbulent shear flow.

Incropera, F. P., Lavine, A. S., Bergman, T. L., & DeWitt, D. P. (2007). Fundamentals of heat and mass transfer. Wiley.

ISA Standard. (1982). Temperature Measurement Thermocouples.

Ishii, T., Zhang, C., & Hino, Y. (2002). Numerical study of the performance of a regenerative furnace. Heat Transfer Engineering, 23(4), 23–33.

Ishii, T., Zhang, C., & Sugiyama, S. (1998). Numerical simulations of highly preheated air combustion in an industrial furnace. Journal of Energy Resources Technology, 120(4), 276–284.

Ismail, H. M., Ng, H. K., & Gan, S. (2012). Evaluation of non-premixed combustion and fuel spray models for in-cylinder diesel engine simulation. Applied Energy, 90(1), 271–279.

Jaklič, A., Glogovac, B., Kolenko, T., Zupančič, B., & Težak, B. (2002). A simulation of heat transfer during billet transport. Applied Thermal Engineering, 22(7), 873–883.

Janjušević, Z., Gulišija, Z., Mihailović, M., & Patarić, A. (2009). The investigation of applicability of the Hollomon-Jaffe equation on tempering the HSLA steel. Chemical Industry and Chemical Engineering Quarterly/CICEQ, 15(3), 131–136.

JMatPro Users Guide 6.2.1. (n.d.). Ansys inc.

Kang, J., & Rong, Y. (2006). Modeling and simulation of load heating in heat treatment furnaces. Journal of Materials Processing Technology, 174(1–3), 109–114.

Kim, S.-E., Choudhury, D., & Patel, B. (1999). Computations of complex turbulent flows using the commercial code FLUENT. In Modeling complex turbulent flows (pp. 259–276). Springer.

Korad, T., Ponboon, M., Chumchery, N., & Pearce, J. T. H. (2013). Overview of Flow Analysis Simulation in Improving Heat Treatment Conditions. CHIANG MAI JOURNAL OF SCIENCE, 40(5), 898–908.

Launder, B. E., Reece, G. J., & Rodi, W. (1975). Progress in the development of a Reynolds-stress turbulence closure. Journal of Fluid Mechanics, 68(3), 537–566.

Launder, B. E., & Spalding, D. B. (1972). Mathematical models of turbulence. Academic press.

Leschziner, M. A. (2006). Modelling turbulent separated flow in the context of aerodynamic applications. Fluid Dynamics Research, 38(2–3), 174–210.

Lior, N. (2004). The cooling process in gas quenching. Journal of Materials Processing Technology, 155, 1881–1888.

Liščić, B., & Filetin, T. (1987). Computer-aided determination of the process parameters for hardening and tempering structural steels. Heat Treatment of Metals, 3, 62.

Liu, Y. J., Li, J. D., Misra, R. D. K., Wang, Z. D., & Wang, G. D. (2016). A numerical analysis of slab heating characteristics in a rolling type reheating furnace with pulse combustion. Applied Thermal Engineering, 107, 1304–1312.

Liu, Y., Liu, Y., Tao, S., Liu, X., & Wen, Z. (2014). Three-dimensional analysis of gas flow and heat transfer in a regenerator with alumina balls. Applied Thermal Engineering, 69(1–2), 113–122.

Macchion, O. (2005). CFD in the design of gas quenching furnace. KTH.

Macchion, O., Lior, N., & Rizzi, A. (2004). Computational study of velocity distribution and pressure drop for designing some gas quench chamber and furnace ducts. Journal of Materials Processing Technology, 155, 1727–1733.

Macchion, O., Zahrai, S., & Bouwman, J. W. (2005). On Heat Transfer within Gas Quenching Furnace. IASME Transactions.

Macchion, O., Zahrai, S., & Bouwman, J. W. (2006). Heat transfer from typical loads within gas quenching furnace. Journal of Materials Processing Technology, 172(3), 356–362.

Magnussen, B. (1981). On the structure of turbulence and a generalized eddy dissipation concept for chemical reaction in turbulent flow. In 19th aerospace sciences meeting (p. 42).

Magnussen, B. F., & Hjertager, B. H. (1977). On mathematical modeling of turbulent combustion with special emphasis on soot formation and combustion. In Symposium (international) on Combustion (Vol. 16, pp. 719–729). Elsevier.

Mallela, G., Paturu, P., Kumar, P. K., Komaleswararao, M., Sharma, S., & Vardhan, G. H. (2019). Thermal efficiency and heat balance of reheating furnace of rolling mills. International Journal of Ambient Energy, 1–6.

Mayr, B., Prieler, R., Demuth, M., Moderer, L., & Hochenauer, C. (2017). CFD analysis of a pusher type reheating furnace and the billet heating characteristic. Applied Thermal Engineering, 115, 986–994. https://doi.org/10.1016/j.applthermaleng, 2017.01.028.

Mayr, B., Prieler, R., Demuth, M., Potesser, M., & Hochenauer, C. (2017). Computational analysis of a semi-industrial furnace fired by a flat flame burner under different O2/N2ratios using the steady laminar flamelet approach. Journal of the Energy Institute, 90(4), 602–612. https://doi.org/10.1016/j.joei.2016.05.002.

Mayr, B, Prieler, R., Demuth, M., Moderer, L., & Hochenauer, C. (2017). CFD analysis of a pusher type reheating furnace and the billet heating characteristic. Applied Thermal Engineering, 115, 986–994.

Mayr, B, Prieler, R., Demuth, M., Potesser, M., & Hochenauer, C. (2017). Computational analysis of a semi-industrial furnace fired by a flat flame burner under different O2/N2 ratios using the steady laminar flamelet approach. Journal of the Energy Institute, 90(4), 602–612.

Mayr, Bernhard, Prieler, R., Demuth, M., Potesser, M., & Hochenauer, C. (2015). CFD and experimental analysis of a 115 kW natural gas fired lab-scale furnace under oxy-fuel and air–fuel conditions. Fuel, 159, 864–875.

Menter, F. R. (1994). Two-equation eddy-viscosity turbulence models for engineering applications. AIAA Journal, 32(8), 1598–1605.

Murakami, S. (1993). Comparison of various turbulence models applied to a bluff body. Journal of Wind Engineering and Industrial Aerodynamics, 46, 21–36.

Ničeno, B., Dronkers, A. D. T., & Hanjalić, K. (2002). Turbulent heat transfer from a multi-layered wall-mounted cube matrix: a large eddy simulation. International Journal of Heat and Fluid Flow, 23(2), 173–185.

Ortega-Casanova, J., & Castillo-Sanchez, S. I. (2017). On using axisymmetric turbulent impinging jets swirling as Burger's vortex for heat transfer applications. Single and multi-objective vortex parameters optimization. Applied Thermal Engineering, 121, 103–114.

Patankar, S. (2018). Numerical heat transfer and fluid flow. CRC press.

Pyradia Inc., 5125 Rue J,-A,- Bombardier, Saint-Hubert, Canada, https://www.pyradia.com/.

Poinsot, T., & Veynante, D. (2005). Theoretical and numerical combustion. RT Edwards, Inc.

Pollack, H. W. (1988). Materials science and metallurgy.

Prieler, R., Demuth, M., Spoljaric, D., & Hochenauer, C. (2015). Numerical investigation of the steady flamelet approach under different combustion environments. Fuel, 140, 731–743.

Prieler, R., Mayr, B., Demuth, M., Holleis, B., & Hochenauer, C. (2016). Prediction of the heating characteristic of billets in a walking hearth type reheating furnace using CFD. International Journal of Heat and Mass Transfer, 92, 675–688.

Prieler, R., Mayr, B., Demuth, M., Spoljaric, D., & Hochenauer, C. (2015). Application of the steady flamelet model on a lab-scale and an industrial furnace for different oxygen concentrations. Energy, 91, 451–464.

Primig, S., & Leitner, H. (2011). Separation of overlapping retained austenite decomposition and cementite precipitation reactions during tempering of martensitic steel by means of thermal analysis. Thermochimica Acta, 526(1–2), 111–117.

Pulat, E., Isman, M. K., Etemoglu, A. B., & Can, M. (2011). Effect of turbulence models and near-wall modeling approaches on numerical results in impingement heat transfer. Numerical Heat Transfer, Part B: Fundamentals, 60(6), 486–519.

Purushothaman, R. (2008). Evaluation and improvement of heat treat furnace model.

Rad, S. D., Ashrafizadeh, A., & Nickaeen, M. (2017). Numerical simulation of fluid flow and heat transfer in an industrial continuous furnace. Applied Thermal Engineering, 117, 263–274.

Raithby, G. D., & Chui, E. H. (1990). A finite-volume method for predicting a radiant heat transfer in enclosures with participating media. Journal of Heat Transfer, 112(2), 415–423.

Ray, P. K., Ganguly, R. I., & Panda, A. K. (2003). Optimization of mechanical properties of an HSLA-100 steel through control of heat treatment variables. Materials Science and Engineering: A, 346(1–2), 122–131.

Revilla, C., López, B., & Rodriguez-Ibabe, J. M. (2014). Carbide size refinement by controlling the heating rate during induction tempering in a low alloy steel. Materials & Design (1980-2015), 62, 296–304.

Rezazadeh, N., Hosseinzadeh, H., & Wu, B. (2019). Effect of burners configuration on performance of heat treatment furnaces. International Journal of Heat and Mass Transfer, 136, 799–807.

Saunders, N., Guo, U. K. Z., Li, X., Miodownik, A. P., & Schillé, J.-P. (2003). Using JMatPro to model materials properties and behavior. Jom, 55(12), 60–65.

Sazhin, S. S., Sazhina, E. M., Faltsi-Saravelou, O., & Wild, P. (1996). The P-1 model for thermal radiation transfer: advantages and limitations. Fuel, 75(3), 289–294.

Schiestel, R. (1983). Multiple scale concept in turbulence modeling. 2. reynolds stresses and turbulent fluxes of a passive scalar, algebraic modeling and simplified model using boussinesq hypothesis. journal de mecanique theorique et appliquee, 2(4), 601–628.

Shih, T.-H., Zhu, J., & Lumley, J. L. (1993). A realizable Reynolds stress algebraic equation model.

Singh, V. K., Talukdar, P., & Coelho, P. J. (2015). Performance evaluation of two heat transfer models of a walking beam type reheat furnace. Heat Transfer Engineering, 36(1), 91–101.

Sivathanu, Y. R., & Faeth, G. M. (1990). Generalized state relationships for scalar properties in nonpremixed hydrocarbon/air flames. Combustion and Flame, 82(2), 211–230.

Smith, T. F., Shen, Z. F., & Friedman, J. N. (1982). Evaluation of coefficients for the weighted sum of gray gases model. Journal of Heat Transfer, 104(4), 602–608.

Spalding, D. B. (1971). Mixing and chemical reaction in steady confined turbulent flames. In Symposium (International) on Combustion (Vol. 13, pp. 649–657). Elsevier.

Speich, G. R., & Leslie, W. C. (1972). Tempering of steel. Metallurgical Transactions, 3(5), 1043–1054.

Szajnar, J., Bartocha, D., Stawarz, M., Wróbel, T., & Sebzda, W. (2010). Computer simulation of the impact of pulling parameters on the process of continuous ingot casting. Archives of Foundry Engineering, 10(1), 47–52.

Tagliafico, L. A., & Senarega, M. (2004). A simulation code for batch heat treatments. International Journal of Thermal Sciences, 43(5), 509–517.

Talebi, S., Ghasemi-Nanesa, H., Jahazi, M., & Melkonyan, H. (2017). In situ study of phase transformations during non-isothermal tempering of bainitic and martensitic microstructures. Metals, 7(9), 346.

Tang, G., Wu, B., Bai, D., Wang, Y., Bodnar, R., & Zhou, C. (2018). CFD modeling and validation of a dynamic slab heating process in an industrial walking beam reheating furnace. Applied Thermal Engineering, 132, 779–789.

Tang, G., Wu, B., Bai, D., Wang, Y., Bodnar, R., & Zhou, C. Q. (2017). Modeling of the slab heating process in a walking beam reheating furnace for process optimization. International Journal of Heat and Mass Transfer, 113, 1142–1151. https://doi.org/10.1016/j.ijheatmasstransfer.2017.06.026.

Tennekes, H., Lumley, J. L., & Lumley, J. L. (1972). A first course in turbulence. MIT press.

Tominaga, Y., & Stathopoulos, T. (2013). CFD simulation of near-field pollutant dispersion in the urban environment: A review of current modeling techniques. Atmospheric Environment, 79, 716–730.

Totten, G. E. (2006). Steel heat treatment: metallurgy and technologies. crc Press.

Tu, Y., Liu, H., Chen, S., Liu, Z., Zhao, H., & Zheng, C. (2015). Effects of furnace chamber shape on the MILD combustion of natural gas. Applied Thermal Engineering, 76, 64–75.

Versteeg, H K, & Malalasekera, W. (2007). An introduction to computional fluid dynamics: The finite volume method.

Versteeg, Henk Kaarle, & Malalasekera, W. (2007). An introduction to computational fluid dynamics: the finite volume method. Pearson education.

Vicquelin, R. (2010). Tabulation de la cinétique chimique pour la modélisation et la simulation de la combustion turbulente. Châtenay-Malabry, Ecole centrale de Paris.

Wang, J., Chen, N. L., & Shan, X. X. (2006). Numerical simulation and measurement of velocity distribution in a gas nitriding furnace. In Solid State Phenomena (Vol. 118, pp. 331–336). Trans Tech Publ.

Wang, J., Gu, J., Shan, X., Hao, X., Chen, N., & Zhang, W. (2008). Numerical simulation of high pressure gas quenching of H13 steel. Journal of Materials Processing Technology, 202(1–3), 188–194.

Wang, Z. J., & Shang, X. F. (2010). Flow and Heat-Transfer Simulation Based on CFD and Experimental Study during High-Pressure Gas Quenching. In Applied Mechanics and Materials (Vol. 29, pp. 1436–1440). Trans Tech Publ.

Wiberg, R. (2001). Heat flux and velocity measurements on and around a single quadratic cylinder, and using groups of quadratic cylinders in the cross flow of air. Internal Report, Faxénlaboratoriet, Kungl. Tekniska Högskolan, Stockholm, Sweden.

Wiberg, Roland, & Lior, N. (2003). Convection heat transfer coefficients for axial flow gas quenching of a cylinder. In Proceedings of the Fourth International Conference on Quenching and the Control of Distortion (Vol. 20, p. 23).

Wilcox, D. C. (1998). Turbulence modeling for CFD (Vol. 2). DCW industries La Canada, CA.

Wu, B., Arnold, A. M., Arnold, E., Downey, G., & Zhou, C. Q. (2007). CFD analysis of batch-type reheating furnace. In ASME 2007 International Mechanical Engineering Congress and Exposition (pp. 753–759). American Society of Mechanical Engineers.

Wu, B. B., Chen, H., Shang, C. J., Xie, K. Y., & Misra, R. D. K. (2019). Effect of Tempering Mode on the Microstructure and Mechanical Properties of a Lean Alloy Martensitic Steel: Conventional Reheating Versus Induction Reheating. Journal of Materials Engineering and Performance, 28(5), 2807–2815.

Wu, B., Roesel, T., Arnold, A. M., Xu, Z., Arnold, E., Downey, G., & Zhou, C. Q. (2008). CFD Analysis of Batch-Type Reheating Furnace With Regeneratve Burners. In ASME 2008 Heat Transfer Summer Conference collocated with the Fluids Engineering, Energy Sustainability, and 3rd Energy Nanotechnology Conferences (pp. 225–234). American Society of Mechanical Engineers.

Yakhot, V., Orszag, S. A., Thangam, S., Gatski, T. B., & Speziale, C. G. (1992). Development of turbulence models for shear flows by a double expansion technique. Physics of Fluids A: Fluid Dynamics, 4(7), 1510–1520.

Yan, G., Han, L., Li, C., Luo, X., & Gu, J. (2017). Characteristic of retained austenite decomposition during tempering and its effect on impact toughness in SA508 Gr. 3 steel. Journal of Nuclear Materials, 483, 167–175.

Yang, Y., De Jong, R. A., & Reuter, M. A. (2007). CFD prediction for the performance of a heat treatment furnace. Progress in Computational Fluid Dynamics, an International Journal, 7(2–4), 209–218.

Yang, Y., Zhou, B., Post, J. R., Scheepers, E., REUTE, M. A., & Boom, R. (2006). Computational fluid dynamics simulation of pyrometallurgical processes. In Proc. 5th Int. Conf. CFD in the Minerals and Process Industries, CSIRO, Melbourne, Australia.

Zhang, C., Ishii, T., Hino, Y., & Sugiyama, S. (2000). The numerical and experimental study of non-premixed combustion flames in regenerative furnaces. Journal of Heat Transfer, 122(2), 287–293.

Zhang, J., Prationo, W., Zhang, L., & Zhang, Z. (2013). Computational fluid dynamics modeling on the air-firing and oxy-fuel combustion of dried Victorian brown coal. Energy & Fuels, 27(8), 4258–4269.

Zhang, S. F., Wen, L. Y., Bai, C. G., Chen, D. F., & Long, Z. J. (2009). Analyses on 3-D gas flow and heat transfer in ladle furnace lid. Applied Mathematical Modelling, 33(6), 2646–2662.

Zhou, B., Yang, Y., Reuter, M. A., & Boin, U. M. J. (2007). CFD-based process modelling of a rotary furnace for aluminium scrap melting. Progress in Computational Fluid Dynamics, 7(2/4), 195.

Zou, D., Ying, H., Zhang, W., & Fang, X. (2010). Influence of tempering process on mechanical properties of 00Cr13Ni4Mo supermartensitic stainless steel. Journal of Iron and Steel Research, International, 17(8), 50–54.

Zuckerman, N., & Lior, N. (2006). Jet impingement heat transfer: physics, correlations, and numerical modeling. Advances in Heat Transfer, 39, 565–631.